On the interplay of topology and interaction:

A quantum Monte Carlo study

DISSERTATION ZUR ERLANGUNG DES
NATURWISSENSCHAFTLICHEN DOKTORGRADES
DER JULIUS-MAXIMILIANS-UNIVERSITÄT WÜRZBURG

vorgelegt von

Johannes Stephan Hofmann

aus Fulda

Würzburg 2019

Eingereicht am: 26.06.2019
bei der Fakultät für Physik und Astronomie

1. Gutachter: Prof. Dr. Fakher F. Assaad
2. Gutachter: Prof. Dr. Björn Trauzettel
3. Gutachter: Prof. Dr. Zi Yang Meng
der Dissertation

Vorsitzender: Prof. Dr. Haye Hinrichsen
1. Prüfer: Prof. Dr. Fakher F. Assaad
2. Prüfer: Prof. Dr. Björn Trauzettel
3. Prüfer: Prof. Dr. Friedrich Reinert
im Promotionskolloquium

Tag des Promotionskolloquiums: 20.12.2019

Doktorurkunde ausgehändigt am: .....

In loving memory of my grandfather,

ERWIN GÖLLER

Abstract

Adding interactions to topological (non-)trivial free fermion systems can in general have four different effects: (i) In symmetry protected topological band insulators, the correlations may lead to the spontaneous breaking of some protecting symmetries by long-range order that gaps the topological boundary modes. (ii) In free fermion (semi-)metal, the interaction could vice versa also generate long-range order that in turn induces a topological mass term and thus generates non-trivial phases dynamically. (iii) Correlation might reduce the topological classification of free fermion systems by allowing adiabatic deformations between states of formerly distinct phases. (iv) Interaction can generate long-range entangled topological order in states such as quantum spin liquids or fractional quantum Hall states that cannot be represented by non-interacting systems. During the course of this thesis, we use numerically exact quantum Monte Carlo algorithms to study various model systems that (potentially) represent one of the four scenarios, respectively.

First, we investigate a two-dimensional d_{xy}-wave, spin-singlet superconductor, which is relevant for high-T_c materials such as the cuprates. This model represents nodal topological superconductors and exhibits chiral flat-band edge states that are protected by time-reversal and translational invariance. We introduce the conventional Hubbard interaction along the edge in order to study their stability with respect to correlations and find ferromagnetic order in case of repulsive interaction as well as charge-density-wave order and/or additional *i*s-wave pairing for attractive couplings. A mean-field analysis that, for the first time, is formulated in terms of the Majorana edge modes suggests that any order has normal and superconducting contributions. For example, the ferromagnetic order appears in linear superposition with triplet pairing. This finding is well confirmed by the numerically exact quantum Monte Carlo investigation.

Second, we consider spinless electrons on a two-dimensional Lieb lattice that are subject to nearest-neighbor Coulomb repulsion. The low energy modes of the free fermion part

constitute a spin-1 Dirac cone that might be gapped by several mass terms. One option breaks time-reversal symmetry and generates a topological Chern insulator, which mainly motivated this study. We employ two flavors of quantum Monte Carlo methods and find instead the formation of charge-density-wave order that breaks particle-hole symmetry. Additionally, due to sublattices of unequal size in Lieb lattices, this induces a finite chemical potential that drives the system away from half-filling. We argue that this mechanism potentially extends the range of solvable models with finite doping by coupling the Lieb lattice to the target system of interest.

Third, we construct a system with four layers of a topological insulators and interlayer correlation that respects one independent time-reversal and a unitary $\mathbb{Z}_2$ symmetry. Previous studies claim a reduced topological classification from $\mathbb{Z}$ to $\mathbb{Z}_4$, for example by gapping out degenerate zero modes in topological defects once the correlation term is designed properly. Our interaction is chosen according to this analysis such that there should exist an adiabatic deformation between states whose topological invariant differs by $\Delta w = \pm 4$ in the free fermion classification. We use a projective quantum Monte Carlo algorithm to determine the ground-state phase diagram and find a symmetry breaking regime, in addition to the non-interacting semi-metal, that separates the free fermion insulators. Frustration reduces the size of the long-range ordered region until it is replaced by a first order phase transition. Within the investigated range of parameters, there is no adiabatic path deforming the formerly distinct free fermion states into each other. We conclude that the prescribed reduction rules, which often use the bulk-boundary correspondence, are necessary but not sufficient and require a more careful investigation.

Fourth, we study conduction electron on a honeycomb lattice that form a Dirac semi-metal Kondo coupled to spin-1/2 degrees of freedom on a Kagome lattice. The local moments are described by a variant of the Balents-Fisher-Girvin model that has been shown to host a ferromagnetic phase and a $\mathbb{Z}_2$ spin liquid at strong frustration. Here, we report the first numerical exact quantum Monte Carlo simulation of the Kondo-coupled system that does not exhibit the negative-sign problem. When the local moments form a ferromagnet, the Kondo coupling induces an anti-ferromagnetic mass term in the conduction-electron system. At large frustration, the Dirac cone remains massless and the spin system forms a $\mathbb{Z}_2$ spin liquid. Owing to the odd number of spins per unit cell, this constitutes a non-Fermi liquid that violates Luttinger's theorem which relates the Fermi volume to the particle density in a Fermi liquid. This phase is a specific realization of the so called 'fractional Fermi liquid' as it has been first introduced in the context of heavy fermion models.

Zusammenfassung

Durch Hinzufügen von Wechselwirkungen zu topologisch (nicht-)trivialen, freien Fermionsystemen können im Allgemeinen vier verschiedene Effekte entstehen: (i) Im Fall von symmetriegeschützen topologischen Bandisolatoren können Korrelationen durch langreichweitige Ordnung einige der schützenden Symmetrien spontan brechen, sodass die topologischen Randzustände eine Bandlücken aufweisen. (ii) In (Halb-)metallen mit freien Elektronen können Wechselwirkungen im Gegenzug langreichweitige Ordnung erzeugen, welche wiederum einen topologischen Massenterm induzieren und so eine nicht-triviale Phase dynamisch erzeugen. (iii) Korrelationen können außerdem zur Reduktion der topologischen Klassifikation freier Fermionsystemen führen, indem sie adiabatische Manipulationen zwischen zuvor verschiedenen Zuständen ermöglichen. (iv) Wechselwirkungen können langreichweitig verschränkte topologische Ordnung in Zuständen wie Quanten-Spin-Flüssigkeiten oder fraktionellen Quanten-Hall-Zuständen erzeugen, die nicht durch wechselwirkungsfreie Systeme dargestellt werden können. Im Laufe dieser Dissertation benutzen wir numerisch-exakte Quanten-Monte-Carlo Algorithmen um verschiedene Modelsysteme zu untersuchen, die (potentiell) eines der vier Szenarien darstellen.

Als Erstes untersuchen wir zwei-dimensionale, d_{xy}-Wellen, spin-singlet Supraleiter, die relevant für Hochtemperatur-Supraleiter wie den Cupraten sind. Dieses Model repräsentiert lückenlose Supraleiter und weist chirale dispersionslose Randzustände auf, die durch Zeitumkehr- und Translationssymmetrie geschützt sind. Wir führen die übliche Hubbard-Wechselwirkung entlang des Randes ein um die Stabilität in Bezug auf Korrelationen zu untersuchen und beobachten ferromagnetische Ordnung im Fall von repulsiven Wechselwirkungen sowie Ladungsdichtewellen und/oder zusätzliche *i*s-Wellen-Paarung bei attraktiven Kopplungen. Eine Molekularfeldanalyse, die zum ersten Mal bezüglich der Majorana Randzuständen formuliert wird, deutet an, dass jede Ordnung normale und supraleitende Beiträge enthält. Diese Erkenntnis wird durch die numerisch-exakte Quanten-Monte-Carlo Untersu-

chung gut bestätigt.

Als Zweites betrachten wir spinlose Elektronen auf einem zwei-dimensionalen Lieb-Gitter die der nächsten-Nachbar Coulombwechselwirkung ausgesetzt sind. Die Niedrigenergiemoden des freien Teilsystems bilden Spin-1 Dirac-Fermionen mit verschiedenen möglichen Massentermen. Bei einem davon wird die Zeitumkehrsymmetrie gebrochen und ein topologischer Chern-Isolator erzeugt, was die Hauptmotivation dieser Untersuchen darstellt. Wir verwenden zwei verschiedene Arten der Quanten-Monte-Carlo Methoden und finden stattdessen die Bildung von Ladungsdichtewellenordnung, welche die Teilchen-Loch-Symmetrie bricht. Zusätzlich führt dies, durch die verschieden großen Untergitter die Lieb-Gitters, zu einem endlichen chemischen Potential und treibt das System weg von Halbfüllung. Wir argumentieren, dass dieser Mechanismus möglicherweise die Breite von lösbaren Modellen mit endlicher Dotierung erweitert, indem das Lieb-Gitter an das Zielmodel von Interesse angekoppelt wird.

Als Drittes konstruieren wir ein System, bestehend aus vier Schichten eines topologischen Isolators, mit Wechselwirkungen zwischen den Schichten, das eine unabhängige Zeitumkehr- und eine unitäre $\mathbb{Z}_2$ Symmetrie respektiert. Vorangegangene Untersuchungen legen nahe eine von $\mathbb{Z}$ auf $\mathbb{Z}_4$ reduzierte topologische Klassifikation, zum Beispiel durch das Aufspalten entarteter Nullmoden in topologischen Defekten, sofern die Korrelationen entsprechend entworfen wurden. Unsere Wechselwirkungen sind den Regeln dieser Analysis folgend gewählt, sodass ein adiabatischer Pfad zwischen Zuständen, deren topologische Quantenzahl sich um $\Delta q = \pm 4$ unterscheiden, existieren sollte. Wir benutzen einen projektiven Quanten-Monte-Carlo Algorithmus um das Phasendiagramm des Grundzustandes zu bestimmen und erhalten, zusätzlich zum nicht-wechselwirkenden Halbleiter, einen symmetriegebrochenen Bereich der die nicht-wechselwirkenden Isolatoren voneinander trennt. Frustration reduziert die Größe dieser Region mit langreichweitiger Ordnung bis sie durch einen Phasenübergang erster Ordnung ersetzt wird. Im betrachteten Parameterbereich gibt es keinen adiabatischen Pfad, der zuvor verschiedene nicht-wechselwirkende Zustände ineinander überführt. Wir schließen daraus, dass die beschriebenen Regel zur Reduktion, die oft die Korrespondenz zwischen dem Probeninneren und dem Rand verwenden, notwendig aber nicht hinreichend sind und dass es hierzu weiterer Studien bedarf.

Als Viertes betrachten wir Leitungselektronen auf einem Honigwabengitter, die einen Dirac Halbleiter verkörpern, und Kondo-gekoppeln diese mit Spin-$1/2$ Freiheitsgraden auf einem Kagomegitter. Die lokalen Momente werden durch eine Variante des Balents-Fisher-Girvin Models beschrieben, welches nachweislich eine ferromagnetische Phase und eine $\mathbb{Z}_2$ Spinflüssigkeit bei starker Frustration beherbergt. Wir berichten hier über die erste numerisch-exakte Quanten-Monte-Carlo Simulation des Kondo-gekoppelten Systems, die kein negatives Vorzeichenproblem aufweist. Wenn die lokalen Momente einen Ferromagneten bilden, überträgt dies einen antiferromagnetischen Massenterm auf das System der Leitungselektronen. Bei starker Frustration bleiben die Dirac-Fermionen masselos und das Spinsystem bil-

det eine $\mathbb{Z}_2$ Spinflüssigkeit. Aufgrund der ungeraden Anzahl von Spin-Freiheitsgraden pro Einheitszelle stellt dies keine Fermiflüssigkeit dar und verletzt das Theorem von Luttinger, dass das Fermivolumen mit der Teilchendichte der Fermiflüssigkeit verbindet. Diese Phase ist eine spezielle Realisation der sogenannten ‘fraktionellen Fermiflüssigkeit’ die zuerst im Zusammenhang mit Schwerfermion-Systeme eingeführt worden ist.

Contents

CHAPTER 1

Introduction

In 1972, Kosterlitz and Thouless developed the theory of 'topological long-range order' in two-dimensional classical systems [1,2] that was awarded with the Nobel prize in 2016. This theory is, for example, relevant for the two dimensional XY model where the order parameter is a unit two-dimensional vector. The ground state of this model cannot exhibit a finite magnetization due to its instability with respect to low-energy spin waves [3]. However, the spin waves due not 'destroy the order' completely such that the states is critical with power-law correlation functions. Most interestingly, this critical phase persists at low but finite temperatures and exhibits a phase transition to a regular disordered phase. This phenomenon cannot be understood within the Ginsburg-Landau theory. However, there also exist topological vortex configurations, in addition to spin wave excitation, and it is their condensation, when two vortices form a bound state, that introduces the finite temperature phase transition. This seminal work introduced the notion of topology to the field on (theoretical) condensed matter physics.

The first experimental realization of topological phases of matter is the quantum Hall effect (QHE) [4]. In classical physics, an electrical current in a two-dimensional electron gas induces a perpendicular Hall conductance if one applies an external magnetic field perpendicular to the plane [5]. Interestingly, this Hall conductance is quantized at low temperatures and high magnetic fields while the applied current is dissipationless within each plateau [4]. A semi-classical analysis provides a first understanding. Classical electrons in a magnetic field move in circular cyclotron orbital that get quantized in a quantum mechanical theory. In the bulk of the sample, these orbitals are localized such that it is insulating. The electrons close to the samples boundary will hit the edge and are then reflected. This leads to conducting channels along the edge where the right- and left-movers are located on the opposite

edges such that this current is dissipationless. This constitutes one hallmark of topological phases, namely the bulk-boundary correspondence.

A first proper quantum-mechanical explanation of the QHE was presented in Ref. [6] where the authors introduced the so-called 'TKNN invariant' which quantizes the Hall plateaus. This quantity characterizes the Berry curvature of filled Landau levels in the same way as the genus g characterizes closed two-dimensional manifolds by counting its number of 'holes'. For example, a sphere as well as a bowl do not contain a 'hole' ($g = 0$) whereas the torus or a coffee mug have one of them ($g = 1$). This also illustrates the insensitivity to local details, only 'global' properties matter. This has direct consequences for the experiment, namely that the quantization of the Hall conductivity is one of the most precise experiments and vastly independent of the sample's chemical composition, disorder, lattice defects and other local deformations. Hence, it is even used to define the standard for the electric resistance in the current international system of units.

In 1988, Haldane introduced a lattice regularization of the quantum Hall effect [7] for spinless fermions on the honeycomb lattice which hosts a Dirac semi-metal when the electrons are only subject to nearest-neighbor hopping. Adding next-nearest-neighbor terms generates an insulating state by gaping the Dirac cones and either inversion or time-reversal symmetry is broken. The latter constitutes a topological state, which is nowadays also know as a Chern insulator, similar to the QHE without Landau levels or requiring an external magnetic field. However, this study received little interest until 2005 when Kane and Mele extended the model to spinful fermions where the two spin components realize opposite topological invariants such that the whole system is again time-reversal symmetric [8, 9]. The total Chern number vanishes, however, a $\mathbb{Z}_2$ valued topological index is still meaningful and the topologically non-trivial quantum spin Hall (QSH) phase, also known as two-dimensional topological insulator (TI), exhibits helical edge modes protected from back scattering due to time-reversal symmetry. This model was proposed to describe graphene, but the spin-orbit coupling, which induces the topological mass term, is too small such that graphene is a semimetal. The Kane-Mele model has only very recently been realized experimentally in bismuthene, grown on a SiC substrate, as a candidate for a high-temperature quantum spin Hall material [10]. Already in 2006, Bernevig, Hughes and Zhang proposed a different realization of the same topological phase in a quantum well structure of mercury/cadmium-telluride compounds [11] that were soon synthesized and characterized to host QSH states [12] and the first three-dimensional topological insulator was discovered in 2008 [13].

These discoveries triggered tremendous progress in the field of symmetry-protected topological phases [14–17]. The topology of gapped, free fermion models with or without non-spatial symmetries such as time-reversal (TRS), particle-hole (PHS) and the combination thereof, the chiral symmetry are fully classified as it is summarized in the 'periodic table' of topology which is also know as ten-fold way [18, 19]. For example, the QHE and the Haldane model do not obey a non-spatial symmetry, apart from the global charge conserva-

tion, and are therefore representations of the symmetry class *A* that may exhibit a $\mathbb{Z}$ valued topological invariant. The Kane-Mele model exhibits a TRS ($\mathcal{T}^2 = -1$) and falls into class *AII* with two topological distinct phases that are characterized by a $\mathbb{Z}_2$ index. This classification has been extended to also include lattice symmetries which introduced the notion of crystalline topological insulators that are protected by inversion symmetry [20–22]. Lately, an catalog of (potentially) high-quality topological materials was developed which is based on irreducible representation at high-symmetry lattice momenta [23].

This symmetry-based classification raises the question concerning the robustness of the invariants as well as the topological boundary states. In Ref. [9], the authors argued that electron interaction may induce backscattering, however, this is an *irrelevant* term that cannot open a mass gap for the helical edge mode but it might still lead to a finite edge conductivity. Interestingly, even magnetic impurities cannot have a huge effect on the edge states of the two-dimensional TI unless the interaction is very strong [24]. Actually, the site of the impurity on the edge can then be interpreted as part of the vacuum as the edge state is propagating around the impurity [25]. Similarly, the helical Majorana edge modes of topological superconductors (TSC) with time-reversal symmetry are stable with respect to weak disorder whereas they partially localize on the outermost sites and reappear in the adjacent region [26]. Zero energy flat bands, the protected boundary states of nodal TSCs, are stable with respect to edge roughness but they do acquire a finite energy from weak non-magnetic and are gapped by magnetic or strong non-magnetic disorder [27]. Interestingly, impurities may also be seen as a feature rather then an issue as they give rise to quasiparticle interference (QPI) pattern in the vicinity of dilute defects. These pattern are sensitive to the helical nature of the surface states and can be measured using Fourier-transform scanning tunneling spectroscopy [28]. Thus this technique provides valuable information about the surface states of TIs [29, 30] and it can even be used to distinguish the different topological boundary states of TSCs such as helical Majorana modes, Majorana arc states and zero-energy flat bands [31].

Combining interaction and topology can generate at least four different effects and each scenario will be discussed in more detail below:

(i) Correlation may lead to long-range order that violates the protecting symmetry and gaps the topological boundary states (see Ch. 3).

(ii) Complementary to this scenario, interactions can also induce topological non-trivial mass terms to gap a metal by spontaneous symmetry breaking (see Ch. 4).

(iii) Contrary, correlations may also reduce the topological classification of free fermions by adiabatically connecting states of formerly distinct phases (see Ch. 5).

(iv) Alternatively, interaction can give rise to states with topological order with long-range entanglement that do not have a non-interacting analog (see Ch. 6).

Several studies considered the effects of correlations on the topologically protected boundary states that originate from the bulk-boundary correspondence. As mentioned before, the Kane-Mele model exhibits helical edge modes. Adding strong repulsive density interactions leads to slowly decaying spin excitations and inelastic spin-flip processes that strongly modifies the low-energy regime of the single-particle edge spectrum such that it appears to be similar to the zigzag edge of graphene [32]. In the latter, the nodes of the bulk Dirac cones are projected to two separated momenta in the edge Brillouin zone that gives rise to a spin-degenerate flat-band edge mode[1]. It is expected that this boundary state of the topological semi-metal is even more unstable due to the high density of states at the Fermi level and indeed, both experiments [33] and theoretical studies [34, 35] show an instability towards anti-ferromagnetism along the edge as a consequence of repulsive correlations. Nodal topological superconductors exhibit similar flat-band edge states [36–39] and the particle-hole symmetry enforces a vanishing energy of these boundary. Several studies discussed possible instabilities and identified magnetic order and charge-density-wave states or additional pairing amplitudes as the most relevant scenarios in case of repulsive and attractive density interactions, respectively [40–46].

A complementary approach is based a (non-topological) metallic states which acquires a topological non-trivial mass term due to spontaneous symmetry breaking that is induced by interactions [47]. This first example of this has recently been reported in Ref. [48]. The authors used quantum Monte Carlo techniques to investigate spinful electrons on the honeycomb lattice and a specifically tailored interaction and found two different long-range ordered phases. One phase is described by the Kane-Mele model on a mean-field level and realizes the quantum spin Hall state. Interestingly, topological skyrmion excitation of the mean-field order parameter play an important role in the direct, second order phase transition to the second phase, a conventional *s*-wave superconductor. Each skyrmion carries twice the electrical charge such that their condensation generates superconductivity and the phase transition might be a realization of a deconfined quantum critical point [49, 50].

Scenario (iii) introduces the notion of symmetry protected topological (SPT) phases as (weakly) interacting states that have a finite gap to excitation, exhibit short-ranged entanglement and preserve a given set of symmetries. States that represent the same topological phase can be adiabatically deformed into each other whereas a path between topologically distinct states necessarily requires either a gap closing or a broken symmetry. Non-trivial SPT states exhibit protected boundary modes, similar to non-trivial band insulators. The spin-1 Haldane chain is considered to be one of the first examples of such a state [51]. This setup introduces deformations of topological free-fermion states which crucially depends on the interaction, i.e., the correlation effects prevent the non-interacting band gap to close without spontaneous

[1] This spectrum is readily understood if one reduces the spin-orbit coupling of the Kane-Mele model such that the Fermi velocity is decreased until the former helical edge state forms spin-full flat band when the bulk gap closes.

symmetry breaking. This gives rise to the so-called reduced topological classification.

The first example of such a reduction was designed by Fidkowski and Kitaev [52]. They considered eight chains of spinless topological superconductor that each host a single Majorana mode localized at the end of a chain [53]. Most importantly, a specifically chosen interaction term, which involves all eight modes at one end of the chain, generated a unique and symmetric ground state as well as an explicit deformation of bulk states that differ by eight in their topological invariant. Hence, the former $\mathbb{Z}$ classification is reduced to $\mathbb{Z}_8$ in the presence of correlations. This insight led to further studies of different symmetry classes and higher dimensions [54–64] that often exploit the bulk-boundary correspondence [54–56], investigate zero-dimensional topological defects [57, 58], employ the entanglement spectrum [59, 60], use braining statistics [61], or group cohomology [62].

Lastly, interaction can also generate states with topological order such as fractional quantum Hall states [65, 66], fractional topological insulators [67] or quantum spin liquids (QSL) [68–71]. So what is a (gapped) QSL? Historically, QSLs are defined as correlated spin systems that do not order at arbitrary low or zero temperature[2], however, the discussion of a *positive* definition is highly controversial, especially for gapless spin liquids. Gapped QSLs exhibit a ground-state degeneracy that depends on the genus g of the lattice or equivalently QSLs are states with long-range entanglement [74]. The following paragraph reviews the main properties of topological order, focuses on gapped $\mathbb{Z}_2$ topological order, which was first studied in Refs. [75, 76], and largely follows the review presented in Ref. [74].

The canonical model systems for a gapped QSL are the toric code [77] and the Kitaev honeycomb model [78] which also hosts a gapless QSL. A system with topological order exhibits degenerate ground states where the number of ground states depends on the boundary conditions of the model, e.g., the ground states of two-dimensional toric code are four-fold degenerate on the torus. This degeneracy also leads to a universal contribution to the entanglement entropy $S(A) \sim s_o L - \gamma$, where A is a sub-region of the lattice. The non-universal coefficient s_0 stems from the local entanglement, which is generically present in any gapped system, that gives rise to the "area law". γ is the universal contribution that depends on the ground state degeneracy, e.g., $\gamma = \ln(2)$ for the above toric code. As the entanglement entropy is manifestly positive, a positive topological contribution directly shows, that there is no local basis for which $s_0 = 0$ which illustrates the aforementioned "long-range entanglement". Interestingly, the ground-state degeneracy is also linked to exotic, gapped excitations that are known as anyons. They have to be created in pairs and each excitation is always connected to a second one via a "string", e.g., by a line of flipped spins in the toric code, which gives rise to an unusual braiding statistic. The following procedure illustrates the relation of the anyons, the boundary conditions of the lattice and the topological ground-state degeneracy. First, we create an anyon pair which costs a given energy, then move one of them around

[2] This can lead to false positive assessments, for example, when numerical simulations cannot reach the lattice sizes that are required to detect the presence of long-range order [72, 73].

of the torus' holes, and finally annihilate the anyon pair, which releases the creation energy. This non-local procedure connects the different ground states and links their number to the genus of the lattice manifold. As a final remark, let us mention the Lieb-Schultz-Mattis-Hastings theorem [79,80], according to which a gapped state of a model with an odd number of spin-$1/2$ degrees of freedom per unit cell has to exhibit topological order in the absence of symmetry breaking, i.e., there does not exist a trivial, short-range entangled, gapped and symmetric ground state.

Isakov *et.al*. investigated a hard-core boson model with topological order, a variant of the Balents-Fisher-Girvin (BFG) model [81–83], first introduced in Ref. [84], using quantum Monte Carlo techniques. This model hosts a superfluid phase, a QSL and a direct $3D\ XY^*$ transition between the two phases with a critical exponent $\eta = 1.47(3)$ that is unconventionally large [85]. This is an important results as it controls the importance of the Kondo coupling between the spin system and conduction electron [86]. Here, the Kondo coupling is irrelevant ($\eta > 1$), from a renormalization group perspective, such that the spin and conduction electrons decouple, whereas in a conventional setting, e.g., with a regular $3D\ XY$ transition ($\eta \simeq 0.038$ [87]), where the Kondo coupling remains active throughout the phase transition.

Before we discuss further aspects of Kondo coupling and topological order, let us take a step back and review more conventional Kondo models, beginning with a single Kondo impurity. In 1961, Anderson introduce a model of conduction electrons and a single, localized f-electron site and studied the emergence of a local moment when the coulomb repulsion suppresses charge fluctuations on this f-electron site [88][3]. Kondo discussed the effect of a single local moment on the resistivity of the conduction electrons and discovered that higher order spin-flip scattering generates a $\ln(T)$ contribution [92], which in case of anti-ferromagnetic spin coupling explains the minimum in $R(T)$ that has been reported by experiments [92]. However, this logarithmic contribution also posed the 'Kondo problem' as a divergent resistivity in a metal at $T = 0$ is nonphysical and cannot be found in experiments. The 'poor man's derivation of scaling laws' by Anderson [93] showed on a perturbative level that the coupling between conduction electrons and local moments increase when the temperature is reduced and thus limits the temperature range in which the analysis by Kondo is applicable. The Kondo problem was then solved using the non-perturbative numerical renormalization group approach [94] and the saturation of the resistivity is nowadays understood as the conduction electrons form a Kondo cloud which screens the magnetic impurity with spin-$1/2$ given that time-reversal symmetry is present.

Let us discuss one more intermediate step by introducing a regular lattice of local moments that are described by a Kondo lattice model. Here, the conduction electron can mediate an indirect Ruderman-Kittel-Kasuya-Yoshida (RKKY) exchange interaction between the local

[3]This model is also known as the single-impurity Anderson model (SIAM) and forms the backbone of the dynamical mean-field theory (DMFT) method [89–91]

moments that in turn might induce magnetic order [95–97]. This leads to a competition between states where the Kondo cloud screens the local moments and anti-ferromagnetic ordered states. A comparison of the associated energy scales, given by the binding energy of Kondo singlet $E_{\mathrm{K}} \sim e^{-1/|J|}$ and the energy of the AFM $E_{\mathrm{AFM}} \sim J^2$, suggest a magnetically ordered state at weak Kondo coupling J and a screening phase at strong interactions, which are separated by a quantum phase transition [98]. Indeed, a large N expansion for $SU(N)$ symmetric models yields a ground state of local Kondo singlets with a vanishing critical value $J_c = 0$ for the phase transition [99] and the RKKY interaction is only generated as a higher order corrections [100]. A unbiased quantum Monte Carlo study of the $SU(2)$ symmetric KLM on a square lattice with a half-filled conduction band [101] confirmed the AFM to Kondo singlet phase transition and interestingly showed that the screening is also finite in the AFM phase. Actually, the Kondo effect induces a finite hybridization between conduction and the localized f-electrons which gives rise to the notion of Kondo insulators and heavy Fermi liquids [102–104].

Let us now return to topological order and note that the decoupling of local moments and conduction electrons which was mentioned above, seems to violate Luttinger's sum rule [105], which states that the size of the Fermi volume cannot change with interactions, and Oshikawa's theorem [106], which showed that the local moments contribute to the Fermi sea, if the number of spins per unit cell is odd. Actually, we even expect this violation when the QSL is Kondo coupled to conduction electrons as it is stable against weak coupling due to the topological order and the finite energy gap. However, as it was pointed out in Ref. [107], Oshikawa's theorem has to be modified if the ground state is degenerate and this introduces a new phase, the socalled 'fractional Fermi liquid' (FL*) phase where electronic quasiparticles coexist with the spinon and associated topological excitations of the QSL [86,107,108].

During the course of this thesis, we study four model systems with quantum Monte Carlo methods that are motivated by the aforementioned four different scenarios for the interplay of topology and interaction as we detail below. The remainder is organized as follows:

In Chapter 2, we begin with a introduction to generic Monte Carlo techniques that focuses on potential pitfalls such as the negative-sign problem, fat tails in the distribution of observables, or autocorrelation/warmup issues and how one might overcome these challenges. Next, we illustrate two flavors of quantum Monte Carlo (QMC) algorithms, namely the continuous-time QMC method in the interaction expansion (CT-INT) [109] and the auxiliary field QMC technique (BSS) [110], and discus a logarithmic stabilization scheme to access temperature regimes and/or interaction strength which otherwise generate numerical numbers that exceed the range of double variables. We close this chapter with a few remarks on the most common observable and the detection of phase transitions and spontaneous symmetry breaking.

In Chapter 3, we define a model Hamiltonian that consists of a two-dimensional d_xy-wave

singlet superconductor, which represents a nodal TSC and hosts flat-band Majorana boundary modes, and additional Hubbard interaction along the edge. A mean-field analysis in the basis of the chiral Majorana modes shows that the mass terms of the edge states is associated with spontaneous symmetry breaking and linear superposition of normal and superconducting order parameters. This analysis is also able to identify the relevant instabilities as magnetic order, and charge-density-wave and/or additional superconductivity in case of repulsive and attractive interaction, respectively. The QMC simulation confirms this insight and is in remarkable agreement with the mean-field analysis as the high density of states and the low dimensionality of the model suggest that quantum fluctuations play an important role.

In Chapter 4, we investigate spinless fermions on a two-dimensional Lieb lattice at half-filling with repulsive nearest-neighbor density interaction. The low energy spectrum of non-interacting model represents a spin-1 Dirac cone and spontaneous breaking of TRS can generate a Chern insulator similar to the Haldane model. However, we find a finite temperature Ising phase transition with a charge-density-wave order that breaks PHS and induces a thermodynamic instability towards a filling fraction of $1/3$ or $2/3$. Interestingly, the probability distribution of the squared order parameter exhibits qualitatively different fat tails for the two QMC methods, such that the central limit theorem is inapplicable tp the CT-INT algorithm.

In Chapter 5, we design a model system in symmetry class A', which preserves a TRS and a unitary $\mathbb{Z}_2$ symmetry, such that the topology of the free fermion model is classified by a $\mathbb{Z}$ valued winding number[4]. It has been argued that a specifically chosen interaction reduces the topological classification from $\mathbb{Z}$ to $\mathbb{Z}_4$ and we test this hypothesis using a numerically exact and unbiased QMC method. Instead of an adiabatic deformation between states that differ in their winding number by 4, we find a extended region of spontaneous symmetry breaking. An attempt to frustrate the long-range order gives rise to a first order phase transition and we conclude that the previous arguments may very well be necessary but apparently not sufficient conditions for the reduced topological classification.

In Chapter 6, we consider local moments, described by a variant of the BFG model, Kondo coupled to conduction electrons on the honeycomb lattice. The spin system exhibits a phase transition from an easy-plane ferromagnet to a gapped $\mathbb{Z}_2$ QSL upon increasing the level of frustration, and the non-interaction conduction electrons form a Dirac semi-metal at half filling. As both the Dirac cone and the spin liquid are stable phases, they are expected to persist even in the presence of weak Kondo coupling. However, this constitutes a violation of Luttinger's sum rule as the Fermi surface remains 'small', in the sense that only the conduction electrons contribute, even though a 'large' surface, to which the odd number of local moments contribute as well, is required by Oshikawa's theorem. This phase of decoupled spins

[4]The two-dimensional topological insulator only preserve the TRS and spin-orbit coupling violates the conservation of S^z such that the $\mathbb{Z}_2$ topological invariant is given by spin Chern number modulo 2. Here, we require a conservation of S^z mod 2 which excludes the spin orbit coupling and the topology is defined by the $\mathbb{Z}$-valued spin Chern number.

and electrons was introduced as a ‘fractional Fermi liquid’ and we report its first numerical realization using QMC techniques.

We close this thesis with a conclusion and an outlook for future directions in chapter 7.

CHAPTER 2

Methods

Interacting fermions are showing plenty of very interesting phenomena such as spontaneous symmetry breaking, like superconductivity or magnetism, topological order as realized in fractional quantum Hall states [65, 66] or quantum spin liquids [68–71], exotic phase transitions like deconfined quantum critical points [49, 50], and much more.

In some cases, analytic solutions are possible, sometimes even exact results as for the Kitaev spin liquid [78], or approximations like the Laughlin state [111] for fractional quantum Hall systems. However, one often has to rely on numerical methods. Arguably the most famous example of an only partly solved system is the Hubbard model [112] on the two dimensional square lattice. Various methods have been developed and used to determine the phase diagram, each has its advantages and disadvantages. Exact diagonalization (ED) [113, 114] can access the full parameter space, i.e. attractive and repulsive interactions as well as finite doping. But as the size of the Hilbert space grows exponentially with the systems size, ED is limited to rather small lattices. The density-matrix-renormalization-group (DMRG) [115–117] approach was invented for one dimensional systems and nevertheless has successfully been applied to (infinite) cylinders. Here, the circumference is limited by the growing entanglement entropy that in turn determines the required bond dimension and the according numerical expense. The functional renormalization group (fRG) [118] approach can access large lattices at finite doping for repulsive interaction in order to understand the mechanism behind high T_c-superconductivity in cuprates. It is well equipped to detect leading instabilities to determine the qualitative phase diagram, but it suffers from systematic errors due to the truncation scheme.

Quantum Monte Carlo (QMC) methods are again numerically exact, overcome the exponential scaling of ED and thus enable us to study larger lattices. An increasing number

of models can be simulated without experiencing the infamous negative-sign problem (see next Sec. 2.1), e.g., the attractive Hubbard model as well as the repulsive one at half filling (on bipartite lattices). However, some models or parameter sets are not accessible due to this problem which leads to en exponential scaling of the compute time, e.g., the repulsive Hubbard model with finite doping.

In the following, we employ two flavors of fermionic quantum Monte Carlo methods, the continuous-time interaction expansion (CT-INT) [109] and the auxiliary-field (BSS) [110] algorithm (see Sec. 2.2 and Sec. 2.3). A more detailed explanation about the implementations can be found in Ref. [119, 120] for the former and Ref. [121] for the latter. The CT-INT method essentially samples Feynman diagrams with vertices in real-space and continuous imaginary time, hence the name. This version's numerical expense scales as $(L^D\beta)^3$ where β is the inverse temperature and L^D the number of interacting lattice sites. It is therefore especially adequate when the interaction is constraint only to a sub-region of the whole lattice, e.g., the one dimensional edge of a two dimensional topological material (see Ch. 3).

The second method uses auxiliary fields introduced by a Hubbard-Stratonovich transformation and provides two major advantages. First, it offers some flexibility in which channel the interaction is decomposed, e.g., whether the density and/or the spin channel is used. This influences the negative-sign-problem and, in some cases, an intelligent choice may solve this issue. Second, the algorithm's effort $(L^D)^3\beta$ also scales cubic in the number of lattice sites (including non-interacting ones), but only linear with inverse temperature. Additionally, it is possible to chose a tailored trial wave function such that a projective version quickly converges to the interacting ground state [122, 123]. This allows us to study both finite temperature aspects (Ch. 4) as well as $T = 0$ physics (Ch. 5 and Ch. 6).

2.1. Generic Monte Carlo aspects

In order to set up a Monte Carlo algorithm one has to define the configurations C in the space $\mathcal{C}$, the weight of the configuration $w(C)$ and the observable(s) $O(C)$ – here we consider only one observable for readability. Given that the weight is always positive, otherwise there is a negative-sign-problem as discussed in the next section, one can interpret $p(C) = w(C)/\sum_{C\in\mathcal{C}} w(C)$ as the probability of the configuration C. The expectation value of the observable is determined by $O = \sum_{C\in\mathcal{C}} p(C)O(C)$.

The key idea of any Monte Carlo scheme is to use a finite number N of the configurations C_i sampled according to the probability p such that $O_{\mathrm{MC}}(N) = 1/N \sum_{i=1}^{N} O(C_i)$ which clearly converges to O with increasing N. The central limit theorem governs the convergence rate, given that the distribution of the observable $O(C_i)$ has a finite variance, and states that the deviation $|O - O_{\mathrm{MC}}(N)| \sim N^{-1/2}$ for large enough N. The theorem also ensures that the Monte Carlo estimate $O_{\mathrm{MC}}(N)$ follows a Gaussian distribution, parameterized by the mean

value $O_{\mathrm{MC}}(N)$ and its standard deviation $\sigma_{O_{\mathrm{MC}}(N)}$. There are many ways to extract the error of Monte Carlo estimates, one popular option is the jackknife method. In situations where the central limit theorem does not apply, one notices fat tails in the distribution of the observable, i.e., some configurations are generated extremely rarely due to an almost vanishing weight $w(C_i)$ while having huge contributions to the measurement $O(C_i)$ (see Sec. 2.1.2).

If the probability p is known, it might be possible to sample the configurations C_i directly. However, especially in solid state physics, the weight w is given but the normalization is unknown. The Markov chain, combined with Metropolis-Hastings acceptance schemes [124, 125], allows us the sample the configurations C_i with the appropriate distribution even in this case. The crucial idea is to compare two configurations (C and C') and balance their relative probability according to their relative weight which is independent from the normalization. In practice, one usually starts from the configuration C and proposes an update to C' with probability $T(C \to C')$. Accepting this move at a rate $r = min(1, \frac{T(C' \to C)w(C')}{T(C \to C')w(C)})$ respects the detailed balance between the two configurations and, in the long run, generates the overall correct distribution of the configurations, given that all of them can be reached such that the algorithm is ergodic.

2.1.1. Sign problem

In condensed matter theory, the weight of the configuration is always extracted from the partition sum $Z = \mathrm{Tr}[\exp(-\beta\mathcal{H})]$ where β is the inverse temperature and $\mathcal{H}$ the Hamiltonian of the system at hand. The definition of the configuration is quite different in various methods but, generically, configuration with negative weight $w(C_i) < 0$ are possible. One illustrative example is the exchange of two fermions and the according minus sign in the two-dimensional worldline Monte Carlo, geometrical frustration is another common source of the negative-sign problem [126].

Even though the interpretation of the weight as a probability is not possible any more, one can use the absolute value of the weight to sample the configurations.

$$\begin{aligned} O &= \frac{\sum_{C\in\mathcal{C}} w(C)O(C)}{\sum_{C\in\mathcal{C}} w(C)} = \frac{\sum_{C\in\mathcal{C}} |w(C)|\mathrm{sign}(C)O(C)/\sum_{C\in\mathcal{C}}|w(C)|}{\sum_{C\in\mathcal{C}} |w(C)|\mathrm{sign}(C)/\sum_{C\in\mathcal{C}}|w(C)|} \\ &= \frac{\sum_{C\in\mathcal{C}} p_s(C)\mathrm{sign}(C)O(C)}{\sum_{C\in\mathcal{C}} p_s(C)\mathrm{sign}(C)} = \frac{\langle sO\rangle}{\langle s\rangle}, \end{aligned} \tag{2.1}$$

where $p_s(C) = |w(C)|/\sum_{C\in\mathcal{C}}|w(C)|$. Apparently, this change mainly recasts the problem. To visualize this, assume an observable $O(C_i)$ fluctuating around some finite value and a severe sign problem where almost half of the weights are negative. Then the average of both the sign and the sign-weighted observable almost vanish such that it is expensive to restore their finite ratio. To quantify this, note that the average sign is the ratio of two partition functions such that it scales exponentially with the euclidean system size $L^D\beta$,

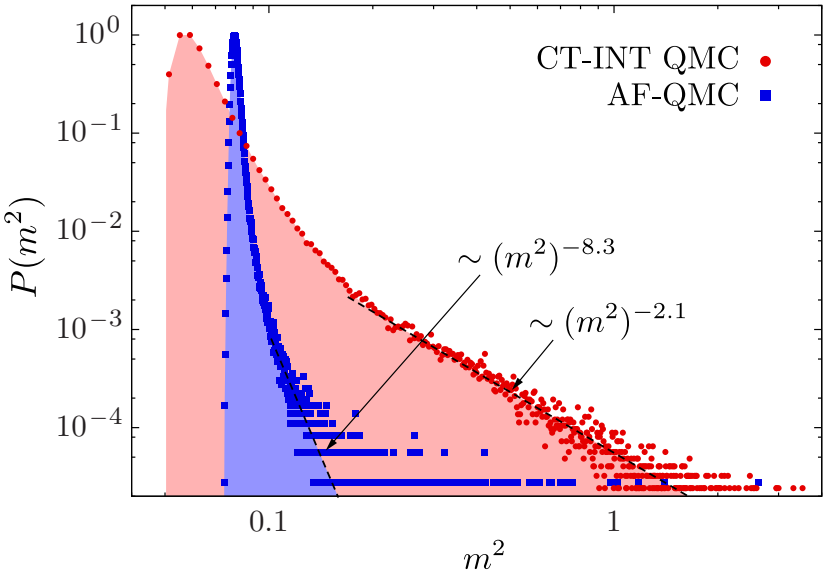

Figure 2.1.: Distribution of the (squared) order parameter for unbinned data from AF-QMC and CT-INT simulations. The data from the CT-INT simulation shows slowly decaying tails which renders the variance ill-defined. This figure is brought forward from Ch. 4 and will be discussed in more detail there.

$\langle s \rangle \sim \sum_{C \in \mathcal{C}} p_s(C)\mathrm{sign}(C) \sim \exp(-\alpha L^D \beta)$, where $\alpha \geq 0$ is an intrinsic quantity. In order to calculate the observable, the error of the sign $\sigma_s \sim N^{-1/2}$ has to be smaller than the average sign itself and this requires a compute time $T_{\mathrm{CPU}} \sim \exp(2\alpha L^D \beta)$. Hence we are left with an exponentially hard problem.

2.1.2. Fat tails

The existence of fat tails in the distribution of some observable is related to the existence of zeros in the weight function $w(C)$. Those can be possible even in the absence of the negative sign problem. The vanishing partition function and the according configuration of zero weight is never generated and therefore does not directly cause the fat tails. Instead, the configurations in the vicinity of those zeros, especially in Monte Carlo formulations with a continuous sampling degree of freedom, have arbitrarily small weight. Hence they are generated only as extremely rare events. At the same time, the contribution of those rare events to the given observable does not have to be small and could actually become arbitrarily large.

Let $P(O)$ be the probability distribution of the observable and assume that the expectation value exists because we are studying a physical system. Then $\langle O \rangle = \int_{-\infty}^{\infty} OP(O)dO$ is finite and the distribution obeys $P(|O|) \sim |O|^{2-\varepsilon}$ for large $|O|$ with $\varepsilon > 0$. This, however, is not sufficient to meet the conditions of the central limit theorem that requires a finite variance and $\varepsilon > 1$, accordingly. In Ch. 4 we face this issue for the CT-INT method whereas the fat tails

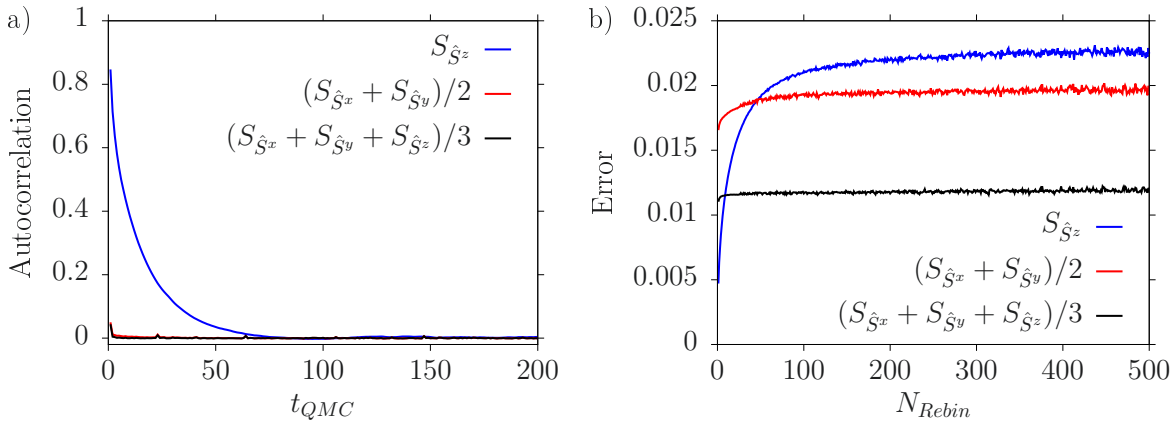

Figure 2.2.: The autocorrelation function $Auto_{\mathcal{O}}(t_{\mathrm{QMC}})$ (a) and the scaling of the error with effective bin size (b) of three equal time spin-spin correlation functions $\mathcal{O}$ of the Hubbard model in the M_z decoupling. Simulations were done on a 6×6 square lattice, with $U/t=4$ and $\beta t=6$. The original bin contained only one sweep and we calculated around one million bins on a single core. The different autocorrelation times for the xy-plane compared to the z-direction can be detected from the decay rate of the autocorrelation function (a) and from the point where saturation of the error sets in (b), which defines the required effective bin size for independent measurements. Apparently, the improved estimator $(S^x+S^y+S^z)/3$ has the smallest autocorrelation time. This figure has been taken from Ref. [127].

are absent when we use the BSS algorithm, as apparent from the copied and moved forward Fig. 2.1. One explanation for this difference is the discrete character of the configuration space for BSS such that the configurations cannot be arbitrarily close to the zeros of the partition function compared to the continuous space of CT-INT.

2.1.3. Warmup, autocorrelation & error analysis

The Markov chain method is an extremely useful way to simulate unnormalized weight distributions. However it often requires somewhat small changes between two configurations such that the weights of them are similar and the proposed move is accepted often enough. Due to those small variations, a certain number of updates is required to generate a new independent configuration and the time scale associated with this is commonly known as the auto-correlation time t_{auto}. Due to the generically random starting point within the configuration space, the simulation has to run longer than at least a few auto-correlation times in order to generate equilibrium configurations before evaluating any observable.

In Fig. 2.2(a), we present a representative plot of the auto-correlation function

$$Auto_{\mathcal{O}}(t_{\mathrm{QMC}}) = \sum_{i=0}^{N-t_{\mathrm{QMC}}} \frac{(O_i-\langle\mathcal{O}\rangle)\left(O_{i+t_{\mathrm{QMC}}}-\langle\mathcal{O}\rangle\right)}{(O_i-\langle\mathcal{O}\rangle)(O_i-\langle\mathcal{O}\rangle)} \tag{2.2}$$

with the shorthand notation $O_i = O(C_i)$. Here we use the BSS algorithm for the two dimensional Hubbard model and analyze various spin operators as observable O. This clearly shows that there is not one unique time scale. Instead the auto-correlation time depends on the given observable of interest.

This effect also influences the error analysis such that one tends to underestimate the true uncertainty of the Monte Carlo average. Therefore, let us briefly review the jackknife error estimation. The so-called jackknife bins are defined as $O_{(i)} = (N-1)^{-1} \sum_{k \neq i} O_k$, where we drop the i^{th} original data point. The expectation value of the observable is $\langle \mathcal{O} \rangle = N^{-1} \sum_i O_{(i)}$ and here it is important to first generate the jackknife bins before any further evaluation, e.g., before taking the ratio in $\langle sO \rangle / \langle s \rangle$ when the negative-sign problem is present. The standard error, including bias correction, is given by $\sigma^2_{O_{\text{MC}}(N)} = \frac{N-1}{N} \sum_i [O_{(i)} - \langle \mathcal{O} \rangle]^2$. When the simulation exhibits considerable auto-correlation times, then the measured data points O_i do not fluctuate as much as independent samples are supposed to. Hence, the overall standard error $\sigma_{O_{\text{MC}}(N)}$ is too small. However, it is possible to generate less correlated bins by averaging over N_{Rebin} of the original data, $O_I = \sum_{k=0}^{N_{Rebin}-1} O_{k+I N_{Rebin}}$. This procedure is also know as rebinning and often performed within the Monte Carlo algorithm as it reduces the storage requirements and writing to disk operations. Using this rebinned data in the jackknife analysis approaches the correct value of $\sigma_{O_{\text{MC}}(N)}$ once the rebinning is larger then the auto-correlation time, as apparent in Fig. 2.2(b).

For some Monte Carlo methods, global updates have been successfully designed to solve this challenge, both for fermionic and bosonic methods. Celebrated examples are the Wolf and the Swendsen-Wang algorithms [128, 129] which solved the Ising model, allowing to determine precise critical exponents of the phase transition, or the worm/loop updates in the context of the stochastic series expansion [130–133]. However, for the two fermionic methods, introduced in the following, such generic global moves have not been established.

In summary, we have discussed that Monte Carlo algorithms stochastically sample the important configuration efficiently such that formerly exponentially hard problems can be solved in polynomial compute time given that the negative-sign problem is absent. Additionally, we presented two major pitfalls that have to be considered during Monte Carlo simulations. (1) Some observables may exhibit *fat tails* in their probability distribution such that the computation is becoming quite expensive and – in the extreme case – the central limit theorem might not apply. Here, the conventional error analysis is misleading as the underlying distribution, assumed when reporting the mean value and the standard error, is not Gaussian any more. (2) Additionally, some observables might have long *auto-correlation times*. Then, the error estimate is typically to optimistic such that the results appear to be more precise than they actually are. Related to this are the *warmup times* that control the convergence rate of the observable's expectation value, starting from a random configuration/value to the correct result.

2.2. Continuous-time quantum Monte Carlo (CT-INT)

The partition function $Z = \mathrm{Tr}[\exp(-\beta\mathcal{H})]$ is the defining quantity in statistical mechanics and used to derive the configuration space with the according weights for the quantum Monte Carlo algorithm. This procedure is not unique and there are various approaches, some use above form and are referred to as operator-based methods whereas others, including the CT-INT algorithm, are action based and require the path integral formulation of the partition function $Z = \int \mathcal{D}\{\psi,\bar{\psi}\}\exp[-S(\psi,\bar{\psi})]$ with $S(\psi,\bar{\psi})$ being the action as a function of the fermionic field $\psi(x,\tau)$ and its complex conjugate $\bar{\psi}(x,\tau)$.

In the next step, the action is split into a non-interacting part $S_0(\psi,\bar{\psi})$, which may contain any terms up to the second power of the fields, and the interaction $S_{\mathrm{int}}(\psi,\bar{\psi})$, which collects the remaining contributions, such that $S(\psi,\bar{\psi}) = S_0(\psi,\bar{\psi}) + S_{\mathrm{int}}(\psi,\bar{\psi})$. For concreteness, let us use the spinful, $SU(2)$-symmetric Hubbard model at half filling with

$$S_0(\psi,\bar{\psi}) = -\sum_{x,y,\sigma}\iint_0^\beta \bar{\psi}_\sigma(x,\tau)G_0^{-1}(x-y,\tau-\tau')\psi_\sigma(y,\tau')d\tau d\tau' \tag{2.3}$$

$$S_{\mathrm{int}}(\psi,\bar{\psi}) = U\sum_{x,s}\int_0^\beta [\bar{\psi}_\uparrow(x,\tau)\psi_\uparrow(x,\tau) - 1/2 + s\alpha_\uparrow]\times [\bar{\psi}_\downarrow(x,\tau)\psi_\downarrow(x,\tau) - 1/2 + s\alpha_\downarrow]\,d\tau \tag{2.4}$$

where $G_0(x,y,\tau)$ is the non-interacting Greens function, that encodes the details of the lattice, the single particle hopping elements as well as the chemical potential. Note that the term $s\alpha$, once summed over s, adds a constant to the action of the original Hubbard action without α. This only influences the overall (unknown) normalization, it does not change the physics but allows choices of α to avoid possible sign problems [134].

In the last step, we expand the partition function in powers of the coupling strength U,

$$Z = \sum_{n=0}^{\infty}\prod_{i=1}^{n}\left[\sum_{x_i,s_i}\int_0^\beta d\tau_i\right]\frac{(-U)^n}{n!}\int\mathcal{D}\{\psi,\bar{\psi}\}T(\exp[-S_0(\psi,\bar{\psi})]\prod_{i=1}^{n}v(x_i,s_i,\tau_i)) \tag{2.5}$$

$$= Z_0\sum_{n=0}^{\infty}\prod_{i=1}^{n}\left[\sum_{x_i,s_i}\int_0^\beta d\tau_i\right]\frac{(-U)^n}{n!}\left\langle\prod_{i=1}^{n}v(x_i,s_i,\tau_i)\right\rangle_0 \tag{2.6}$$

$$= Z_0\sum_{C\in\mathcal{C}}\frac{(-U)^n}{n!}\left\langle\prod_{i=1}^{n}v(x_i,s_i,\tau_i)\right\rangle_0 . \tag{2.7}$$

Here we have introduced the shorthand notation for the vertex $v(x_i,s_i,\tau_i) = \prod_{\sigma=\uparrow,\downarrow}[n_\sigma(x_i,\tau_i) - 1/2 + s_i\alpha_\sigma]$, $T(\dots)$ refers to the time ordering for fermion fields and we also use the abbreviation $\langle\dots\rangle_0 = Z_0^{-1}\int\mathcal{D}\{\psi,\bar{\psi}\}T(\dots\exp[-S_0(\psi,\bar{\psi})])$ for non-interacting expectation values. The comparison of the last two lines in the equation above identifies the configu-

ration space as lists of the vertex positions $\{x_i, s_i, \tau_i\}$ for a given order n such that $C = \{n, \{x_1, s_1, \tau_1\}, \cdots, \{x_n, s_n, \tau_n\}\}$. The weight of each configuration can also be inferred as $w(C) = \frac{(-2U)^n}{n!} \langle \prod_{i=1}^n v(x_i, s_i, \tau_i) \rangle_0$. Observe that the expectation value is taken with respect to the non-interacting system. In most cases, the model is conserving the particle number[1] such that the weight can be expressed as a determinant of a matrix M. For simplicity, let us exploit the $SU(2)$ symmetry such that the spin sectors completely decouple and we have $\det M = \det M^{\uparrow} \det M^{\downarrow}$ with the matrix elements $M^{\sigma}_{ij} = G_0(x_i - x_j, \tau_i - \tau_j) - \delta_{ij}(1/2 - s_i \alpha_{\sigma})$ with $i, j \in \{1, n\}$.

The configuration space then also suggest the update moves used to construct the Markov chain, namely the addition and the removal of one or more vertices. The Metropolis scheme requires the ratio $w(C')/w(C)$, that compares the determinants of two matrices which have almost equal dimension. This can be done in a very efficient and numerically stable manner by using the fast update schemes presented in Refs. [119, 120]. These two moves allow us to explore the full configuration space and are therefore ergodic. Nevertheless, it is beneficial to also propose updates of the auxiliary variable s_i of the i^{th} vertex due to the low computational cost of this move.

Last, but not least, we discuss the measurement of observables. For a given configuration C, we take all expectation values with respect to a non-interacting theory and Ref[David] has shown that Wick's theorem can then be used to calculate any higher-order correlation function from the single-particle Green's function of that configuration C. This leads to the basic building block

$$\langle\langle \bar{\psi}_{\sigma}(x, \tau) \psi_{\sigma}(y, \tau') \rangle\rangle_C = \frac{\langle \bar{\psi}_{\sigma}(x, \tau) \psi_{\sigma}(y, \tau') \prod_{i=1}^n v(x_i, s_i, \tau_i) \rangle_0}{\langle \prod_{i=1}^n v(x_i, s_i, \tau_i) \rangle_0} . \tag{2.8}$$

Note, that the Greens function $\langle\langle \bar{\psi}_{\sigma}(x, \tau) \psi_{\sigma}(y, \tau') \rangle\rangle_C$ again is a ratio of matrices with almost equal dimension such that we can once more profit from the fast update scheme.

The purpose of this section has been to present the main ideas and concepts of the CT-INT algorithm and show that this QMC method samples all possible Feynman diagrams by adding and removing vertices. A more detailed discussion is presented in Refs. [119, 120] and readers, who are interested in developing their own implementation, are referred to those manuscripts.

[1] In Ch. 3, we will discuss a superconducting system such that the particle number is not conserved. However, we can utilize another global $U(1)$ symmetry related to the conservation of S^z in spin-singlet superconductors.

2.3. Auxiliary-field quantum Monte Carlo (BSS)

In contrast to the above action-based CT-INT method, the auxiliary-field algorithm is operator-based. The partition function is again the starting point of the derivation. Let us use the same Hubbard model to illustrate the key setup of the method, this time from the Hamiltonian perspective, $\mathcal{H} = \mathcal{H}_0 + U\sum_x (n_{x,\uparrow} + n_{x,\downarrow} - 1)^2$. First, we perform a Trotter decomposition [135–137]

$$\begin{aligned} \exp(-\beta\mathcal{H}) &= [\exp(-\Delta\tau\mathcal{H})]^{L_{\text{Trott}}} && (2.9)\\ &= [\exp(-\Delta\tau\mathcal{H}_0)\prod_x \exp(-\Delta\tau U(n_{x,\uparrow}+n_{x,\downarrow}-1)^2)]^{L_{\text{Trott}}} + \mathcal{O}(\Delta\tau^2)\,, && (2.10)\end{aligned}$$

with $\Delta\tau = \beta/L_{\text{Trott}}$. $\mathcal{H}_0$ describes the non-interacting part of the system, just like S_0 in the previous section.

As the interaction is a perfect square, we can use a discrete version of the Hubbard-Stratonovich transformation for an operator $\mathcal{A}$

$$\exp(-\Delta\tau U\mathcal{A}^2) = \frac{1}{4}\sum_{s=\pm1,\pm2} \gamma(s)\exp(\sqrt{-\Delta\tau U}\,\eta(s)\mathcal{A}) + \mathcal{O}(\Delta\tau^4)\,, \qquad (2.11)$$

given that $\gamma(\pm1) = 1+\sqrt{6}/3$ and $\gamma(\pm2) = 1-\sqrt{6}/3$ as well as $\eta(\pm1) = \pm\sqrt{2(3-\sqrt{6})}$ and $\eta(\pm2) = \pm\sqrt{2(3+\sqrt{6})}$. We perform this transformation for each interaction term, indexed by the real-space position x here, and for each time-slice indexed by $1 \le \tau \le L_{\text{Trott}}$. Hence, this leads to a space-time dependent auxiliary field $s_{x,\tau}$. As a result, we can write the partition function

$$\begin{aligned} Z &= \text{Tr}[\exp(-\beta\mathcal{H})] && (2.12)\\ &\sim \sum_{s_{x,\tau}} \text{Tr}\left[\prod_\tau B_\tau(s_{x,\tau})\right] \quad \text{with} && (2.13)\\ B_\tau(s_{x,\tau}) &= \exp(-\Delta\tau\mathcal{H}_0)\prod_x \gamma(s_{x,\tau})\exp(\sqrt{-\Delta\tau U}\,\eta(s_{x,\tau})(n_{x,\uparrow}+n_{x,\downarrow}-1)). && (2.14)\end{aligned}$$

This equation nicely illustrates the configuration space of the BSS method that is given by the auxiliary fields $s_{x,\tau}$. The weight of each field configuration is determined by the Tr in the fermionic Fock space. The trace can be reduced to a determinant in the single-particle Hilbert space $\text{Tr}[\prod_\tau B_\tau(s_{x,\tau})] = \det[1+\prod_\tau B_\tau(s_{x,\tau})]$ as, for a given field configuration, we are left with a non-interacting Gaussian theory. The updating scheme then proposes to change the field configuration by modifying one single $s_{x,\tau}$ for a given position x and time τ.

Similar to the CT-INT algorithm we can once more use Wick's theorem to calculate any other higher order correlation function from the knowledge of the single-particle Green's function. For more details, especially on the stabilization schemes required due to the expo-

nentially large and small scales in $\exp(-\beta\mathcal{H})$ as well as the calculation of the single-particle Green's function, the interested reader is referred to Ref. [121, 138].

Before we move on to the next section, let us briefly discuss the projective version of this method that allows us to access ground state physics more efficiently then by simply lowering the temperature of the system ($\beta \to \infty$). The key idea is to use a trial wave function $|\Psi_{\text{trial}}\rangle$ and to project this state to the interacting ground state by applying the exponentiated Hamiltonian $\exp(-\Theta\mathcal{H})|\Psi_{\text{trial}}\rangle = \exp(-\Theta E_{\text{GS}})\sum_n \exp(-\Theta(E_n - E_{\text{GS}}))|n\rangle\langle n|\Psi_{\text{trial}}\rangle$. Here $|n\rangle$ is an eigenstate of the full Hamiltonian with energy E_n and E_{GS} is the energy of the ground state. This clearly shows that any excitation is suppressed exponentially fast upon increasing the parameter Θ. The overlap $\langle n|\Psi_{\text{trial}}\rangle$ of the trial wave function and the eigenstates is both a great feature but also a caveat to be considered. On the positive site, we have the freedom to choose a 'good' trial wave function. If, for example, the ground state is known to be a spin-singlet and the lowest excitation are triplet excitation, we can choose a singlet as a trial wave function without any triplet component, thus increasing the effective gap and accordingly the convergence rate. On the negative side, however, one can accidentally define a trial wave function that does not overlap with the true ground state at all and thereby produce wrong results. The implementation of this idea is rather simple as one essentially replaces the trace in the weight by the trial wave function and adds the projection length, $\text{Tr}[\ldots] \to \langle\Psi_{\text{trial}}|\exp(-\Theta\mathcal{H})\ldots\exp(-\Theta\mathcal{H})|\Psi_{\text{trial}}\rangle$. Also, this projection scheme allows us to focus solely on the lowest energy state and the numerical calculations are thus more stable than the finite temperature version.

Logarithmic stabilization scheme

Increasing the inverse temperature introduces a challenge for the numerical stability of the algorithm. Here we have to control the various scales of $A_j = \prod_{\tau=0}^{j} B_\tau$ where B_τ is the product of all exponentiated operators on the i^{th} time slice, as defined in the previous section. Apparently, some models, e.g., in Ch. 6 generate Eigenvalues in A_j which exceeded the range of double precision of order $10^{\pm 308}$. To overcome this issue, we store the scale of A_j on a logarithmic axis and implemented the following stabilization scheme. Assume that we already have a QR decomposition of $A_{j-1} = Q_{j-1}e^{\lambda_{j-1}}R_{j-1}$ where Q_{j-1} is the orthogonal part, $e^{\lambda_{j-1}}$ is diagonal and separates the main scales, and R_{j-1} encodes their mixing. To generate the QR decomposition of $A_j = B_j A_{j-1}$ we perform the following steps:

1. Calculate $\tilde{M}_j = B_j Q_{j-1}$.
2. Use the permutation P_j to sort the columns of $M_j = \tilde{M}_j P_j$ according to the column norm of $M_j e^{\lambda_{j-1}}$. Permute λ_{j-1} and R_{j-1} with P_j^{-1} to correct this manipulation.
3. Perform a QR decomposition of $M_j = Q_j \tilde{R}_j$ without further pivoting.

4. Extract the scales of $\tilde{R}$ as $(D_j)_n = |(\tilde{R}_j)_{nn}|$.

5. Determine the new scales $\lambda_j = \log(D_j) + \lambda_{j-1}$.

6. Calculate $R_j = D_j^{-1} e^{-\lambda_{j-1}} \tilde{R}_j e^{\lambda_{j-1}} R_{j-1}$.

This scheme keeps all the advantages of QR decomposition with pivoting to handle exponentially large and small scales of A_j which is paramount to a stable BSS algorithm, even when double precision suffices. Here, the key point is not store the scales as D's but rather as $e^{\lambda_{j-1}}$ as to handle values that are much larger than $10^{\pm 308}$.

2.4. How to detect symmetry breaking and phase transitions numerically?

Spontaneous symmetry breaking occurs, when the Hamiltonian respects a certain symmetry, e.g., the $SU(2)$ symmetry in the Hubbard model, whereas the ground state does not, as it is spontaneously chosen from a degenerate set of ground states with a vanishing transition probability from one ground state to another in the thermodynamic limit. The partition function is by design respecting the symmetries of the Hamiltonian and consequently an ergodic Monte Carlo has to do so as well. However, we have to distinguish two scenarios here. On one hand, the symmetry can be conserved by each configuration C_i, e.g., when we use the density channel Hubbard-Stratonovich decomposition for the BSS algorithm. On the other hand, individual configurations C_i may break the symmetry, but then there exists one or more symmetry related configurations $\tilde{C}_i$s that have equal weight and that restores the symmetry on average, e.g., when we use the spin channel for the decomposition[2].

Consequently, it is impossible to determine symmetry breaking order parameters directly. However, we can access the according correlation function of the operators $\mathcal{A}$ and $\mathcal{B}$, defined by

$$C_{\mathcal{A},\mathcal{B}}(d) = \frac{1}{L}\sum_{x}^{L}\left(\langle \mathcal{A}_x^\dagger \mathcal{B}_{x-d}\rangle - \langle \mathcal{A}_x^\dagger\rangle\langle \mathcal{B}_{x-d}\rangle\right) \tag{2.15}$$

$$C_{\mathcal{A},\mathcal{B}}(q) = \sum_{d}^{L} e^{iqd} C_{\mathcal{A},\mathcal{B}}(d)\,, \tag{2.16}$$

for real and momentum space, respectively. A sketch of correlation functions is shown in Fig. 2.3. In the disordered phase, the correlation function decays exponentially with distance

[2] In these cases, the phenomenon of critical slowing down might occur, when the time-scale associated with the symmetry restoration is diverging. This typically occurs when global moves, e.g., a global rotation of the spins relate the configuration partners, while the updating scheme only includes local moves. The local moves in principle may also restore the symmetry, however they have to overcome an exponentially large (with euclidean volume) energy barrier and the accordingly small acceptance probability.

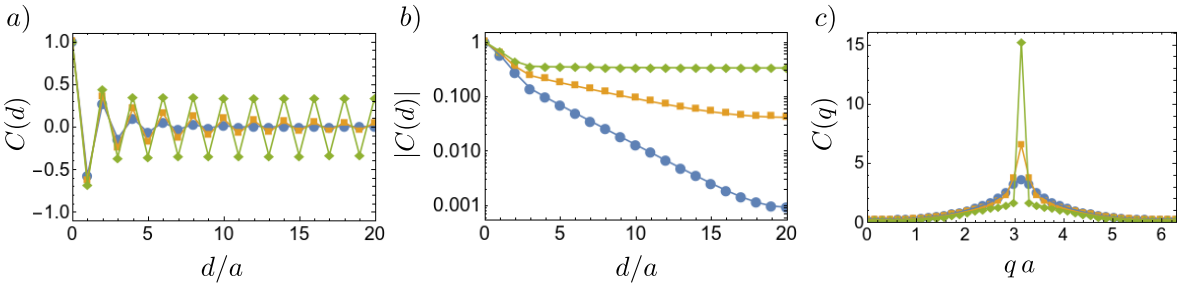

Figure 2.3.: Sketch of correlation functions in real (panels (a) and (b)) and momentum space (panel (c)) with various correlation length scales. The green diamonds represent long-range order with a non-analytical (divergence) behavior at q_{inst}, the associated wave vector.

d as represented by the blue and orange curve. Hence every value $C_{\mathcal{A},\mathcal{B}}(q)$ remains finite as we approach the thermodynamic limit $L \to \infty$. In a symmetry broken phase, however, far apart observables are still related to each other, represented by the green data points. The correlation function then remains finite for large distances d (see Fig. 2.3(b)) and the Fourier transformation generates a linear divergence with system size L at specific momenta q_{inst} as in Fig. 2.3(c). This enables the detection of the absolute value of the mean-field like order parameter $m = \sqrt{L^{-1} C_{\mathcal{A},\mathcal{A}}(q_{inst})}$. For example, the spin-spin correlation function with $\mathcal{A} = S$ signals ferromagnetically ordered states with an instability at $q_{inst} = 0$, as well as anti-ferromagnetic order with $q_{inst} = \pi$, assuming a one dimensional model system.

First order transitions

In general, the transition between two phases can be of first or second order, distinguished by a discontinuous jump in the first or in higher derivatives of the free energy F with respect to the tuning parameter g. In the canonical ensemble, the free energy is defined as $F = -\beta^{-1} \ln(Z)$ with Z being the canonical partition sum. Observe that the projective version of the BSS algorithm explicitly fixes the number of particles by specifying the trial wave function. Technically, the finite temperature version as well as the CT-INT method do not fix the number of particles, but rather specify a chemical potential μ such that the methods sample the grand-canonical partition function. However, most of the time, we use particle-hole symmetry to avoid sign-problems during the remainder of this thesis. The chemical potential is therefore set to $\mu = 0$ and the two partition functions are indistinguishable. Taking again the Hubbard model as an example and using the interaction strength as the tuning parameter $g = U$, the first derivative of the free energy is given as

$$\frac{\partial F}{\partial U} = -(\beta Z)^{-1} \operatorname{Tr}\left[\exp(-\beta \mathcal{H}) \sum_x (n_{x,\uparrow} + n_{x,\downarrow} - 1)^2\right] = -(\beta U)^{-1} \langle \mathcal{H}_{\text{pot}} \rangle , \tag{2.17}$$

where we introduced the potential energy $\mathcal{H}_{\text{pot}} = U \sum_x (n_{x,\uparrow} + n_{x,\downarrow} - 1)^2$ in the last line.

Second order phase transitions

Second order phase transitions, on the other hand, display a non-analytic but continuous behavior in both the first derivative $\frac{\partial F}{\partial g}$ as well as the order parameter $m(g)$. Here it is useful to define a correlation ratio

$$r = 1 - \frac{C_{\mathcal{A},\mathcal{A}}(q_{inst} + \delta)}{C_{\mathcal{A},\mathcal{A}}(q_{inst})}, \tag{2.18}$$

where δ is an increment of the lattice in momentum space ($\delta \sim 1/L$). For the disordered phase, $C(q)$ is an analytic function such that $r \to 0$ with increasing lattice size $L \to \infty$ (compare Fig. 2.3(c)). For a ordered phase, in contrast, the ratio converges to 1 in the thermodynamic limit. Right at the critical point of the phase transition this ratio is lattice size independent as it is an renormalization-group invariant quantity that follows the scaling ansatz

$$r = f((U - U_c)/U_c L^{1/\nu}) \tag{2.19}$$

for the vicinity of the critical point. $f(x)$ is a non-universal, analytic function and U_c the critical value of the coupling strength, again for the Hubbard model as an example, locating the phase boundary. The order parameter obeys a similar scaling ansatz, however, the order parameter itself is not RG invariant and therefore requires an additional critical exponent β. Then $m = L^{-\beta/\nu} g((U - U_c)/U_c L^{1/\nu})$ for quantum phase transitions and $m = L^{-\beta/\nu} h((T - T_c)/T_c L^{1/\nu})$ for finite temperature phase transitions with a critical temperature T_c.

Spectral functions

Last but not least, the single-particle Green's function and the according spectra are interesting observables. Hence, let us define the imaginary-time resolved Green's function

$$\begin{aligned} G(k,\tau) &= \langle c_k(\tau) c_k^\dagger(0) \rangle & (2.20)\\ &= Z^{-1} \sum_{n,m} e^{+\tau(E_n - E_m)} e^{-\beta E_n} \langle n|c_k|m\rangle \langle m|c_k^\dagger|n\rangle & (2.21)\\ &= \int_{-\infty}^{\infty} A(k,\omega) K(\omega,\tau) d\omega\,. & (2.22) \end{aligned}$$

The second line (Eq. (2.21)) is the Lehmann representation where n and m label eigenstates of the full interacting system. This illustrates the connection of the Green's function with the matrix elements of the single-particle creation/annihilation operators. To make the connection with the maximum entropy method, we expressed the propagator in terms of the fermion kernel $K(\omega,\tau) = \exp(-\tau\omega)/(1+\exp(-\beta\omega))$ where β is again the inverse temperature. The stochastic maximum-entropy method [139, 140] solves the last equation from above. This is required as we can only measure $G(k,\tau)$ on the imaginary time axis, but ultimately, we are

interested in the spectrum as a function of real frequencies ω,

$$A(k,\omega) \quad = \quad Z^{-1}\sum_{n,m}(e^{-\beta E_n}+e^{-\beta E_m})|\langle n|c_k|m\rangle|^2\delta(\omega-(E_m-E_n))\,. \tag{2.23}$$

Let us assume very low temperature (large β) to develop an intuition for the spectrum $A(k,\omega)$. Here we can approximate $Z^{-1}e^{-\beta E_n}$ as $\delta(E_n-E_0)$ such that either the state n or m has to be a ground state with energy E_0. Then we have

$$\lim_{\beta\to\infty} A(k,\omega) = \sum_n(\delta(\omega-\Delta E)|\langle n|c_k^\dagger|0\rangle|^2+\delta(\omega+\Delta E)|\langle n|c_k|0\rangle|^2) \tag{2.24}$$

with $\Delta E = E_n - E_0 > 0$ such that we can associate any contribution with positive frequency to particle excitation from the ground state to another eigenstate n whereas the negative frequencies stem from hole excitations.

CHAPTER 3

Edge instabilities of topological superconductors

The discovery of topological insulators [11–13] has established the existence of novel surface states [14–17] that are protected by their non-trivial bulk topology. Some of those boundary states exhibit a flat dispersion relation and thus are highly susceptible to correlation effects [33–35, 40–46, 141, 142]. These surface states may occur in topological semi metals [142–144] as well as in nodal topological superconductors [36–39]. In the latter, particle-hole-symmetry (PHS) enforces the energy of the flat band to vanish and gives rise to the notion of neutral Majorana bands [39, 145, 146].

Looking at the surface Brillouin zone, the flat bands are terminated by the projection of the bulk Fermi surface. Depending on the dimensionality of the enclosed area, this gives rise to an extensive ground state degeneracy g which diverges linearly (1D) or quadratically (2D) with system size. This is in violation of the third law of thermodynamics, which states that the entropy $S = k_B \ln g$ has to vanish (unique ground state) or remain constant (topological order or glassy phases) at absolute zero. As a consequence, arbitrarily weak interaction gap the topologically protected boundary modes and induce novel symmetry broken states at the surface [33–35,44–46,141,142,147]. Due to the low dimensionality of the surface states and their macroscopic degeneracy, fluctuations around mean-field saddle points should be taken into account [148].

Here, we use quantum Monte Carlo techniques [109, 119] to investigate the stability of flat-band surface states in d_{xy}-wave spin-singlet superconductors with respect to interactions. This model is relevant for high-temperature cuprate SCs [149, 150]. Tunnel junction experiments on the normal-metal $YBa_2Cu_3O_{7-x}$ exhibits a sharp zero-bias peak for intermediate temperatures [151–157] that is interpreted as a signature of flat-band edge states. This peak then splits into two finite-bias peaks at lower temperatures [158, 159] that is considered as

a sign of spontaneous symmetry breaking. However, experiments do not always report the splitting of the zero bias peak at the lowest temperatures [160].

In this project, we (i) refine the mean-field analysis by using a Majorana basis compared to previous works using complex fermion operators [40–45] that provides new insights to a hierarchy of fermionic correlations, and (ii) include all fluctuations by employing the numerically exact continuous-time QMC (see Sec. 2.2). Any Majorana bilinear mass term, which gaps out the boundary modes, breaks the physical time-reversal and/or translation symmetry. In the Monte Carlo simulation, we find long-range order in coherent superposition of normal and superconducting operators in agreement with the hierarchy developed on the mean-field level. For repulsive interaction, the anti-ferromagnetic order is combined with triplet superconductivity, whereas, for attractive interaction, we find s-wave singlet SC mixed with spontaneous current order and/or charge-density-waves (CDW) in superposition with singlet cooper pairing of finite momentum.

This study was carried out under the supervision of F. F. Assaad and A. P. Schnyder and the following results of this project have been published in Ref. [P1]. This chapter contains reprinted figures with permission from Ref. [P1].

3.1. Model

We start from a phenomenological model system of d_{xy}-wave superconductors in two dimension using the Bogoliubov–de Gennes Hamiltonian $\mathcal{H}_0 = \sum_{\mathbf{k}} \Psi^\dagger_{\mathbf{k}} H(\mathbf{k}) \Psi_{\mathbf{k}}$, with the Nambu spinor $\Psi_{\mathbf{k}} = (c_{\mathbf{k}\uparrow}, c^\dagger_{-\mathbf{k}\downarrow})^{\mathrm{T}}$ and

$$H(\mathbf{k}) = \begin{pmatrix} \varepsilon_{\mathbf{k}} & \Delta_{\mathbf{k}} \\ \Delta^*_{\mathbf{k}} & -\varepsilon_{-\mathbf{k}} \end{pmatrix}. \tag{3.1}$$

The operator $c^\dagger_{\mathbf{k}\sigma}$ creates an electron of spin σ and momentum $\mathbf{k} = (k_\parallel = k_x, k_\perp = k_y)^{\mathrm{T}}$. This labeling of momenta already anticipates the later introduced ribbon geometry with open boundary conditions in the y- and periodic ones for the x-direction (see Fig. 3.1). The normal state dispersion relation is given by $\varepsilon_{\mathbf{k}} = -2t\,(\cos k_\parallel + \cos k_\perp) - \mu$ with the hopping integral t and the chemical potential μ. The contribution $\Delta_{\mathbf{k}} = \Delta_{d_{xy}} \sin k_\parallel \sin k_\perp$ introduces d_{xy}-wave spin-singlet superconductivity with a pairing amplitude $\Delta_{d_{xy}}$.

To discuss the topology of this two-dimensional nodal system, we interpret $H\left(k_\parallel, k_\perp\right)$ as a set of fully gapped one-dimensional chains $H_{k_\parallel}(k_\perp)$, indexed by $k_\parallel$. Each subsystem belongs to the class BDI and its topology is classified by a winding number. If $2|t| > |\mu_{k_\parallel}|$ and $\Delta_{k_\parallel} \neq 0$, the subsystem exhibits a nontrivial bulk topology and hosts protected zero energy edge states (created by $\gamma^\dagger_{k_\parallel}$) once open boundary conditions for the perpendicular direction $k_\perp$

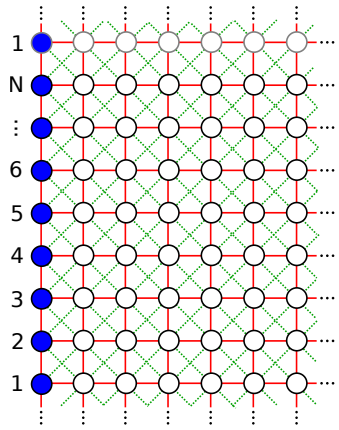

Figure 3.1.: Visualization of the square lattice in ribbon geometry: normal hopping terms along nearest neighbor bond (solid red), superconducting d_{xy}-wave pairing on next-nearest neighbor bonds (dashed greed), on-site chemical potential in the bulk and interactions along the edge (filled blue circles). We assume periodic boundary conditions in the parallel x-direction and open ones for the perpendicular y-direction

are imposed. Here we use the shorthand notations $\mu_{k_\parallel} = \mu + 2t\cos(k_\parallel)$ and $\Delta_{k_\parallel} = \Delta_{d_{xy}}\sin(k_\parallel)$.

The aim of the project is to study correlation effects of these Majorana edge states. Hence, we add the conventional Hubbard interaction along the top edge ($i_{\perp,0} = 1$) by refining the Hamiltonian to $\mathcal{H} = \mathcal{H}_0 + \mathcal{H}_{\text{int}}$ with

$$\mathcal{H}_{\text{int}} = -\frac{2U}{3L}\sum_{q_\parallel}\mathbf{S}_{-q_\parallel}\mathbf{S}_{q_\parallel} = \frac{2U}{3L}\sum_{q_\parallel}\mathbf{S}^{(\Psi)}_{-q_\parallel}\mathbf{S}^{(\Psi)}_{q_\parallel}\,. \tag{3.2}$$

Here it is useful to define both the conventional spin operator $\mathbf{S}_q = \sum_{k_\parallel} c^\dagger_{k_\parallel}\frac{\sigma}{2}c_{k_\parallel+q}$ and additionally the pseudo-spin operator of the Nambu basis $\mathbf{S}^{(\Psi)}_q = \sum_{k_\parallel}\Psi^\dagger_{k_\parallel}\frac{\tau}{2}\Psi_{k_\parallel+q}$.

In Fig. 3.1, we present a graphical representation of our model Hamiltonian. The interacting sites are marked in blue, solid red bonds depict normal hopping terms, and the dashed green lines visualize the d_{xy} pairing. Unless stated otherwise, we use t as the unit of energy set $(t,\mu,\Delta_{d_{xy}},L_\perp) = (1.0, 0.0, 1.0, 10^2)$. We study the effect of finite doping ($\mu \neq 0$) and our results do not crucially depend on $\Delta_{d_{xy}}$ and $L_\perp$ as long as the system is topological and $L_\perp$ is large enough to separate the exponentially-localized boundary modes of opposite edges.

3.2. Mean-field considerations

Let us examine some mean-field scenarios before presenting the numerical simulations. The most important step in this analysis is the projection of conventional approaches, such as $\mathbf{m} = \langle\mathbf{S}_0\rangle$ for ferromagnetic order, onto the edge modes as the relevant low-energy degrees of freedom. A detailed derivation of the boundary modes can be found in appendix A. Let us briefly summarize the main findings here, namely that topological flat-band states are created by

$$\gamma^\dagger_{k_\parallel} \;=\; \sum_{i_\perp=1}^{L_\perp}\phi_{k_\parallel}(i_\perp)\frac{1}{\sqrt{2}}(c^\dagger_{k_\parallel,i_\perp\uparrow} - i\,s_{k_\parallel}\,c_{-k_\parallel,i_\perp\downarrow})\,, \tag{3.3}$$

where $s_{k_\parallel} = \mathrm{sgn}(t\Delta_{d_{xy}}\sin(k_\parallel))$ labels the chirality and $\phi_{k_\parallel}(i_\perp)$ denotes the wave function of the boundary mode. Additionally, we found that the wave function can be chosen to by real valued and also that it is even in momentum $k_\parallel$.

In the following, we project the fermion operators onto the zero-energy boundary modes and use this projection to identify possible instabilities. We present the relation of different types of long-range order to the according Majorana mass terms which all break either time-reversal and/or translation symmetry. Interestingly, we find that each mass can be associated the a unique set of coherent combination of normal and superconducting order parameters, in contrast to previous mean-field studies that discussed only the leading order contribution.

3.2.1. Fermionic operators projected onto edge states

First, we decompose the fermion operators $\Psi_{k_\parallel,i_\perp} = (c_{k_\parallel,i_\perp;\uparrow}, c^\dagger_{-k_\parallel,i_\perp;\downarrow})$ in terms of the eigenstates $\eta_{k_\parallel,n}$ of the non-interacting system, using the unitary matrix U which diagonalizes H, with

$$\eta_{k_\parallel,n} = \sum_{i_\perp,\tau} U_{n,(i\perp,\tau)}(k_\parallel)\Psi_{k_\parallel,i_\perp;\tau} \tag{3.4a}$$

$$\Psi_{k_\parallel,i_\perp;\tau} = \sum_n U^\dagger_{(i\perp,\tau),n}(k_\parallel)\eta_{k_\parallel,n}\,. \tag{3.4b}$$

Second, we project onto the edge states by keeping only the zero-energy, exponentially localized modes with $E_n = 0$ given by $\eta_{k_\parallel,n} = \gamma_{k_\parallel}$, and ignore all other high energy contributions:

$$c_{k_\parallel,i_\perp,\uparrow} \rightarrow \frac{1}{\sqrt{2}}\phi_{k_\parallel}(i_\perp)\gamma_{k_\parallel} \tag{3.5a}$$

$$c_{k_\parallel,i_\perp,\downarrow} \rightarrow \frac{-is_{k_\parallel}}{\sqrt{2}}\phi_{k_\parallel}(i_\perp)\gamma^\dagger_{-k_\parallel} \tag{3.5b}$$

Finally, we combine Eq. (3.3) and Eq. (3.5) to generate the replacement rules of the projection onto chiral edge states

$$c_{k_\parallel,i_\perp,\uparrow} \rightarrow \frac{\phi^2_{k_\parallel}(i_\perp)}{2}\left(c_{k_\parallel,i_\perp,\uparrow} + is_{k_\parallel}c^\dagger_{-k_\parallel,i_\perp,\downarrow}\right) + \ldots \tag{3.6a}$$

$$c_{k_\parallel,i_\perp,\downarrow} \rightarrow \frac{\phi^2_{k_\parallel}(i_\perp)}{2}\left(c_{k_\parallel,i_\perp,\downarrow} - is_{k_\parallel}c^\dagger_{-k_\parallel,i_\perp,\uparrow}\right) + \ldots \quad . \tag{3.6b}$$

We are interested in the signatures along the edge, hence we will restrict the Monte Carlo observable to the edge sites. Therefore, we kept only the contributions along those position $i_\perp$ in the above. Additional terms due to the sum in Eq. (3.3) are represented by $(\ldots)$.

operator	definitions	operator	definitions
n_j	$c_j^\dagger \sigma^0 c_j$	$\Delta_j^{b,s}$	$c_j^{\mathrm{T}} i\tau_y \frac{\tau^0}{2} c_{j+1}$
$\mathbf{S}_j$	$c_j^\dagger \frac{\boldsymbol{\sigma}}{2} c_j$	Δ_j^{b}	$c_j^{\mathrm{T}} i\tau_y \frac{\boldsymbol{\tau}}{2} c_{j+1}$
J_j	$c_j^\dagger \frac{i\sigma^0}{2} c_{j+1} + h.c.$	Δ_j^{s}	$-c_{j\uparrow} c_{j\downarrow}$
n_j^b	$c_j^\dagger \frac{\sigma^0}{2} c_{j+1} + h.c.$		

Table 3.1.: List of various operators, both on-site and nearest-neighbors.

3.2.2. Repulsive interaction

In the presence of repulsive interactions one expects ferromagnetic instabilities, hence we approximate $\mathcal{H}_{\mathrm{int}}$ by a mean-field decoupling $\mathbf{m}\mathbf{S}_0$ with $\mathbf{m} = \langle \mathbf{S}_0 \rangle$. Due to the $SU(2)$-spin symmetry of the Hamiltonian, the orientation $\mathbf{m}$ remains arbitrary. A nonzero value $|\mathbf{m}|$ breaks both time-reversal and spin-rotation symmetry.

Using the projection rules derived above by substituting Eq. (3.5) into the definition of the physical spin operator, we obtain the Majorana mass term

$$\mathcal{H}_{\text{rep. MF}} = \mathbf{m}\mathbf{S}_0 = \frac{1}{2} \sum_{k_\parallel=0}^{\pi} \Gamma_{k_\parallel}^\dagger \mathbf{m}_{k_\parallel} \tau \Gamma_{k_\parallel} + \cdots , \tag{3.7}$$

with the basis $\Gamma_{k_\parallel}^\dagger = (\gamma_{k_\parallel}^\dagger, -i s_{k_\parallel} \gamma_{-k_\parallel})$ and $\mathbf{m}_{k_\parallel} = \phi_{k_\parallel}^2(i_\perp,0)\,\mathbf{m}$. The $(\cdots)$ represent edge-bulk and bulk-bulk contributions.

To make the connection with the QMC simulations, we express Eq. (3.7) in terms of fermionic correlations along the edge, or equivalently, we apply the replacement rules of Eq. (3.6) to the physical spin operator $\mathbf{S}_0$. This generates an expression with the forth power of the wave function, $\phi_{k_\parallel}^4(i_\perp)$ and $s_{k_\parallel}\phi_{k_\parallel}^4(i_\perp)$. As the wave function is even in $k_\parallel$ while the chirality $s_{k_\parallel}$ inherits the sign of $k_\parallel$, the former is also even and latter odd in momentum. Accordingly, we can expand $\phi_{k_\parallel}^4(i_\perp)/2 = a_0 + \ldots$ and $s_{k_\parallel}\phi_{k_\parallel}^4(i_\perp)/2 = 2b_1 \sin(k_{k_\parallel}) + \ldots$ in terms of harmonic functions. We find the following decompositions

$$S_0^x = \sum_j \left[a_0 S_j^x + b_1 (\Delta_j^{b,x} + \Delta_j^{b,x\dagger}) \right] + \ldots \tag{3.8a}$$

$$S_0^y = \sum_j \left[a_0 S_j^y + b_1 (\Delta_j^{b,y} + \Delta_j^{b,y\dagger}) \right] + \ldots \tag{3.8b}$$

$$S_0^z = \sum_j \left[a_0 S_j^z - b_1 (\Delta_j^{b,z} + \Delta_j^{b,z\dagger}) \right] + \ldots . \tag{3.8c}$$

The fermion operators on the right hand side are defined in Tab. 3.1.

Due to the chiral structure of the edge states, a non-zero mass $|\mathbf{m}|$ corresponds to a coherent superposition of FM and spin-triplet SC, where the in-plane (out-of-plane) components

are parallel (antiparallel) aligned. The decomposition of the $k_\parallel$ dependence of $\phi^4_{k_\parallel}$ in harmonics induces further contributions on next-nearest neighbor and higher-order bonds, that oscillate between normal and SC operators.

This analysis demonstrates the level at which normal and SC order are intertwined. If the edge supports another state with the same wave function $\phi_{k_\parallel}(i_\perp)$ of opposite chirality, the anomalous contribution $c^\dagger$ in Eq. (3.6) cancels and the only consequence of the projection is a prefactor of $\phi^2_{k_\parallel}(i_\perp)$. Hence, a conventional SC ground state may also dynamically mix normal and SC order parameter, but the linear superposition here stems from the chiral nature of the Majorana modes.

The above derivation assumed half filling, such that the SC nodes are located in the edge Brillouin zone at 0 and π. The analysis itself however does not crucially depend on this assumption. Doping the system away from half filling shortens the flat band and the summation in Eq. (3.7) has to be adapted accordingly. Nevertheless, the edge states still come in $(k_\parallel, -k_\parallel)$ pairs and there is again a mixing of normal and SC operators. The only point that requires more work is the decomposition in harmonic functions and the Fourier transformation that lead to the equations above.

This reproduces the edge splitting terms known from Ref. [45].

3.2.3. Attractive interactions

As indicated by Eq. (3.2), the transformation $c_\mathbf{k} \to \Psi_\mathbf{k}$ renders $U > 0$ repulsive in terms of $\mathbf{S}^{(\Psi)}_q$. Hence, we expect pseudo-magnetic instabilities. First focusing on homogeneous instabilities ($q_\text{inst} = 0$), we find that $\mathbf{S}^{(\Psi)}_0$ projected on the Majorana states is vanishing except for the y component. Therefore only a condensation of $S^{y,(\Psi)}_0$ gaps the edge spectrum. Including inhomogeneous order (i.e., $q_\text{inst} \neq 0$) opens additional channels. It is natural to study those wave vectors q_inst that maximize the nesting between edge states with opposite chiral eigenvalue. At half filling, this fixes $q_\text{inst} = \pi$ and projecting $\mathbf{S}^{(\Psi)}_\pi$ on the Majorana states generates nontrivial operators for the x and z but a vanishing y component, complementary to $q_\text{inst} = 0$.

In the following calculations, we use the particle-hole-symmetry at half filling explicitly that guarantees the relation $\phi_{k_\parallel}(i_\perp) = -(-1)^{i_\perp}\phi_{k_\parallel+\pi}(i_\perp)$. As the interaction is restrained to $i_\perp = 1$ and the QMC study is performed in this layer only, we drop the sign completely. The projection of $\mathbf{S}^{(\Psi)}_q$ onto the edge states vanishes for the x- and z-component with $q = 0$ and for the y-component with $q = \pi$. The three non-vanishing parts $(S^{x,(\Psi)}_\pi, S^{y,(\Psi)}_0, S^{z,(\Psi)}_\pi)^T$ generate the Majorana mass terms with $\tilde{\Gamma}^\dagger_{k_\parallel} = (\gamma^\dagger_{k_\parallel}, -is_{k_\parallel}\gamma^\dagger_{k_\parallel-\pi})$

$$\mathcal{H}_\text{attr. MF} = \mathbf{g}(S^{x,(\Psi)}_\pi, S^{y,(\Psi)}_0, S^{z,(\Psi)}_\pi)^T = \frac{1}{2}\sum_{k_\parallel=0}^{\pi} \tilde{\Gamma}^\dagger_{k_\parallel}\left(g^x_{k_\parallel}\tau^x + \tilde{\mathbf{g}}_{k_\parallel}\tau\right)\tilde{\Gamma}_{k_\parallel} + \cdots, \tag{3.9}$$

with the order parameter $g^x_{k_\parallel} = \phi^2_{k_\parallel}(i_{\perp,0})g^x$ and $\tilde{\mathbf{g}}_{k_\parallel} = \phi^2_{k_\parallel}(i_{\perp,0})\mathbf{g}\times\mathbf{e_x}$.

At half filling, we make use of a sublattice symmetry $U^{\mathrm{SL}} = \sum_{k_\parallel, i_\perp} (-1)^{i_\perp} \Psi^\dagger_{k_\parallel, i_\perp} \frac{\tau^x}{2} \Psi_{k_\parallel + \pi, i_\perp}$. This symmetry generates rotations in the (y,z) plane that change the orientation of $\tilde{\mathbf{g}}$, but leave $|\tilde{\mathbf{g}}|$ and g_x invariant. Hence, there is a competition between these two channels. Interestingly, the sublattice symmetry combines a time-reversal and a translation-symmetry-breaking sector in $\tilde{\mathbf{g}}$.

As before, we rewrite Eq. (3.9) in terms of fermionic operators by substituting Eq. (3.6) into the definition of $\mathbf{S}^{(\Psi)}_q$:

$$S^{x(\Psi)}_\pi = \sum_j (-1)^j \left[a_0 (\Delta^s_j + \Delta^{s\dagger}_j) + b_1 n^b_j \right] + \dots \tag{3.10a}$$

$$S^{y(\Psi)}_0 = \sum_j \left[-i a_0 (\Delta^s_j - \Delta^{s\dagger}_j) + b_1 J_j \right] + \dots \tag{3.10b}$$

$$S^{z(\Psi)}_\pi = \sum_j (-1)^j \left[a_0 n_j - b_1 (\Delta^{b,s}_j + \Delta^{b,s\dagger}_j) \right] + \dots \tag{3.10c}$$

We obtain once more linear superpositions of normal and SC operators. $S^{x,(\psi)}_\pi$ combines finite-momentum s-wave pairing with a bond-density-wave instability, $S^{y,(\psi)}_0$ contains complex s-wave SC and edge current operators, and $S^{z,(\psi)}_\pi$ includes a CDW instability and finite-momentum singlet SC on nearest-neighbor bonds.

Doping the system breaks the symmetry U^{SL}. As a result, the constraint on $S^{y,(\psi)}$ and $S^{z,(\psi)}$ is lifted, which allows for a competition between both channels. As the bulk nodes move away from 0 or π, the nesting wave vector q_{inst} decreases and we expect instabilities in the $S^{x,(\psi)}$ and $S^{z,(\psi)}$ channel at $q_{\mathrm{inst}} < \pi$.

As we have shown above, the projection onto the edge modes is able to identify the relevant order parameters, the associated Majorana mass terms and the according fermion correlation functions. The results are summarized for both repulsive (upper two rows) as well as attractive interactions (lower three rows) in Tab. 3.2.

3.3. Method

We have argued before, that the high density of states at the Fermi level combined with the reduced dimensionality of the edge modes requires a proper treatment of the fluctuations around mean-field saddle points. Therefore, we study this model using the numerically exact continuous-time quantum Monte Carlo method introduced in Sec. 2.2. Usually, the non-interacting part of models studied by QMC approaches does not include superconductivity. However, it has been show that the algorithm can also be formulated in the Nambu-Basis Ψ in case of s-wave singlet pairing [120, 161, 162]. This setup employs the conventional spin rotation symmetry S_z of the original fermions that generates a global $U(1)$ charge con-

non-zero vev	mass term	fermionic correlation along interacting edge
$\left\langle S_0^{x,y}\right\rangle$	$\frac{1}{2}\sum_{k_\parallel=0}^{\pi}\Gamma_{k_\parallel}^\dagger m_{k_\parallel}^{x,y}\tau^{x,y}\Gamma_{k_\parallel}$	$\sum_j\left[a_0 S_j^{x,y}+b_1(\Delta_j^{b;x,y}+\Delta_j^{b;x,y^\dagger})\right]+\cdots$
$\left\langle S_0^{z}\right\rangle$	$\frac{1}{2}\sum_{k_\parallel=0}^{\pi}\Gamma_{k_\parallel}^\dagger m_{k_\parallel}^{z}\tau^{z}\Gamma_{k_\parallel}$	$\sum_j\left[a_0 S_j^{z}-b_1(\Delta_j^{b,z}+\Delta_j^{b,z^\dagger})\right]+\cdots$
$\left\langle S_\pi^{x(\Psi)}\right\rangle$	$\frac{1}{2}\sum_{k_\parallel=0}^{\pi}\tilde{\Gamma}_{k_\parallel}^\dagger g_{k_\parallel}^{x}\tau^{x}\tilde{\Gamma}_{k_\parallel}$	$\sum_j(-1)^j\left[a_0(\Delta_j^{s}+\Delta_j^{s\dagger})+b_1 n_j^b\right]+\cdots$
$\left\langle S_0^{y(\Psi)}\right\rangle$	$\frac{1}{2}\sum_{k_\parallel=0}^{\pi}\tilde{\Gamma}_{k_\parallel}^\dagger(-g_{k_\parallel}^{y})\tau^{z}\tilde{\Gamma}_{k_\parallel}$	$\sum_j\left[-ia_0(\Delta_j^{s}-\Delta_j^{s\dagger})+b_1 J_j\right]+\cdots$
$\left\langle S_\pi^{z(\Psi)}\right\rangle$	$\frac{1}{2}\sum_{k_\parallel=0}^{\pi}\tilde{\Gamma}_{k_\parallel}^\dagger g_{k_\parallel}^{z}\tau^{y}\tilde{\Gamma}_{k_\parallel}$	$\sum_j(-1)^j\left[a_0 n_j-b_1(\Delta_j^{b,s}+\Delta_j^{b,s^\dagger})\right]+\cdots$

Table 3.2.: Summary of all possible MF channels at half filling. The left table lists possible vacuum expectation values (vev), their associated masses for the edge states, and the characterizing fermionic correlations. We use $\Gamma_{k_\parallel}^\dagger=(\gamma_{k_\parallel}^\dagger,-is_{k_\parallel}\gamma_{-k_\parallel})$ and $\tilde{\Gamma}_{k_\parallel}^\dagger=(\gamma_{k_\parallel}^\dagger,-is_{k_\parallel}\gamma_{k_\parallel-\pi}^\dagger)$. The $(\cdots)$ indicate additional operators on higher-order bonds.

servation in Nambu space. Consequently, the are no anomalous Green's functions $\langle\Psi_{\mathbf{i}}\Psi_{\mathbf{j}}\rangle$ and $\langle\Psi_{\mathbf{i}}^\dagger\Psi_{\mathbf{j}}^\dagger\rangle$. Hence, Wick's theorem generates a single determinate for the weight of the configuration.

To make the connection with Sec. 2.2, let us express the grand-canonical partition sum using the action S with a Gaussian part S_0 and an interacting contribution S_{int}

$$S_0 = -\sum_{\mathbf{i},\mathbf{j}}\int_0^\beta\!\!\int d\tau\, d\tau'\Psi_{\mathbf{i},\tau}^\dagger G_0^{-1}(\mathbf{i}-\mathbf{j},\tau-\tau')\Psi_{\mathbf{j},\tau'} \tag{3.11}$$

$$S_{\text{int}} = -U\sum_{i_e}\int_0^\beta d\tau\prod_\sigma(\Psi_{\sigma,i_e,\tau}^\dagger\Psi_{\sigma,i_e,\tau}-\frac{1}{2}), \tag{3.12}$$

where $G_0^{-1}(\mathbf{i}-\mathbf{j},\tau-\tau')$ is the free BdG-Green's function of the two-dimensional system Eq. (3.1) in ribbon geometry. The configuration space, sampled stochastically, is given by the set of n vertices $v(x_j,\tau_j)=\prod_{\sigma=\uparrow,\downarrow}[\Psi_{\sigma,x_j,\tau_j}^\dagger\Psi_{\sigma,x_j,\tau_j}-1/2]$ where x_j is restricted to positions along the edge as only those sites are interacting.

When we evaluate the weight of a configuration, $w(C_n)=\frac{U^n}{n!}\langle\prod_{j=1}^n v_j\rangle_0$, we can make use of Wick's theorem that will exclusively evoke propagators between two edge sites. It is also straight forward to show that the average expansion order $\langle n\rangle=-\beta\langle H_{\text{int}}\rangle$ is proportional to the potential energy. This is an extensive quantity which scales linear with the number of interacting edge sites. Accordingly, the simulation appears to be one-dimensional. Nevertheless the Green's function still contains the information about all possible paths in the original two-dimensional system and thereby respects all degrees of freedom including bulk states [32, 163, 164]. In precisely this sense, we have integrated out the bulk degrees of freedom.

At half filling ($\mu = 0$) the absence of the negative-sign problem for attractive interactions ($U < 0$) is guarantied by the symmetry of the Hamiltonian with respect to the transformation $\Psi_{\mathbf{i},\sigma} \to D_{\mathbf{i},\sigma}\Psi^\dagger_{\mathbf{i},\sigma}$ where the diagonal matrix $D_{\mathbf{i},\sigma} = \sigma(-1)^{i_x+i_y}$. This particle-hole symmetry enforces the single particle Green's function $G^{(\Psi)}_{(\mathbf{i},\sigma),(\mathbf{j},\sigma')}(\tau) = \langle \Psi^\dagger_{\mathbf{i},\sigma}(\tau)\Psi_{\mathbf{j},\sigma'}(0)\rangle_0$ to respect the relation

$$G^{(\Psi)}_{(\mathbf{i},\sigma),(\mathbf{j},\sigma')}(\tau) \;=\; -D_{\mathbf{j},\sigma'}G^{(\Psi)}_{(\mathbf{j},\sigma'),(\mathbf{i},\sigma)}(-\tau)D_{\mathbf{i},\sigma}\,, \tag{3.13}$$

where the overall negative sign originates from the usual anti-periodic boundary conditions in imaginary time for fermions. Using Wick's theorem, the weight of a configuration is given as $w(C_n) = \frac{U^n}{n!}\det[M]$ with the $2n \times 2n$-matrix $M_{q,q'} = G^{(\Psi)}_{(\mathbf{i}_q,\sigma_q),(\mathbf{i}_{q'},\sigma_{q'})}(\tau_q - \tau_{q'}) - 1/2\delta_{qq'}$. Here, odd values of q refer to the $\sigma = \uparrow$ and the even ones to the $\downarrow$ factor of Eq. (3.12).

Due to the PHS, the diagonal elements vanish and the off-diagonal entries are related through Eq. (3.13) such that $M^{\mathrm{T}} = -DMD$. Observe that $\det[D] = (-1)^n$ as each vertex contains one site of the even and odd sublattice. For attractive interaction ($U < 0$), we have $U^n = (-U)^n(-1)^n$ with $(-U)^n > 0$. Hence, the weight can be rewritten as $w(C_n) = \frac{(-U)^n}{n!}\det[DM] \geq 0$ where crucially DM is a real[1], anti-symmetric matrix with positive determinate. Observe that repulsive interaction introduce a trivial sign-problem as $(-U)^n$ is not positive ($U > 0$) that cannot be cured by introducing the auxiliary spins as discussed in Sec. 2.2. These spins violate the particle-hole symmetry for an individual configuration such that the sign of the determinant is not controllable anymore. This has first been understood by Huffman and Chandrasekharan in Ref. [165].

Finally, let us briefly mention the main observables here, a more detailed discussion is presented in Sec. 2.4. The single-particle spectra $A_{\mathrm{tot}}(\omega,k) = -(2\pi)^{-1}\sum_\sigma \mathrm{Im}G_\sigma(\omega,k)$ are extracted from the time-ordered Green's function $\langle c^\dagger_{k,\sigma}(\tau)c_{k,\sigma}(0)\rangle$ using the stochastic maximum entropy method [139, 140]. To identify the mentioned Majorana mass terms, we determine equal-time correlation functions of the according fermion operators $\mathcal{A}$ and $\mathcal{B}$,

$$C_{\mathcal{A},\mathcal{B}}(q) = \frac{1}{L}\sum_{n,n'}^{L} e^{iq(n-n')}\left(\langle \mathcal{A}^\dagger_n\mathcal{B}_{n'}\rangle - \langle \mathcal{A}^\dagger_n\rangle\langle \mathcal{B}_{n'}\rangle\right). \tag{3.14}$$

3.4. Results

The QMC simulation is sign-problem free for attractive interactions ($U = -2$) at half filling such that we can perform a scaling analysis and extrapolate to the thermodynamic limit. Doping and/or repulsive interaction introduce a sign problem such that the required computation time diverges exponentially with system size. Hence, we cannot approach the thermody-

[1] In position space, every matrix element of the non-interacting Hamiltonian is real valued and therefore the Green's function is also real.

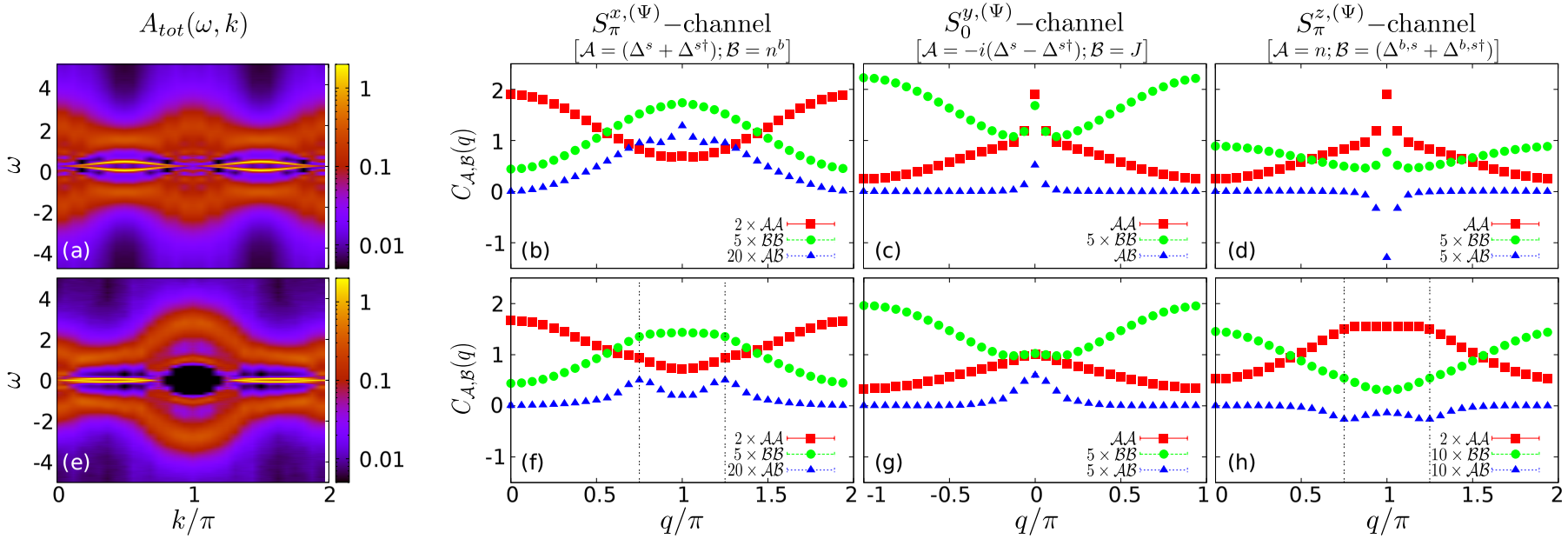

Figure 3.2.: We present the single particle spectrum $A_{\text{tot}}(\omega,k)$ and equal-time correlation functions for attractive interactions with $L=32$ and $(U,\mu,\beta/t)=(-2,0,100)$ in the top [(a)–(d)] and $(U,\mu,\beta/t)=(-1,-0.586,50)$ in the bottom [(e)–(h)]. The edge states have been gapped out and instabilities can be identified in all three $\mathbf{S}^{(\Psi)}$ channels as defined in Tab. 3.2.

namic limit anymore and therefore only extract leading instabilities with fixed $L = 32$ and $U = \pm 1$.

Attractive interactions: We first study the system at half filling and set the inverse temperature to $\beta/t = 100$. The single particle spectrum is shown in Fig. 3.2(a) and we observe that the zero-energy flat bands develop a dispersion and gap out. Hence the interaction along the edge dynamically generates Majorana masses and many of the mass terms discussed above can generate such a edge spectrum. However, each channel leads to an unique set of coherent fermionic correlations that may be seen as its fingerprint. In Figs. 3.2(b)–(d) we present the correlation function for the associated operators according to Tab. 3.1. The data suggests instabilities for both $|g^x| \neq 0$ ($S_\pi^{x(\Psi)}$-channel) and $|\tilde{\mathbf{g}}| \neq 0$ ($S_0^{y(\Psi)}$- and $S_\pi^{z(\Psi)}$-channel), apparent from the non-analytic behavior at $q = 0$ or $q = \pi$, respectively. Each nontrivial cross correlation confirms the expected coherent superposition of normal and SC correlations, including the phase relation between the particle-hole and particle-particle contribution.

Without suffering from the negative-sign problem, we can systematically increase the system size while keeping a fixed ratio $\beta/L = 50/8$. Figure 4.3 visualizes the scaling behavior of the correlation function for the CDW, representing the $\tilde{\mathbf{g}}$ channel, and for s-wave singlet SC, representing the g^x-channel. The extrapolation of the data suggests long-range order at $T = 0$ in the $\tilde{\mathbf{g}}$ channel, whereas g^x vanishes. Observe that we employed the enhanced symmetry of the zero-energy subspace (i.e., the chiral nature of the edge states) to derive the fermionic correlation functions associated to each Majorana mass. However, this symmetry does not manifest itself for the order parameter as it would unify the three channels by promoting the $U(1)$ sublattice symmetry to a $SU(2)$ symmetry. This can be seen as one instance where the bulk states that are ignored in the mean-field analysis, contribute in the full system.

Doping the system breaks the sublattice symmetry and allows a competition between the $S_0^{y(\Psi)}$- and $S_{q_{\text{inst}}}^{z(\Psi)}$-channels. Figure 4.2(e) depicts the single particle spectrum and we again observe a splitting of the flat-band. Due to the negative-sign problem, the interaction strength is reduced which explains the smaller Majorana mass compared to the system at half filling. Once more the correlation function in Figs. 3.2(f)–(h) show instabilities in all channels, visible as non-analytic behavior, which is best seen in the cross correlations between normal and

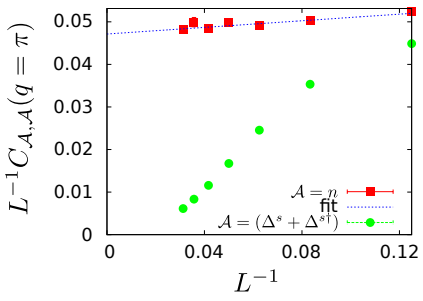

Figure 3.3.: Finite size scaling of $|\tilde{\mathbf{g}}|^2$ and $|g^x|^2$ with fixed $\beta = \frac{50}{8}L$ in red squares and green discs, respectively. The extrapolation for $\mathcal{A} = n$ suggests long-range order ($|\tilde{\mathbf{g}}| \neq 0$) at $T = 0$.

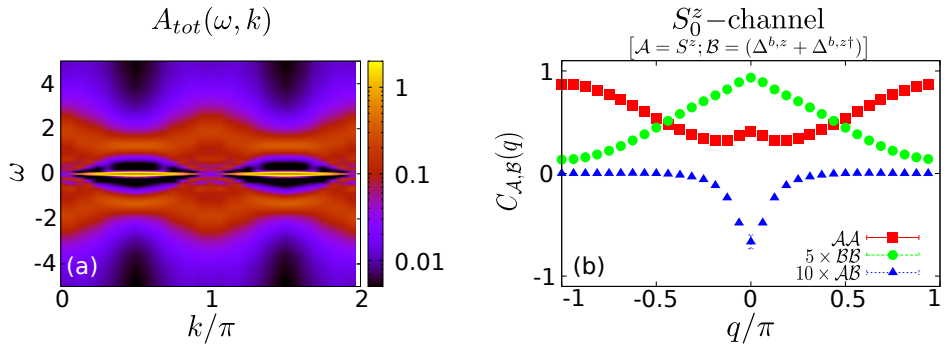

Figure 3.4.: We present the single particle spectrum $A_{\text{tot}}(\omega,k)$ (a) and the correlation functions (b) for $L=32$ and $\beta/t=100$. The edge states have been gapped out and the FM is coherently mixed with triplet SC.

SC contributions. The doping of $\mu=-0.586$ induces a nesting vector $q_{\text{inst}}=\pm\frac{3}{4}\pi$, which explains the instabilities for these momenta in the $S^{x(\Psi)}$ and $S^{z(\Psi)}$ channel. Even though the extrapolation to the ground state of the thermodynamic limit is even more interesting then before, it is prohibited by the numerical effort that increases exponentially with the euclidean space-time βL. However, we can speculate that the $S_0^{y(\Psi)}$-channel might be favorable as it does not depend on the nesting vector q_{inst} but rather introduces a mass gap by scattering edge states with $\pm k_{\|}$ into each other.

Repulsive interactions: Here, the system is again at half filling and the results for $L=32$ and $\beta=100$ are shown in Fig. 3.4. The spectral function is depicted in panel (a) for the whole edge Brillouin zone. The Majorana states are again dispersive and develop a gap everywhere except for the bulk node projections at $k_{\|}=0$ or $k_{\|}=\pi$. Due to the weaker interaction strength compared to the attractive case, the Majorana mass is reduced. We can nevertheless confirm that edge ferromagnetism is the leading instability as it has been discussed on the mean-field level in Ref. [45] and Sec. 3.2. In contrast to previous studies, however, we find in our analysis that the ferromagnet is coherently mixed with a (anti-)parallel polarized triplet SC. This is well confirmed by the correlation functions depicted in Fig. 3.4(b).

3.5. Discussion

Previous studies discussed ferromagnetism or additional *is*-wave pairing as leading instabilities of the boundary modes on a mean-field level [40–45]. In contrast to those works, we show that one should view the possible instabilities from the perspective of Majorana mass terms. The most important consequence is the linear superposition of particle-hole and particle-particle channels. For example, the ferromagnetic order is coherently mixed with triplet superconductivity, similarly *is*-wave pairing is combined with spontaneous current

order. The former is relevant for repulsive interaction and the latter for attractive ones.

We find a remarkable agreement between the mean-field analysis and the numerically exact results of the quantum Monte Carlo simulations. To appreciate this, it is important to realize the somewhat crude approximation made during the derivation. We have completely ignored any bulk-state contributions, even though there is no energy gap separating the nodal bulk from the zero-energy boundary states. Related to this, higher order contribution may lead to processes that flip between states of different chiralities [27].

The coherence between the various order parameter is a directly tied to the chiral nature of the Majorana flat-bands along the edge. Hence, probing the phase relation can provide useful insights into the edge-state character. Interestingly, we may be able to test this in experiments. Let us focus on the case of repulsive interaction which is the most likely scenario for underdoped YBCO cuprates. We propose to build SC-FM-SC Josephson junctions [166] and control the polarization of the triplet component using the orientation of the ferromagnet in the middle of the junction, e.g., by weak external fields. We expect the ferromagnetic order along the edge to be aligned with the magnet of the junction. Observe that this setup allows a switch between parallel and anti-parallel polarized triplet components which should leave non-trivial signatures in the Josephson current. Also one can compare junctions with interfaces in the (110) direction (with topological Majorana modes) and the (100) version (without edge mode) in order to control the background to the measured signal.[2] Finally, in case of attractive interactions, it might be possible to detect the CDW order using STM experiments, once the order is pinned by impurities or the underlying lattice [167].

One interesting avenue for future investigations are topological non-centrosymmetric superconductors. Here, inversion symmetry is broken by the lattice such that Rashba spin-orbit coupling as well as the mixing of singlet and triplet components in the pairing amplitude should be included. As a result, one can define systems with half of the degrees of freedom along the edge, e.g., one could design a system where the flat band only exists for $k_{\|} > 0$. This renders the flat band more stable as all mass terms of this work connect modes at $k_{\|} > 0$ and $k_{\|} < 0$ of opposite chirality. However, it is still at odds with the laws of thermodynamics.

[2] We thank P. Brouwer for very useful discussions especially for pointing out some ideas that led to the proposed experimental setup.

CHAPTER 4

Spontaneous particle-hole symmetry breaking of correlated fermions on the Lieb lattice

It is widely accepted that fermionic quantum Monte Carlo methods may only be applied to certain models – unless one is willing to give up the polynomial scaling of the numerical expense and suffer the infamous negative-sign problem. In the previous chapter, we had to experience the numerical limits set by the negative-sign problem first hand. In its absence, we were able to extrapolate to the thermodynamic limit, in its presence, this was numerically to expensive. The origin of the negative-sign problem can vary from method to method. In the auxiliary-field QMC [110], the polynomial scaling is usually ensured by a symmetry of the action after the Hubbard-Stratonovich decomposition which may be explicit in the representation of complex [168] or Majorana [169–171] fermions. A popular class of solvable models respect a particle-hole symmetry (PHS) – restricting the system to half filling – and contain repulsive interaction on non-frustrated lattices [172]. Here, we gain insights into properties away from half-filling from simulations that preserve PHS. However, the symmetry will be spontaneously broken by a variant of charge order that simultaneously induces a finite chemical potential.

We study fermions on the Lieb lattice that is a square lattice with additional sites in the center of the original bonds, also know as a face-centered square lattice. This structure is sometimes used to model the CuO planes of cuprates in order to understand high temperature superconductivity. Here, we instead focus on fundamental properties of two linear dispersing modes and a flat band that is induced by perfect destructive interference of the three orbital unit cell. In case of spinful fermions with $SU(2)$ symmetry, the system is prone to ferromagnetic order [173]. In contrast, the ground state for spinless fermions is either unique or doubly degenerate [174]. Generically, correlation effects play an important role

whenever there is a high density of states at the Fermi level, here it is even diverging linearly with the system size. Previous works already studied the robustness of the flat band with respect to magnetic fields [175], spin-orbit interactions [175–177], local [178–181] and inter-site [182, 183] Coulomb repulsion, attractive interactions [184, 185], as well as disorder [186]. The interested reader is referred to the more complete review on strongly-correlated flat-band systems in Ref. [187]. The Lieb lattice geometry has been constructed in optical lattices [188, 189] and populating them with spin-polarized fermionic atoms would experimentally realize the scenario presented here.

The low-energy band structure of this model represents a spin-1 Dirac cone for which the charge order is just one out of many possible symmetry breaking terms. Another option is the spontaneous generation of current order. This band gap induces a topologically non-trivial band structure with the according chiral edge modes, once open boundary conditions are introduced. Hence, the long-range current-order scenario would represent a spontaneously generated quantum anomalous Hall (QAH) state. For spinful fermions, the first dynamic realization of a quantum spin Hall (QSH) phase is established in Ref. [48] where a deconfined quantum critical point between the QSH and a superconducting states demonstrates the interesting physics present in such systems. Here, such a current order is not found.

We employ continuous-time QMC (Sec. 2.2), auxiliary-field QMC (Sec. 2.3) and exact diagonalization techniques in order to study spinless fermions on the Lieb lattice with repulsive nearest-neighbor interactions. Both QMC methods rely on the PHS at half-filling to avoid the negative-sign problem and conserve the number of particles. Breaking the PHS with charge order relates to an Ising order and may already occur at finite temperature [190, 191]. In those studies, charge ordering does not induce finite doping which is the conventional scenario. Here, the situation is fundamentally different due to fractional filling related to sublattices of unequal size. In fact, the symmetry breaking charge-density-wave (CDW) states correspond to filling fractions of 1/3 or 2/3, depending on the sign of the Ising order parameter. The QMC algorithms are formulated in a configuration space where each elements preserves the PHS such that the negative sign problem is avoided. Hence, the simulation is forced to 'see' both CDW states with equal weight. Nevertheless, we show the possibility to infer the properties the symmetry broken states and thereby gain access to systems away from half-filling.

This work was done in collaboration with M. Bercx[1] and T. C. Lang under the guiding supervision of F. F. Assaad. The corresponding publication of this project is Ref. [P4] and the following contains reprinted figures with permission from Ref. [P4]. Copyright (2017) by the American Physical Society.

[1]Both Martin Bercx and I contributed equally during this project. Martin developed the Majorana QMC implementation and I performed the CT-INT and exact diagonalization calculations.

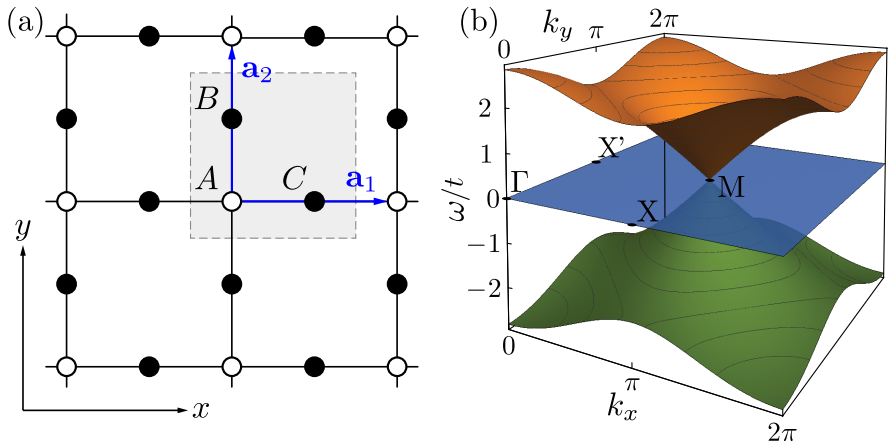

Figure 4.1.: The bipartite lattice structure of the Lieb lattice (a) with the three orbitals A, B and C per unit cell indicated in gray and the dispersion of the non-interacting system (b) which features a single linearly dispersing cone at the corner of the Brillouin zone.

4.1. Model & Symmetries

We study spinless fermions on a two-dimensional Lieb lattice [cf. Fig. 4.1(a)] interacting via a nearest-neighbor Coulomb repulsion described by $\mathcal{H}_0 + \mathcal{H}_V$, with

$$\mathcal{H}_0 = -t \sum_{\langle \mathbf{i},\mathbf{j} \rangle} (c_\mathbf{i}^\dagger c_\mathbf{j} + \text{H.c.}) \,, \tag{4.1}$$

$$\mathcal{H}_V = V \sum_{\langle \mathbf{i},\mathbf{j} \rangle} \left(n_\mathbf{i} - \frac{1}{2} \right) \left(n_\mathbf{j} - \frac{1}{2} \right) \tag{4.2}$$

$$= -\frac{V}{2} \sum_{\langle \mathbf{i},\mathbf{j} \rangle} \left[\left(c_\mathbf{i}^\dagger c_\mathbf{j} + \text{H.c.} \right)^2 - \frac{1}{2} \right] \,, \tag{4.3}$$

where $c_\mathbf{i}^\dagger$ creates a spinless electron on lattice site $\mathbf{i}$, t denotes the hopping amplitude and V the interaction strength. The Fourier transformation of the non-interacting Hamiltonian to momentum space generates $\mathcal{H}_0 = \sum_\mathbf{k} \Psi_\mathbf{k}^\dagger H(\mathbf{k}) \Psi_\mathbf{k}$ with $\Psi_\mathbf{k}^\dagger = \left(c_{A\mathbf{k}}^\dagger, c_{B\mathbf{k}}^\dagger, c_{C\mathbf{k}}^\dagger \right)$ and expanding it to leading order around the $\mathbf{M}$-point at (π, π) gives

$$H(\mathbf{M} + \mathbf{q}) = -t(q_x \mathbf{S}_x + q_y \mathbf{S}_y) + \mathcal{O}(q^2) \,. \tag{4.4}$$

Here the $\mathbf{S}$ matrices are the spin $S = 1$ representation of the SU(2) Lie-Algebra [175, 192, 193]. The eigenvalues are given by $\{0, \pm|\mathbf{q}|\}$ such that the Hamiltonian hosts a zero energy flat band and two linear dispersing modes as it is typical for a spin-1-cone [192]. The spectrum for the whole Brillouin zone is depicted in Fig. 4.1(b).

The zero mode is not a coincidence but it is rather strongly tied to the symmetry of the Hamiltonian with respect to the transformation $c_\mathbf{i}^\dagger \to s_\mathbf{i} c_\mathbf{i}$. The sign $s_\mathbf{i}$ partitions the Lieb

lattice into an odd (even) sublattice with $s_{\mathbf{i}} = -1$ ($s_{\mathbf{i}} = +1$) when the site $\mathbf{i}$ is in sublattice A (B or C). Clearly, the even part is twice as large as the odd one. This constitutes the property which is causing the later discussed charge order to also induce a finite doping driving the system away from half filling. To further discuss the symmetries of the model, let us introduce the Majorana basis

$$c_{\mathbf{i}} = \frac{1}{2\sqrt{s_{\mathbf{i}}}}(\gamma_{\mathbf{i}} + \mathrm{i}\eta_{\mathbf{i}}) \,, \quad c_{\mathbf{i}}^{\dagger} = \frac{\sqrt{s_{\mathbf{i}}}}{2}(\gamma_{\mathbf{i}} - \mathrm{i}\eta_{\mathbf{i}}) \,. \tag{4.5}$$

The fermion commutation relation, $\{c_{\mathbf{i}}, c_{\mathbf{j}}^{\dagger}\} = \delta_{\mathbf{ij}}$, fixes the Majorana commutation relations to $\{\gamma_{\mathbf{i}}, \gamma_{\mathbf{j}}\} = \{\eta_{\mathbf{i}}, \eta_{\mathbf{j}}\} = 2\delta_{\mathbf{ij}}$ and $\{\gamma_{\mathbf{i}}, \eta_{\mathbf{j}}\} = 0$. Rewriting the hopping operator for bond $\langle \mathbf{i}, \mathbf{j} \rangle$ in terms of the new basis results in

$$c_{\mathbf{i}}^{\dagger} c_{\mathbf{j}} + c_{\mathbf{j}}^{\dagger} c_{\mathbf{i}} = \frac{\mathrm{i}}{2}(\gamma_{\mathbf{i}}\gamma_{\mathbf{j}} + \eta_{\mathbf{i}}\eta_{\mathbf{j}}) \,. \tag{4.6}$$

Observe that this form explicitly demonstrates an underlying $O(2)$ symmetry which contains both the $U(1) \simeq SO(2)$ charge conservation of Eq. (4.1) as well as the PHS symmetry of bipartite lattices that allowed the different phase choice for the sublattices in Eq. (4.5). The latter is represented by the reflection operation $\mathbf{R} = \sigma_z$ and completes the $O(2)$ group. It is also interesting to observe that the hopping amplitude t being real induces an anti-unitary time-reversal symmetry $\gamma_{\mathbf{j}} \leftrightarrow s_{\mathbf{j}}\eta_{\mathbf{j}}$, which will be used to show the absence of the negative-sign problem for the BSS algorithm in the following section.

4.2. QMC methods

The interacting fermion model defined in Eqs. (4.1)–(4.3) can be solved by multiple quantum Monte Carlo variants, without formally encountering a sign problem. We will employ the continuous time QMC within the interaction expansion (CT-INT) [109, 119] (see Sec. 2.2) as well as an auxiliary field algorithm (AF-QMC) [110, 121] in the Majorana representation with slight modifications compared to Sec. 2.3. Both methods are briefly discussed in the following, mainly focusing on the absence of the negative-sign problem, before we compare the two QMC methods. We find that the CT-INT algorithm heavily suffers from fat tail distributions (see Sec. 2.1.2) for the order parameter such that we rely on the AF-QMC to investigate the phase transition. This section is closed with a discussion of the potentially optimal method of choice, the continuous-time auxiliary field approach, which generically interpolates between the other two flavors. However, we show that this does not hold in this model.

4.2.1. Continuous-time QMC algorithm

First, we focus on the CT-INT algorithm, introduced in Sec. 2.2, which stochastically samples the grand-canonical partition function Z. The formalism is action based where one distinguishes the Gaussian part S_0 and the interaction part S_{int}

$$S_0 = -\sum_{\mathbf{i},\mathbf{j}} \int_0^\beta \int_0^\beta \mathrm{d}\tau \mathrm{d}\tau' c^\dagger_{\mathbf{i},\tau} G_0^{-1}(\mathbf{i}-\mathbf{j}, \tau-\tau') c_{\mathbf{j},\tau'} \tag{4.7}$$

$$S_{\text{int}} = V \sum_{\langle \mathbf{i},\mathbf{j} \rangle} \int_0^\beta \mathrm{d}\tau \left(c^\dagger_{\mathbf{i},\tau} c_{\mathbf{i},\tau} - \frac{1}{2} \right) \left(c^\dagger_{\mathbf{j},\tau} c_{\mathbf{j},\tau} - \frac{1}{2} \right) . \tag{4.8}$$

In Ref. [165], Huffman and Chandrasekharan have demonstrated that the sign of $\langle {S_{\text{int}}}^n \rangle_0$ exactly cancels the alternating sign $(-1)^n$. The requirements of the proof are bipartite lattices with real hopping and repulsive density-density interaction ($V > 0$) between sites of different sublattices. Additionally, both the Hamiltonian, but also each configuration has to respect the particle-hole symmetry. In comparison to Sec. 2.2, this requires the choice of $\alpha = 0$. The symmetry then ensures that the configuration's weight $w(C) = (-1)^n \langle {S_{\text{int}}}^n \rangle_0$ can be expressed as the determinant of a real and anti-symmetric matrix M. Hence, the determinant is non-negative and the simulations do not suffer the negative sign problem. Actually, we have encountered this mechanism already in the previous chapter 4 for the case of attractive interaction at half-filling and the interested reader is referred to there for a more detailed discussion.

4.2.2. Auxiliary-field QMC algorithm

Second, we employ the BSS algorithm in a formulation that preserves the $O(2)$ symmetry, which is discussed in Sec. 4.1, in order to avoid the sign problem. Therefore, we cannot use the conventional decoupling of the interaction in the density or the magnetic channel, e.g. as it is done in Ref. [194], but rather choose the hopping channel as first introduced in Ref. [169]. In principle, we could proceed by introducing a four-valued discrete Hubbard-Stratonovich transformation as in Eq. (2.11) of Sec. 2.3. However, we can here make use of the relation ${\mathcal{T}_{\mathbf{ij}}}^4 = {\mathcal{T}_{\mathbf{ij}}}^2$, with the shorthand notation $\mathcal{T}_{\mathbf{ij}} = c^\dagger_{\mathbf{i}} c_{\mathbf{j}} + c^\dagger_{\mathbf{j}} c_{\mathbf{i}}$, such that

$$\begin{aligned} \mathrm{e}^{-\Delta\tau V \left(n_{\mathbf{i}} - \frac{1}{2}\right)\left(n_{\mathbf{j}} - \frac{1}{2}\right)} &= \mathrm{e}^{\frac{\Delta\tau V}{2}\left[{\mathcal{T}_{\mathbf{ij}}}^2 - \frac{1}{2}\right]} \\ &= \frac{1}{2} \mathrm{e}^{-\frac{V\Delta\tau}{4}} \sum_{\sigma_{\mathbf{ij}} = \pm 1} \mathrm{e}^{-\lambda \sigma_{\mathbf{ij}} \mathcal{T}_{\mathbf{ij}}} . \end{aligned} \tag{4.9}$$

The last identity holds, given that $\cosh(\lambda) = \exp(V\Delta\tau/2)$. This, in turn, requires only a two-valued auxiliary field $\sigma_{\mathbf{ij}}$to make it exact to all orders of $\Delta\tau$, in contrast to the approximation used in the BSS method.

Proceeding along the same line of argument as in Sec. 2.3, we perform a Trotter decomposition and introduce the auxiliary fields from above such that

$$\begin{aligned} Z &= \mathrm{Tr}\left[\mathrm{e}^{-\beta(\mathcal{H}_0+\mathcal{H}_V)}\right] \\ &= \mathrm{Tr}\left[\prod_{\tau}^{N_\tau}\mathrm{e}^{-\Delta\tau(\mathcal{H}_0+\mathcal{H}_V)}\right] \\ &\sim \sum_{\{\sigma\}}\mathrm{Tr}\left[\prod_{\tau}^{N_\tau}\mathrm{e}^{-\Delta\tau\mathcal{H}_0}\prod_{\langle \mathbf{i},\mathbf{j}\rangle}\mathrm{e}^{-\lambda\sigma_{\mathbf{ij},\tau}\mathcal{T}_{\mathbf{ij}}}\right]+\mathcal{O}(\Delta\tau^2) \qquad (4.10) \\ &\sim \sum_{\{\sigma\}}\mathrm{Tr}\left[\prod_{\tau}^{N_\tau}\prod_{\langle \mathbf{i},\mathbf{j}\rangle}\mathrm{e}^{\frac{\mathrm{i}}{2}(\Delta\tau t-\lambda\sigma_{\mathbf{ij},\tau})(\gamma_\mathbf{i}\gamma_\mathbf{j}+\eta_\mathbf{i}\eta_\mathbf{j})}\right]+\mathcal{O}(\Delta\tau^2) \\ &\sim \sum_{\{\sigma\}}W_\gamma(\{\sigma\})W_\eta(\{\sigma\})+\mathcal{O}(\Delta\tau^2)\,. \qquad (4.11) \end{aligned}$$

In the third line, we have dropped a constant normalization factor. The important part, however is the factorization $W(\{\sigma\}) = W_\gamma(\{\sigma\})W_\eta(\{\sigma\})$ of the configurations weight within the Majorana representation[2] as it was first shown in Ref. [169]. Observe that the anti-unitary TRS mentioned in Sec. 4.1 relates the two factors as it interchanges γ and η such that $W_\gamma(\{\sigma\}) = W_\eta^*(\{\sigma\})$. Hence the total weight is non-negative $W(\{\sigma\}) \geq 0$ and the simulation does not suffer from the negative-sign problem. This statement holds even when the algorithm is formulated in terms of the original fermions as in Eq. (4.10) without ever introducing the Majorana basis of Eq. (4.11) explicitly. General considerations on how to avoid the sign problem within the Majorana representation can be found in Ref. [169–171, 195].

4.2.3. Comparison of QMC methods

The CT-INT method stochastically evaluates the series expansion of the grand-canonical partition function to all orders, and imaginary time can be treated as a continuous parameter. In the AF-QMC algorithm, the imaginary time is discretized with a finite resolution $\Delta\tau$ [see Eq. (4.10)]. The systematic error introduced by the discretization acts as a high-energy cutoff. Therefore, the low-energy physics is insensitive to the discretization once $\Delta\tau$ is chosen to be small enough. For the AF-QMC simulations we use $\Delta\tau t = 0.1$ throughout this project.

Various versions of QMC algorithms may lead to remarkably different probability distribution of observables. An example of this is shown in Fig. 4.2 where we present the distribution for m^2, the squared CDW order parameter. Most noticeable is the different power law decay for large values of m^2. By fitting the tail as $P(m^2) = a(m^2)^{2-\varepsilon}$, we extracted the

[2] One way to see the factorization is to express the trace of the fock space as a usual path integral in terms of complex fermions, $\int \mathcal{D}\bar{\phi}\mathcal{D}\phi\prod_\tau^{N_\tau}\prod_{\langle \mathbf{i},\mathbf{j}\rangle}\mathrm{e}^{(\Delta\tau t-\lambda\sigma_{\mathbf{ij},\tau})(\bar{\phi}_{\mathbf{i},\tau}\phi_{\mathbf{j},\tau}+h.c.)}$. Then express the complex Grassmann field ϕ into two real ones, γ and η, in analogy to Eq. (4.5). This yields $\int \mathcal{D}\gamma\mathcal{D}\eta\prod_\tau^{N_\tau}\prod_{\langle \mathbf{i},\mathbf{j}\rangle}\mathrm{e}^{\frac{\mathrm{i}}{2}(\Delta\tau t-\lambda\sigma_{\mathbf{ij},\tau})(\gamma_\mathbf{i}\gamma_\mathbf{j}+\eta_\mathbf{i}\eta_\mathbf{j})}$ that clearly factorizes as γ and η anticommute.

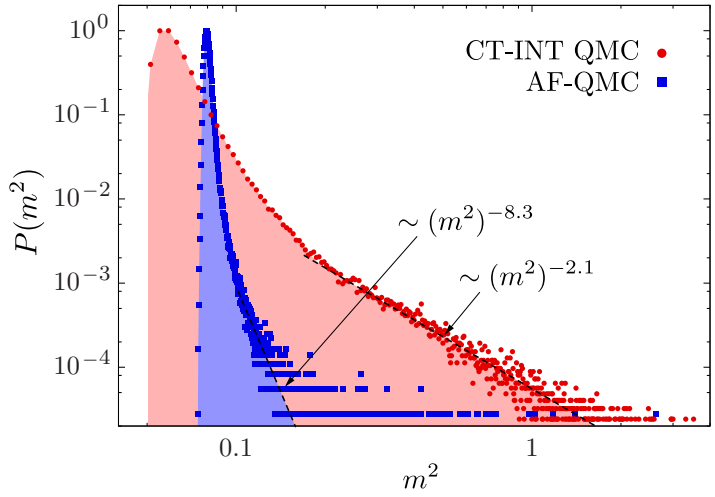

Figure 4.2.: Distribution of the (squared) order parameter for unbinned data from AF-QMC and CT-INT simulations. The data from the CT-INT simulation shows slowly decaying tails which renders the variance ill-defined.

exponent $\varepsilon = 6.3$ for the BSS algorithm whereas the CT-INT method yields $\varepsilon = 0.1$. As it is discussed in Sec. 2.1.2, this is in agreement with the physical constraint of a finite order parameter, $\langle m^2 \rangle = \int_0^\infty d[m^2] P(m^2) m^2 < \infty$. However, the CT-INT method barely meets the requirement such that the variance σ_{m^2} is infinite as $\varepsilon < 1$ (see Sec. 2.1.2). This means that the CT-INT method is not only much more expensive computational wise but also that the central limit theorem is not applicable for this specific observable[3].

Hence, we cannot use this QMC method to detect long-range order and instead employ the more favorable BSS algorithm. One possible explanation for the different behavior of the two methods might be the discrete nature of the BSS configuration space compared to the continuous one in CT-INT. In the latter, it seems to be easier to approach configurations with zero weight $W(C_0) = 0$. Even though C_0 will never be accepted by the QMC method, its vicinity does contribute with arbitrary small weight and leads to rare events. On the other hand, the observable of interest can have a considerable contribution in that region of the configuration space, such that the fat tail is generated. The discrete character of the configuration space might act as a regularization of this issue. However, the AF-QMC method may itself be affected by diverging variances which has been studied recently and a remedy has been proposed in Ref. [196].

The question then arises how to formulate an efficient sign problem free continuous-time QMC algorithm for the Lieb lattice. Here we briefly argue that the method of choice is the CT-AUX algorithm [119, 197] which is sign problem free in the Majorana representation.

[3] According to the central limit theorem, any distribution turns into a Gaussian one, given that it is folded often enough if the original variance is finite. When extracting confidence levels in terms of error bars, it is implicitly assumed that the distribution of the observable/measurement is Gaussian and fully described by its mean and the variance.

Consider the partition function

$$\begin{aligned} \mathrm{e}^{\beta 4L^2K}\frac{Z}{Z_0} &= {Z_0}^{-1}\mathrm{Tr}\,\mathrm{e}^{-\beta\left(\mathcal{H}_0+\Sigma_{\langle\mathbf{ij}\rangle}\left[V\left(n_\mathbf{i}-\frac{1}{2}\right)\left(n_\mathbf{j}-\frac{1}{2}\right)-K\right]\right)} \\ &= \sum_{n=0}^{\infty}\frac{(K-V/4)^n}{n!}\prod_{k=1}^{n}\left(\int_0^\beta \mathrm{d}\tau_k\sum_{\langle\mathbf{i}_k,\mathbf{j}_k\rangle}\right)\langle T\,\mathcal{H}^{\mathrm{int}}_{\langle\mathbf{i}_n\mathbf{j}_n\rangle,\tau_n}\cdots\mathcal{H}^{\mathrm{int}}_{\langle\mathbf{i}_1\mathbf{j}_1\rangle,\tau_1}\rangle_0\,, \end{aligned} \tag{4.12}$$

where K is a real parameter and

$$\begin{aligned} \mathcal{H}^{\mathrm{int}}_{\langle\mathbf{ij}\rangle} &= 1-\frac{V}{K-V/4}\left[\left(n_\mathbf{i}-\frac{1}{2}\right)\left(n_\mathbf{j}-\frac{1}{2}\right)-\frac{1}{4}\right] \\ &= 1+\frac{V}{2K-V/2}{\mathcal{T}_\mathbf{ij}}^2 \\ &= \frac{1}{2}\sum_{s=\pm1}\mathrm{e}^{s\alpha\mathcal{T}_\mathbf{ij}}\,. \end{aligned} \tag{4.13}$$

The last identity follows again from the relation ${\mathcal{T}_\mathbf{ij}}^4={\mathcal{T}_\mathbf{ij}}^2$ and hence the necessary choice of α is given by $\frac{V}{2K-V/2}+1=\cosh(\alpha)$. Therefore the algorithm can only be formulated for $K>V/4$. In general, the parameter K can be tuned to maximize the efficiency of the algorithm and also to avoid numerical instabilities due to nearly singular matrices [119]. With this expression, the partition function reads

$$\mathrm{e}^{\beta 4L^2K}\frac{Z}{Z_0}=\sum_{n=0}^{\infty}\frac{(K-V/4)^n}{2^n\,n!}\prod_{k=1}^{n}\left(\int_0^\beta \mathrm{d}\tau_k\sum_{\langle\mathbf{i}_k,\mathbf{j}_k\rangle}\right)\langle T\,\mathrm{e}^{s_n\alpha\mathcal{T}_{\mathbf{i}_n\mathbf{j}_n}(\tau_n)}\cdots\mathrm{e}^{s_1\alpha\mathcal{T}_{\mathbf{i}_1\mathbf{j}_1}(\tau_1)}\rangle_0 \tag{4.14}$$

and this method is also free of the negative-sign problem due to the same reasons discussed in Sec. 4.2.2.

The CT-AUX methods can also be used to interpolate between the BSS and the CT-INT approach as, on one hand, it is a weak-coupling expansion similar to the latter and, on the other hand, uses a Hubbard-Stratonovich decompositions as in the former method Ref. [198]. Observe that the average expansion order is proportional to $\langle\Sigma_{\langle\mathbf{ij}\rangle}\,\mathcal{H}^{\mathrm{int}}_{\langle\mathbf{ij}\rangle}\rangle$ such that it diverges linearly for large $K\to\infty$. These vertices will then be distributed evenly in space-time. To approach the continuous time limit in the BSS method, we have to set $\Delta\tau\to\infty$ that also generates a divergent density of operators and auxiliary fields. In the limit $K=0$ the expansion sampled by the CT-AUX algorithm is identical to the one of the CT-INT method. However, the condition $K>V/4$ for the hopping decomposition of this model, is blocking the CT-AUX algorithm as an interpolation between the BSS and CT-INT methods here.

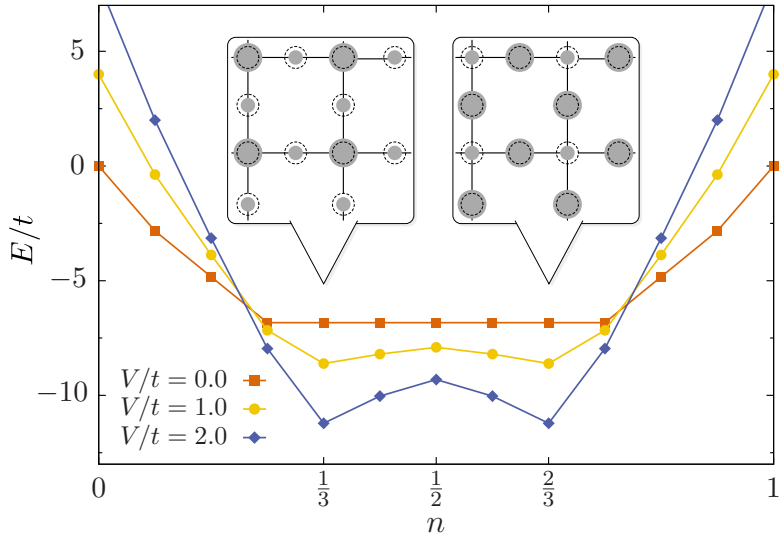

Figure 4.3.: Ground-state energy E for fixed electron density n and various interaction strengths V on an $L = 2$ lattice from exact diagonalization. The distribution of the charge density for the ground state with $1/3$- and $2/3$-filling is illustrated in the insets. Lines are meant as guides to the eye only.

4.3. Results

First, we study a 2×2 lattice employing exact diagonalization and present the ground-state energy as a function of fixed particle number for various values of interaction strength V in Fig. 4.3. Due to the presence of the flat band at the chemical potential, the derivative of the free energy with respect to the particle number vanishes $dF/dN = 0$ such that the system is thermodynamically unstable. Interestingly, the instability drives the model away from half filling and towards a filling fraction of $n = 1/3$ or $n = 2/3$. The ground states of the sectors with a fixed number of particles are generically degenerate, only for $N = 4$ and $N = 8$, we find a unique state. The insets visualize the density distribution of both states, where the area of the gray discs is proportional to the local density and the dotted circles represent a homogeneous distribution as a reference. This clearly characterizes them as CDW states that break PHS and that are linked to each other by a particle-hole transformation. Also the overall twofold ground-state degeneracy is in agreement with the theorem of Ref. [174].

Second, we employ both QMC methods in order to study larger lattices and test the hypothesis of spontaneous symmetry breaking by the formation of charge order at finite temperatures. Hence the density correlation function are used (i) to examine the spatial pattern and the according length scale as well as (ii) to obtain the (squared) order parameter and extrapolate it to the thermodynamic limit. Once we have established the existence of the symmetry broken phase, we continue with a proper finite-size scaling analysis to both confirm the Ising nature and determine the critical temperature of the phase transition in Sec. 4.3.1. Finally, we present the single-particle spectra in Sec. 4.3.2 which equally detect the symmetry bro-

ken phase. In the previous Sec. 4.2.3, we have shown that the order parameter suffers from fat tails for the CT-INT method such that the following data has been generated using the AF-QMC algorithm, unless stated otherwise as in Sec. 4.3.2.

In order to examine the spatial pattern of the charge distribution, let us define the density correlation function

$$C(r) = \frac{1}{4L^2} \sum_{\mathbf{i},\mathbf{j}} \left(\langle n_\mathbf{i} n_\mathbf{j} \rangle - \langle n_\mathbf{i} \rangle \langle n_\mathbf{j} \rangle \right) \delta((\mathbf{i}-\mathbf{j}) - \frac{r}{2}\mathbf{a}_1) \, . \tag{4.15}$$

The resulting pattern are shown in Fig. 4.4(a) representing a path starting on say sublattice A of one unit cell. Then the path contains sites of alternating A and C orbitals where the site of $r = 1$ the same unit cell, $r = 2$ and $r = 3$ represents the neighboring one, up to the maximal distance when $r = L$. Here we used a 12×12 lattice, a coupling strength $V/t = 2$ and various inverse temperatures β. First of all, the alternating sign of the correlation function $C(r)$ confirms the CDW pattern. The correlation decays exponentially at high temperatures of $\beta t = 1$, best seen in the inset. For low temperatures ($\beta t = 3$), the amplitude $|C(r)|$ seems to remain constant for the largest accessible distances. This behavior is consistent with a CDW state for $\beta t = 3$. The data for $\beta t = 2$ requires a more careful analysis with respect to system size.

Hence, let us define a finite size version of the order parameter $m(T,L) = \sqrt{\mathrm{Tr}[\mathbf{N}(\mathbf{Q}=\mathbf{0})]}$, which – strictly speaking – only becomes the order parameter in the thermodynamic limit $L \to \infty$. Here, it is useful to slightly modify the correlation function from above by essentially, taking the A, B and C sublattice as orbitals and use the (linearized) position $x = \{1, \cdots, L^2\}$ that now refers to the unit cell of the lattice. Then we have $N_{ab}(\mathbf{Q}) = \frac{1}{L^2} \sum_x^{L^2} \langle n_1^a n_x^b \rangle - \langle n_1^a \rangle \langle n_x^b \rangle$ as a 3×3 matrix. Figure 4.4(b) shows the extracted (squared) order parameter $m(T,L)$ for various temperatures as a function of linear system size $L = 4, 6, 8, 10, 12,$ and 15 in a logarithmic plot. Observe that the curve for $\beta t = 2$ shows a clear downturn upon increasing the system size, hence it extrapolates to $m = 0$ for $L \to \infty$ such that the thermodynamic limit is disordered. Actually, this trend is also present for $\beta t < 2.4$. In contrast, temperatures below $\beta t = 2.5$ remain rather constant upto the largest available lattice size. Therefore, the data is consistent with a finite-temperature phase transition between $\beta t = 2.4$ and $\beta t = 2.5$. In the upcoming section we will determine a critical value $\beta_c t = 2.491(5)$ for the phase transition by using the finite-size scaling analysis.

In addition, we also tested various other correlation function, mainly for the current channel, without detecting any sign of long-range order (not shown). Hence, time-reversal symmetry is conserved and there does not exist a spontaneously generated, topological QAH state within this model.

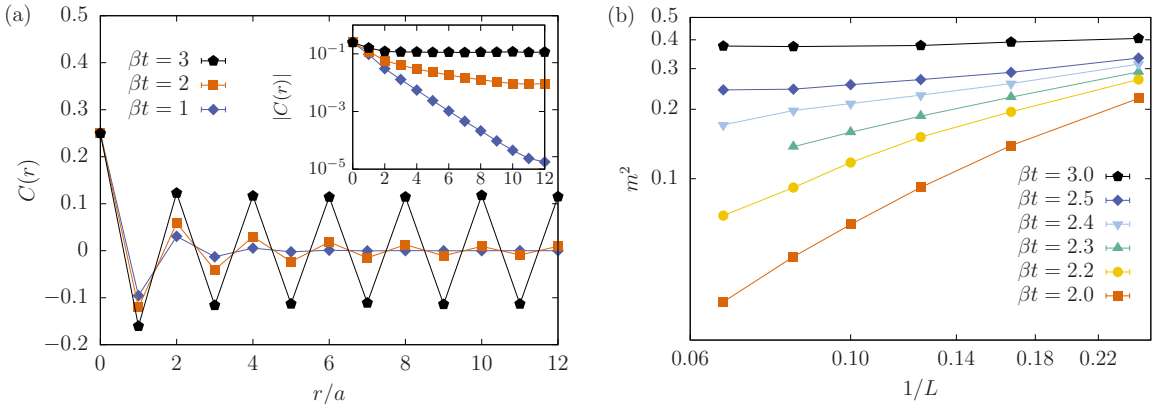

Figure 4.4.: Density correlation function for $L = 12$ and at $V/t = 2$ as a function of spatial separation along the lattice axes (a). The inset displays the growing correlation length on a semi-logarithmic scale. Panel (b) shows the the finite-size behavior of the (squared) order parameter on a double-logarithmic scale. The data is compatible with a phase transition between $\beta t = 2.4$ and $\beta t = 2.5$.

4.3.1. Finite-Temperature phase transition

To test the claimed Ising nature of the phase transition, we perform a finite-size scaling ansatz

$$m_i(T_i, L_i) = L_i^{-\beta/\nu} \mathcal{F}[(T_i - T_c)/T_c \, L_i^{1/\nu}] \,, \tag{4.16}$$

with the critical exponents $\beta = 1/8$ and $\nu = 1$ that are known for the two dimensional Ising universality class and kept fixed during the following analysis. T_c is the critical temperature at which the phase transition takes place and $\mathcal{F}$ is a non-universal function. In the following, we will approximate $\mathcal{F}$ in the vicinity of the critical temperature T_c by a polynomial $\tilde{\mathcal{F}}(x) = \sum_{k=0}^{k_{\max}} u_k x^k$ up to fourth order ($k_{\max} \leq 4$). This leaves at the most six parameters that are determined by fitting the ansatz to the Monte Carlo data $m_i(T_i, L_i)$ weighted according to their statistical uncertainty $\sigma_{m,i}$. The quality of the fit is measured by χ^2/d.o.f. with

$$\chi^2 = \sum_{i=1}^{N_{\text{data}}} \left\{ \frac{m_i(T_i, L_i) L_i^{\beta/\nu} - \tilde{\mathcal{F}}[(T_i - T_c)/T_c \, L_i^{1/\nu}]}{\sigma_{m,i}} \right\}^2 \tag{4.17}$$

and the fitting procedure has to minimize this quantity. We have also compared our finite-size scaling method to a recently proposed method [199], based on Bayesian statistics, and we obtained the same critical temperatures within error bars (not shown).

The extracted critical temperatures are summarized in Tab. 4.1 that also indicates the order of the polynomial $\tilde{\mathcal{F}}(x)$ as well as χ^2/d.o.f. for the goodness of the fit. Observe that the latter is of order 1 for every investigated interaction strength. This nicely confirms the Ising nature of the phase transition. In Figs. 4.5(a)-(e), we present a visualization of the data collapse and

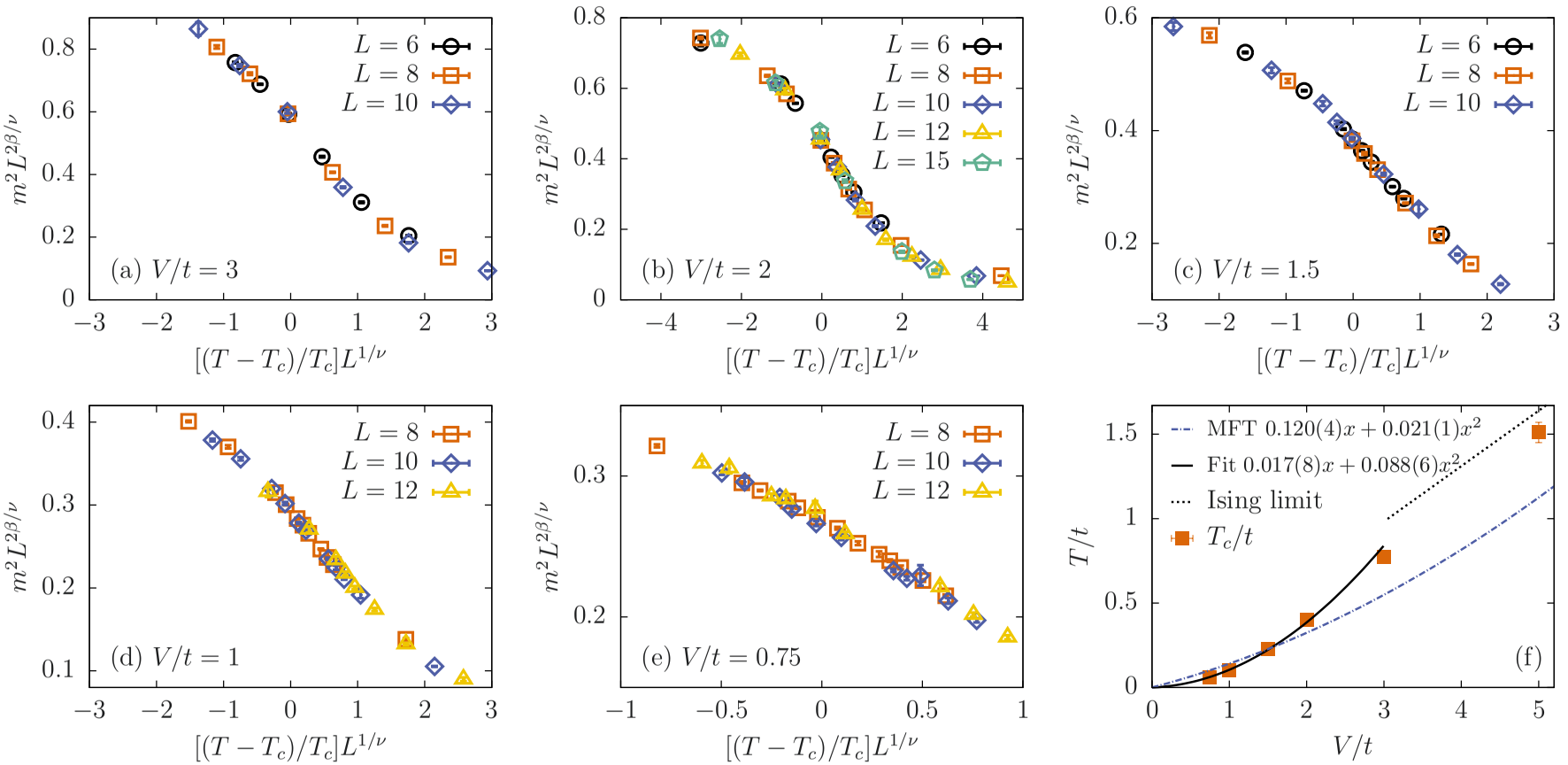

Figure 4.5.: Finite-size data collapses (a–e) of the (squared) order parameter across the thermal phase transition using the critical exponents of the two-dimensional Ising model for different interaction strength V. Panel (f) shows the behavior of the extracted critical temperatures as a function of V compared to mean-field theory (MFT) results and the classical Ising-limit for strong Coulomb repulsion[4]

V/t	0.75	1	1.5	2	3
T_c/t	0.0619(2)	0.1029(2)	0.2277(5)	0.4013(6)	0.773(2)
k	3	4	3	3	2
χ/d.o.f.	21.92/15	41.21/20	18.24/12	19.35/14	4.45/8

Table 4.1.: For each interaction strength V the critical temperature T_c/t is obtained from the fit of the (squared) order parameter to a polynomial of order k.

panel (f) shows the extracted $T_c(V)$ as a function of coupling strength V/t. At $V/t = 5$, the resolution $\Delta\tau t = 0.1$ of inverse temperatures is too coarse for an accurate fit of the scaling function. Therefore we used the crossing points of $mL^{\beta/\nu}(T)$ together with a conservative error to estimate $T_c(V/t = 5) = 1.51 \pm 0.06$.

According to the Stoner criterion for the weak coupling regime, one would expect a linear relation $V \sim T$ resulting from the Curie-type non-interacting susceptibility for localized states. This behavior can indeed be seen in the standard charge-order mean-field approximation. However, as a consequence of many-body correlations, the QMC simulation result has a dominating quadratic contribution. For strong Coulomb repulsion $|V| \gg 1$, the t-V model maps onto a classical two dimensional Ising model, such that the critical temperature $T_{c,t\text{-}V} = T_{c,\text{Ising}}|V|/4$ [194] increases linearly with interaction strength V. For the Ising model on the Lieb lattice we have computed the estimate $T_{c,\text{Ising}} = 1.310(1)$ and indicate the strong coupling limit as the dotted line in Fig. 4.5(f). This approximation is consistent with the critical temperatures extracted from the QMC data.

4.3.2. Dynamics

The symmetry breaking is equally visible in the single-particle spectrum as the PHS protects the zero-energy flat band. Therefore we measure the imaginary time-resolved Green's function $G(\mathbf{k}, \tau)$ and perform an analytic continuation using the stochastic maximum-entropy method to extract the spectrum $A(\mathbf{k}, \omega)$ as introduced in Refs. [139, 200]. For this observable, the CT-INT method does not suffer from fat tails, essentially because it is a lower order correlation function[5] [201]. Hence we used this QMC version here and the results are shown in Fig. 4.6.

Panel (a) displays the fermion spectrum representative for temperatures above the phase transition ($T > T_c$). The band structure is very similar to the non-interacting case, up to a renormalization of the band width, where the main difference is spectral broadening due to

[4] At $V/t = 5$, the resolution $\Delta\tau t = 0.1$ of inverse temperatures is too coarse for an accurate fit of the scaling function. Therefore we used the crossing points of $mL^{\beta/\nu}(T)$ together with a conservative error to estimate $T_c(V/t = 5) = 1.51 \pm 0.06$.

[5] It is simply the single-particle Green's function whereas the density correlation function, upon Wick decomposition, is given by the product of two of them.

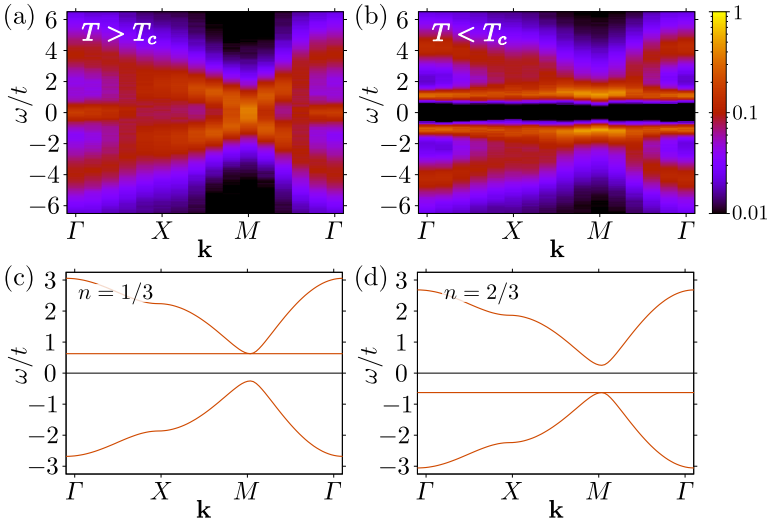

Figure 4.6.: The one-particle spectral function at temperature (a) $T = 0.5$ above T_c and (b) $T = 0.2$ below the Ising transition for an $L = 10$ lattice and $V/t = 2$. The spectrum in (b) can be interpreted as the superposition of the dispersions for (c) 1/3-filling and (d) 2/3 filling (here obtained from mean-field calculations).

temperature[6] and the finite lifetime of the bare fermions. Most importantly, the zero-energy flat band persists indicating the preservation of particle-hole symmetry.

Panel (b) shows a spectrum representing temperatures below the critical value ($T < T_c$) and a clear single-particle gap is visible as expected for the insulating CDW. Hence, the PHS is broken and the flat band remains (almost) dispersionless but appears to be doubled as well as shifted to a finite energy $\omega \sim \pm 1$. This spectrum, including the very unconventional doubling of bands, is understandable as a combination of both CDW states introduced from ED. In panels (c) and (d), we present the single-particle spectrum for those states on a mean-field level. Panel (c) has the perfectly flat band shifted to higher energies such that the filling fraction is $n = 1/3$ whereas it is shifted to lower energies in panel (d) leading to a filling of $n = 2/3$. As the QMC has to preserve PHS for each configuration, the results also are particle-hole symmetric, and matches an equal weight combination of both CDW states:

$$G_{n=1/2}(\mathbf{k},\tau) = \frac{1}{2}\left[G_{n=1/3}(\mathbf{k},\tau) + G_{n=2/3}(\mathbf{k},\tau)\right] . \tag{4.18}$$

In this sense, we even recognize the instability towards finite doping, even though the simulation is always at half filling and we cannot access the two ground states individually.

[6] In Sec. 2.4 we discussed that the spectrum is essentially defined by single-particle excitations of the ground state, given that the temperature is low enough. At high temperatures, other low-energy states also contribute according to their Boltzmann weight which broadens the formerly sharp lines.

4.4. Discussion

The numerical simulations were quite challenging, despite the absence of the negative-sign problem, but they also opened doors to previously inaccessible parameter regimes away from half filling. The observed fat tails, which may render a QMC method inapplicable, are dependent on the flavor of the QMC as they were much worse for the CT-INT method compared to the more favorable auxiliary-field approach. We conjectured that the CT-AUX algorithm might be the method of choice for this model.

Exact diagonalization indicated two CDW states, related by a particle-hole transformation, as the ground states of the interacting model which drive the system away from half filling. Using the BSS method, we presented strong evidence for spontaneous breaking of PHS at finite temperatures. The according phase transition belongs to the two dimensional Ising universality class and we find a critical temperature $T_c(V)$ that predominantly scales quadratically with weak interaction strength $V < 1$ whereas mean-field theory predicts a leading linear order. This can be taken as a sign of strong fluctuation effects due to the flat band that are neglected on the mean-field level. Finally, we have shown that the single-particle spectrum, even though constraint to be particle-hole symmetric, should be interpreted as a linear superposition of two CDW ground states with a filling fraction of $n = 1/3$ and $n = 2/3$, respectively.

One important observation is the relation between charge order and finite doping with $\langle n - 3/2 \rangle \neq 0$ where n is the particle density per unit cell, due to the unequal-size bipartition of the Lieb lattice. This effect raises the question, if one can use this setup to simulate other interesting models with finite doping that otherwise suffer from the negative-sign problem. One possible scenario contains two layers where one of them is defined on the Lieb lattice (1) and the other one is the target layer of interest (2) with an assumed $SU(N)$ symmetry. The two subsystems are then coupled via an interaction of the form $\mu(n_i^{(1)} - 3/2)(n_i^{(2)} - N/2)$ such that the CDW order in the Lieb lattice induces an effective chemical potential $\mu_{\text{target}} = \mu \langle n_i^{(1)} - 3/2 \rangle$ for the target subsystem, once the system is below T_c. Here we assumed that the nature of the phase transition remains unaffected by the coupling of the Lieb lattice part to the target system[7].

[7] Alternatively one can break particle-hole symmetry explicitly on the Lieb lattice, by adding a staggered chemical potential. Within the Majorana representation, this will not introduce a sign problem (cf. Ref. [171]).

CHAPTER 5

Reduction of the topological classification

Recently there has been rapid progress in topological quantum matter [14–17], motivated by the discovery of topological insulators [11–13] which are insulating in the bulk but exhibit gapless excitations at the boundary. Non-interacting systems with given non-spatial symmetries, such as time-reversal or particle-hole symmetry, have been characterized extensively [18, 19]. The presence of interaction gives rise to the notion of symmetry-protected topological (SPT) phases that describe short-range entangled gapped states with a given symmetry. Importantly, quantum states of the same phase can be deformed into each other without closing the gap while preserving the symmetry, representations of different topology, however, may not be connected adiabatically. Non-trivial SPT phases exhibit gapless boundary excitations, similar to the uncorrelated topological states.

The inclusion of interaction can modify free fermion models in at least three different ways: (i) spontaneous symmetry breaking can induce topological non-trivial mass terms [48], which motivated the project discussed in Ch. 4, (ii) interaction can give rise to topological order with long-range entanglement as in fractional quantum Hall states [65, 66], fractional topological insulators [67] or quantum spin liquids [68–71], all of which do not have a non-interacting analog, or (iii) correlations may reduce the topological classification of free fermion system by adiabatically connecting states of formerly distinct phases.

The first example of such a reduction was considered by Fidkowski and Kitaev [52]. They studied a spinless superconductor in one dimension with an unconventional time-reversal symmetry ($\mathcal{T}^2 = +1$), representing class BDI, and showed that a specifically chosen interaction gaps out 8 topological Majorana boundary modes and adiabatically connects bulk states whose winding number differ by 8. This demonstrates the "collapse" of the non-interaction classification form $\mathbb{Z}$ to $\mathbb{Z}_8$. In comparison to this study, the gap opening of protected edge

modes in Ch. 3 is accompanied by spontaneous symmetry breaking. Later on, this result has been generalized to different symmetry classes and higher dimensions [54–64]. These investigations often make use of the bulk-boundary correspondence, e.g., by showing that interaction symmetrically gap the topological modes at the boundary [54–56] or in 0D defects that follow from dimensional reduction [57,58], by investigating the signatures of these boundary states in the entanglement spectrum [59, 60], or in braiding statistics [61]. An alternative approach is based on group cohomology [62].

Complementary to this, we aim to construct an explicit adiabatic connection of the bulk states that represent topologically distinct phases in the free fermion classification. Here, we focus on symmetry class A' in two dimensions where the classification is expected to be reduced from $\mathbb{Z}$ to $\mathbb{Z}_4$. To this end, we construct SPT phases that differ by 4 in the winding number, introduce an interaction term that follows the rules of Ref. [58], and determine the phase diagram. We find an extended region of spontaneous symmetry breaking – in addition to the non-interacting semi-metal – that separates the topologically distinct phases. Interestingly, we are able to frustrate the long-range order that in turn introduces a first order phase transition which then blocks the adiabatic path. The given phase diagram suggest that the guidelines, which have been uncovered so far, may be necessary, but they do not seem to be sufficient.

The remainder is structured as follows. In Sec. 5.1, we define the microscopic model and discuss its symmetries. In Sec. 5.2, we analyze possible mean-field scenarios with spontaneous symmetry breaking, identify the most relevant option and argue that the exact solution of the atomic limit provides reasonable hope for the existence of an adiabatic path. A brief discussion of the quantum Monte Carlo (QMC) method is found in Sec. 5.3 before we present the numerical results in Sec. 5.4 and conclude with a discussion of their implications in Sec. 5.5.

This project has been studied in collaboration with R. Queiroz and E. Khalaf under the supervision of F. F. Assaad and has been published in Ref. [P1].

5.1. Model & symmetries

We begin by introducing the free fermion part of the model $\mathcal{H}_0 = \sum_{\mathbf{k}} \Psi^\dagger_{\mathbf{k}} H(\mathbf{k}) \Psi_{\mathbf{k}}$ which essentially represents two copies of a Quantum-Hall system with opposite topology, similar to the construction of some quantum spin Hall models [8, 11, 202, 203]. We have

$$H(\mathbf{k}) = t \begin{pmatrix} H_+(\mathbf{k}) & 0 \\ 0 & H_-(\mathbf{k}) \end{pmatrix} \tag{5.1a}$$

$$H_\pm(\mathbf{k}) = \sin(k_x)\sigma_x + \sin(k_y)\sigma_y \pm m(\mathbf{k})\sigma_z + \Delta[\sin^2(k_x) + \sin^2(k_y)]\sigma_0 \tag{5.1b}$$

$$m(\mathbf{k}) = 2 + \lambda + \cos(k_x) + \cos(k_y)\,, \tag{5.1c}$$

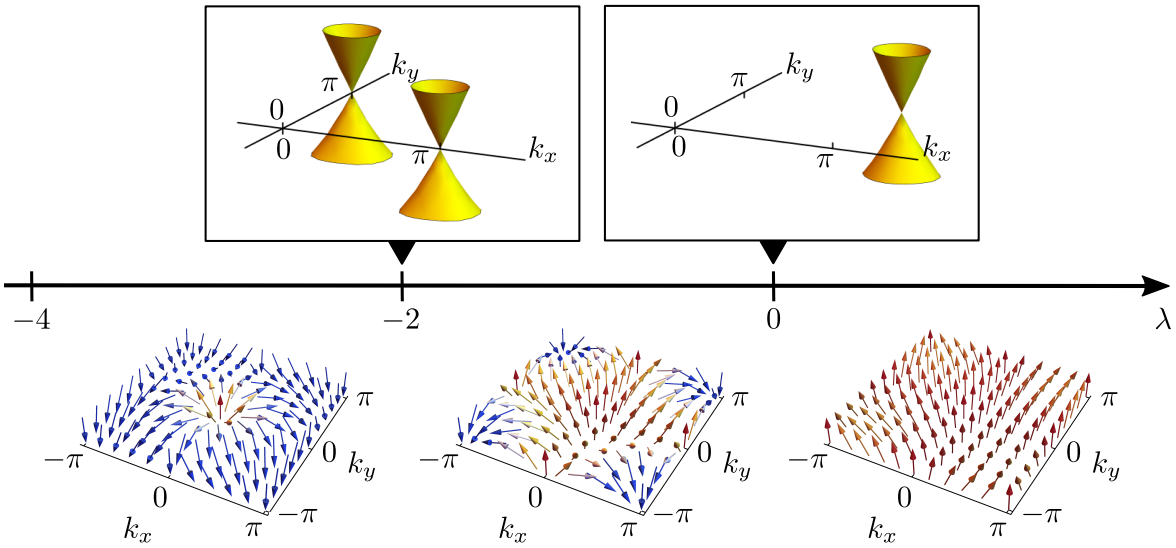

Figure 5.1.: Graphical visualization of $\mathcal{H}_0$ showing the localization of the Dirac cone(s) for $\lambda = -2$ and $\lambda = 0$. The 3D-vector plots depict the orientation of $\hat{\mathbf{d}}$ representing topological (left and middle) and trivial (right) insulators. For readability, we also color-coded the z-component.

where $\Psi^\dagger_{\mathbf{k}}$ is the creation operator of a four-component spinor with momentum $\mathbf{k}$. The basic building blocks $H_\pm(\mathbf{k})$ represent lattice regularization of the quantum Hall effect [7]. The energy scale is set by t which will also be used as the unit of energy ($t = 1$) throughout the rest of this project. The first two terms in Eq. (5.1b), $\sin(k_x)\sigma_x + \sin(k_y)\sigma_y$, host one Dirac cone at each of the four time-reversal invariant momenta that can be gapped by $m(\mathbf{k})\sigma_z$. For the specific values of $\lambda = 0$, $\lambda = -2$ or $\lambda = -4$ at least one of the Dirac cones remains massless (compare with Fig. 5.1) whereas any other value describes an insulating state. The last term in Eq. (5.1b), $\Delta = 0.25$ is used to break the particle-hole symmetry within $H_\pm(\mathbf{k})$.

At this point, the model obeys a unitary $U(1)$ symmetry generated by $R = \tau_z \otimes \mathbf{1}$, such that $H_\pm$ act on the respective $\pm$ sector of R and the two sectors cannot mix. Additional, there is one independent, anti-unitary time-reversal symmetry defined by $\mathcal{K}\,\tau_x \otimes \sigma_y$ with complex conjugation $\mathcal{K}$. Hence the model belongs to symmetry class A' and is very closely related to the well know topological insulators (TIs). There, one may introduce spin-orbit coupling which breaks the spin conservation as long as the time-reversal symmetry is respected.

In order to discuss the topology of the gapped states, it is useful to first focus on H_+, define a vector $\mathbf{d} = (\sin(k_x), \sin(k_y), m(\mathbf{k}))$ and introduce the winding number $w_+ = \frac{1}{4\pi}\iint_{\mathrm{BZ}} \hat{\mathbf{d}} \cdot (\partial_{k_x}\hat{\mathbf{d}} \times \partial_{k_y}\hat{\mathbf{d}})$ with $\hat{\mathbf{d}} = \mathbf{d}/|\mathbf{d}|$ [11]. As it is visualized in Fig. 5.1, the parameter λ tunes the system from a trivial insulator ($\lambda > 0$) through a semi-metal with a Dirac cone at $\mathbf{k} = (\pi, \pi)$ ($\lambda = 0$) to a topological insulator ($-2 < \lambda < 0$) of winding $+1$. At $\lambda = -2$, the system exhibits one Dirac cone at each $\mathbf{k} = (0, \pi)$ and $\mathbf{k} = (\pi, 0)$. The winding number of the full Hamiltonian is then given as $w = 1/2(w_+ - w_-)$ where $w_- = -w_+$ due to the time-reversal

symmetry connecting the two sectors. Observe that small values of Δ only modify the energy of the bands and, as long as the band gap does not close, the wave functions do not change. Hence the topology is insensitive to (small) Δ.

According to predictions in previous studies [58], we expect a reduction of the topological classification from $\mathbb{Z}$ to $\mathbb{Z}_4$. Therefore, we introduce four copies of the above system by modifying $\mathcal{H}_0 = \sum_{\mathbf{k},o} \Psi^\dagger_{\mathbf{k},o} H(\mathbf{k}) \Psi_{\mathbf{k},o}$, where $o \in \{A,B,C,D\}$ labels the copy and will be referred to as layer degree of freedom. In Ref. [58], the authors describe a scheme which introduces a lattice of zero-dimensional defects that inherit the bulk topology in the sense that those defects exhibit n topologically degenerate zero modes where n matches the topological invariant of the bulk. For two-dimensional models, this is done by first realizing one-dimensional edge modes at a domain wall and secondly adding an oscillating mass term along this domain wall with appropriately chosen symmetries, such that each node of the mass term localizes zero modes. This construction in turn allows to derive an explicit interaction term which gaps those defects without breaking any symmetry. Using this recipe, we designed the following interaction

$$\mathcal{H}_{\text{int}} = U \sum_{\mathbf{i},\alpha=\pm} \Psi^\dagger_{\mathbf{i},A} \gamma_5 P_\alpha \Psi_{\mathbf{i},B} \Psi^\dagger_{\mathbf{i},D} \gamma_5 P_\alpha \Psi_{\mathbf{i},C} + h.c. \tag{5.2a}$$

$$P_\alpha = \frac{1}{2}(1 + i\alpha\gamma_3\gamma_4)\,, \tag{5.2b}$$

where the γ matrices act on the original Dirac components [$\gamma^{1,2} = \mathbf{1} \otimes \sigma^{x,y}$, $\gamma^{3,4,5} = \tau^{z,y,x} \otimes \sigma^z$]. Observe that $R = i\gamma_4\gamma_5$ and therefore R, γ_4 and γ_5 form an $SU(2)$ algebra such that the interaction reduces the R symmetry from a continuous $U(1)$ to a discrete $\mathbb{Z}_2$ that transforms $\gamma_5 \to -\gamma_5$. Physically, the interaction introduces correlated pair hopping of electrons between layers $A \to B$ and $D \to C$ while flipping the R charge. This term does allow, e.g., two $R = +$ electrons being scattered into two $R = -$ ones such that the R charge is only conserved modulo 2 which illustrates the $U(1) \to \mathbb{Z}_2$ reduction[1].

5.2. Mean-field theory & atomic limit

Before moving on to the method and numerical results, let us develop an intuition on possible phases. We will first discuss various mean-field scenarios that might break some of the protecting symmetries. Then we will solve the atomic limit analytically. This provides an additional argument, complementary to the edge state analysis of Ref. [58], on the existence of an adiabatic path and the according reduction of the topological classification.

To discuss mean-field scenarios, it is very useful to divide the four layers into two pairs,

[1] The attentive reader might have realized that this correlated hopping actually changes R by 4. However, in the canonical ensemble, the total number of particles is conserved and at half-filling with an even number of fermions, the total R charge itself has to be even and thus this reduces the $U(1)$ symmetry to $\mathbb{Z}_2$.

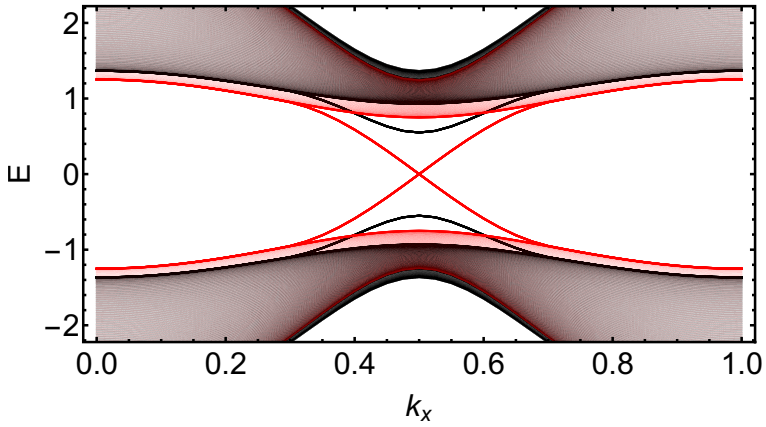

Figure 5.2.: Spectrum of the model defined in Eq. (5.1) in ribbon geometry representing the symmetric (red) and the symmetry broken scenario (black) with an mean-field order parameter $m = 0.6$ and $\mathcal{H}_{\mathrm{MF}} = m\sum_{\mathbf{i}} M^x_{\mathbf{i}}$.

namely (A,B) and (C,D) and introduce the two pseudo-spin operators with $\beta = x,y$

$$S^{1,\alpha,\beta}_{\mathbf{i}} = (\Psi^\dagger_{\mathbf{i},A}\Psi^\dagger_{\mathbf{i},B})s^\beta \otimes \gamma_5 P_\alpha (\Psi_{\mathbf{i},A}\Psi_{\mathbf{i},B})^T \tag{5.3a}$$

$$S^{2,\alpha,\beta}_{\mathbf{i}} = (\Psi^\dagger_{\mathbf{i},C}\Psi^\dagger_{\mathbf{i},D})s^\beta \otimes \gamma_5 P_\alpha (\Psi_{\mathbf{i},C}\Psi_{\mathbf{i},D})^T \tag{5.3b}$$

where the Pauli matrices s^β act on layer index within each pair. This allows us to rewrite the interaction as

$$\mathcal{H}_{\mathrm{int}} = \frac{U}{8}\sum_{\substack{\mathbf{i},\alpha=\pm,\\ \beta=x,y}}\sum_{\tau=\pm}\tau\left(S^{1,\alpha,\beta}_{\mathbf{i}} + \tau S^{2,\alpha,\beta}_{\mathbf{i}}\right)^2 \tag{5.4}$$

and shows the possibility to minimize the energy for $\tau = -$, given that $U > 0$, by the generation of pseudo-magnetic order in the xy-plane of

$$M^\beta_{\mathbf{i}} = \sum_{\alpha=\pm}\left(S^{1,\alpha,\beta}_{\mathbf{i}} - S^{2,\alpha,\beta}_{\mathbf{i}}\right). \tag{5.5}$$

This order parameter breaks the R symmetry and anti-commutes with Eq. (5.1a) such that it introduces a gap in both the bulk and edge state spectrum. As Eq. (5.4) points out, the interaction is symmetric under rotation around the z-axis of the pseudo-spins, and hence the orientation of M within the xy-plane is arbitrary and also breaks this symmetry spontaneously.

Without loss of generality, we choose the x direction for the magnetization and introduce $\mathcal{H}_{\mathrm{MF}} = m\sum_{\mathbf{i}} M^x_{\mathbf{i}}$. In Fig. 5.2 we present the energy spectrum for $\mathcal{H}_0 + \mathcal{H}_{\mathrm{MF}}$ with open boundary condition in y direction. The solid black lines represent a non-zero mean-field expectation value $m > 0$ and the red lines overlay the symmetric version ($m = 0$). We can clearly observe the introduced gap of the former massless Dirac edge state.

To make the connection between this mean-field scenario and the phase diagram, let us discuss the limiting cases. Keeping the interaction strength small, we expect stable Dirac cones for $\lambda \sim 0$ and $\lambda \sim -2$ as the density of states at the Fermi level vanishes at half filling [72, 73, 204–207]. The insulating states provide an intrinsic scale of energy, namely the band gap, such that the correlation should reach comparable strength before it leads to significant changes.

The more interesting limiting case is the strongly interacting one with $U/t \gg 1$. Starting from the limit $t = 0$, we can solve $\mathcal{H}_{\text{int}}$ analytically, as the lattice sites completely decouple and we are left with a zero-dimensional problem. In the following, we calculate the full spectrum and show that there is a unique ground state. For readability, let us drop the position index $\mathbf{i}$ for the remainder of this analytic derivation. Note that $P_\pm$ act as projectors such that the Fock space can be decomposed into two separate blocks which have an identical spectrum. Hence it is sufficient to focus on one subspace, say $\mathcal{H}_+$. Let ε_i be an eigenvalue of $\mathcal{H}_+$ with degeneracy g_i. The full spectrum is then given by $\varepsilon_i + \varepsilon_j$ with degeneracy $g_i g_j$.

In the previous Sec. 5.1, we have chosen a basis for the γ-matrices in which R is diagonal to remind the reader of popular QSH models. Here, however, it is more convenient to choose a different basis in which both $\gamma_5 = \tau^x \otimes \sigma^z$ and $i\gamma_3\gamma_4 = \tau^x \otimes \sigma^z$ are diagonal[2]. Note that the local fermion degrees of freedom $\mathcal{H}_+$ within one layer o is then fully classified by the eigenvalues $s_5 = \pm$ of γ_5 such that $P_+\Psi_{o,s_5} = \Psi_{o,s_5}$ and $\gamma_5\Psi_{o,s_5} = s_5\Psi_{o,s_5}$. This leads to the definition of four new spin operators:

$$\mathbf{S}_a = (\Psi^\dagger_{A,+}\Psi^\dagger_{B,+})\boldsymbol{\sigma}(\Psi_{A,+}\Psi_{B,+})^T \tag{5.6}$$

$$\mathbf{S}_b = (\Psi^\dagger_{A,-}\Psi^\dagger_{B,-})\boldsymbol{\sigma}(\Psi_{A,-}\Psi_{B,-})^T \tag{5.7}$$

$$\mathbf{S}_c = (\Psi^\dagger_{C,+}\Psi^\dagger_{D,+})\boldsymbol{\sigma}(\Psi_{C,+}\Psi_{D,+})^T \tag{5.8}$$

$$\mathbf{S}_d = (\Psi^\dagger_{C,-}\Psi^\dagger_{D,-})\boldsymbol{\sigma}(\Psi_{C,-}\Psi_{D,-})^T\,, \tag{5.9}$$

such that the Hamiltonian can be written as $\mathcal{H}_+ = h_{ac} - h_{ad} - h_{bc} + h_{bd}$ where we used the shorthand notation $h_{ij} = U(S^+_i S^-_j + h.c.)$. Note that this has mapped Eq. (5.2) to a model with four sites on a ring (*a*-*c*-*b*-*d*) that conserves the local parity[3] as well as the total S^z spin component which can be used to further block-diagonalize the Hamiltonian.

Let us first consider the subspace where at least both a and b or both c and d sites are parity even. Observe that every second site represents a spin singlet such that spin-flip processes on all bonds are prohibited. Hence, the Hamiltonian and all eigenvalues vanish.

Next, we discuss the cases where only the a or b as well as only the c or d site is single

[2] Note that γ_5 and P_α commute with each other such that they may be diagonalized simultaneously. However, γ_5 anti-commutes with R such that there is no basis which diagonalizes all three of them.

[3] Actually, the local number of particles is conserved. However, in the following it is more useful to distinguish the parity only as both empty and double-occupied sites constitute a spin-singlet which effectively removes that site from the ring.

occupied. Then, only one bond operator, say h_{ac}, is non-zero. From the spin conservation follows that the sectors with maximal value of $|S^z|$ have a vanishing Hamiltonian as the spin-flip operators cannot act on those states. The $S^z = 0$ subspace contains the two eigenstates $|\uparrow_a\downarrow_c\rangle \pm |\downarrow_a\uparrow_c\rangle$ with the according eigenvalues $\pm U$.

Third, we consider the subspace where exactly one parity is even, e.g., site b, such that $\mathcal{H}_+ = h_{ac} - h_{ad}$. Once more the states with maximal $|S^z| = 3/2$ are eigenstates of energy zero. In the $S^z = \pm 1/2$ subspace we find the Hamiltonian

$$H_{1/2} = U \begin{pmatrix} 0 & 1 & -1 \\ 1 & 0 & 0 \\ -1 & 0 & 0 \end{pmatrix}, \tag{5.10}$$

using the basis $\{|\downarrow_a\uparrow_c\uparrow_d\rangle, |\uparrow_a\downarrow_c\uparrow_d\rangle, |\uparrow_a\uparrow_c\downarrow_d\rangle\}$. Here the eigenvalues are given by $\pm\sqrt{2}U$ and zero.

The last and most interesting subspace has only odd parity sites. Like before, the two states with $S^z = 2$ are eigenstates with vanishing energy. In the $S^z = \pm 1$ sector we find eigenvalues of 0 and $\pm 2U$. The wave function of the $-2U$ state is

$$\phi_1 = 1/2\,(|\downarrow_a\uparrow_b\uparrow_c\uparrow_d\rangle - |\uparrow_a\downarrow_b\uparrow_c\uparrow_d\rangle - |\uparrow_a\uparrow_b\downarrow_c\uparrow_d\rangle + |\uparrow_a\uparrow_b\uparrow_c\downarrow_d\rangle)\,. \tag{5.11}$$

Finally, for $S^z = 0$ there are multiple states with vanishing energy, but only one state is associated with the eigenvalues $\pm 2\sqrt{2}U$, respectively, where the ground state wave function is

$$\begin{aligned} \phi_0 \;=\; & 1/2\Big(|\downarrow_a\downarrow_b\uparrow_c\uparrow_d\rangle + |\uparrow_a\uparrow_b\downarrow_c\downarrow_d\rangle \\ & + 1/\sqrt{2}[|\downarrow_a\uparrow_b\downarrow_c\uparrow_d\rangle - |\downarrow_a\uparrow_b\uparrow_c\downarrow_d\rangle - |\uparrow_a\downarrow_b\downarrow_c\uparrow_d\rangle + |\uparrow_a\downarrow_b\uparrow_c\downarrow_d\rangle]\Big)\,. \end{aligned} \tag{5.12}$$

In summary, the full spectrum of $\mathcal{H}_+$ consists of 186 states of vanishing energy, 16 states with energies $\pm U$ and $\pm\sqrt{2}U$ each, 2 modes for $\pm 2U$ and a unique state at energy $\pm 2\sqrt{2}U$.

It is also interesting to notice that lowest excitation has an energy of $\omega = 2(\sqrt{2}-1)U$ and changes the spin by $\Delta S^z = \pm 1$. It is straight forward to show that the lowest states ϕ_0 and ϕ_1 are related as $[(S_a^+ - S_b^+) - (S_c^+ - S_d^+)]\phi_0 \sim \phi_1$. Note that the b and d sites have negative γ_5 eigenvalues. This, combined with the second relative minus sign between (a,b) and (c,d) indicates the relation to the operator $M_{\mathbf{i}}^{\beta}$ defined in Eq. (5.5) which has already been identified as the most dangerous mean-field channel. Here, we learn that this operator also exhibits the lowest excitation of the strongly interacting limit.

We have shown that the block $\mathcal{H}_+$ exhibit a gaped and unique ground state, which is therefore also symmetric. The overall ground state of the full lattice model is then a product state that is also gapped, unique and respects all symmetries. Allowing finite, but small

values of t will change details of the ground-state wave-function. Especially it will no longer be a product state of purely local states. However, it will remain unique and symmetric until the hopping energy-scale set by t is comparable to the many-body gap. This is quite opposite to the regular Hubbard model on the two-dimensional square lattice where any finite value of t generates anti-ferromagnetic order.

To summarize, the limiting cases all exhibit unique ground states that share the same symmetries. As the strongly interacting state is a local product state, it is a representation of an atomic limit and very likely adiabatically connected to the trivial band insulators. The topological insulator is also stable against small interactions that where specifically chosen to allow a connection of the topological state to the strong interacting limit as the topologically protected defect states are symmetrically gapped [58]. However, especially for intermediate coupling strength along the path from the topological insulator to the Mott phase at strong interacting, the energy scales mix and spontaneous symmetry breaking might occur. The *dangerous* channel here is given by pseudo-magnetic order.

5.3. Method

Why should we go beyond mean field? The considerations of Sec. 5.2 allow two scenarios for intermediate coupling strength, both are in agreement with the theorems on non-interacting systems. Either the order parameters vanishes and the bulk gap closes at the topological phase transition, or, the non-zero order parameters ensures a finite bulk gap at the expense of a broken symmetry. However the interaction constructed following the rules of Ref. [58] aims at a different path, namely an adiabatic connection of two topological distinct phases. Such a setup has to keep the band gap finite while preserving all protecting symmetries. Hence this connection cannot be made on a mean-field level and requires an intermediate state without a quasi particle description. In other words, one replaces poles of the Greens function that cross the Fermi surface (band gap closing) by zeros (no spectral weight) in order to change the topological invariant.

To solve the interacting system, we use the ALF package [138], a general implementation of the auxiliary field Quantum Monte Carlo [110] method which is discussed in Sec. 2.3. The zero-temperature version of this algorithm provides access to ground-state properties by using a trial wave function $|\psi_T\rangle$, we take the non-interacting ground state, and project it to the correlated one by applying the exponentiated Hamiltonian $\exp(-\Theta\mathcal{H})|\psi_T\rangle$ [122, 123]. Here Θ controls the projection length, the result converges exponentially fast and we choose $\Theta = 20$ for the remainder of this work. The simulation of this model in the above formulation does not suffer a sign problem due to an anti-unitary symmetry which guarantees the positivity of each configurations weight.

Three observables are the main focus of this study. The first derivative of the free en-

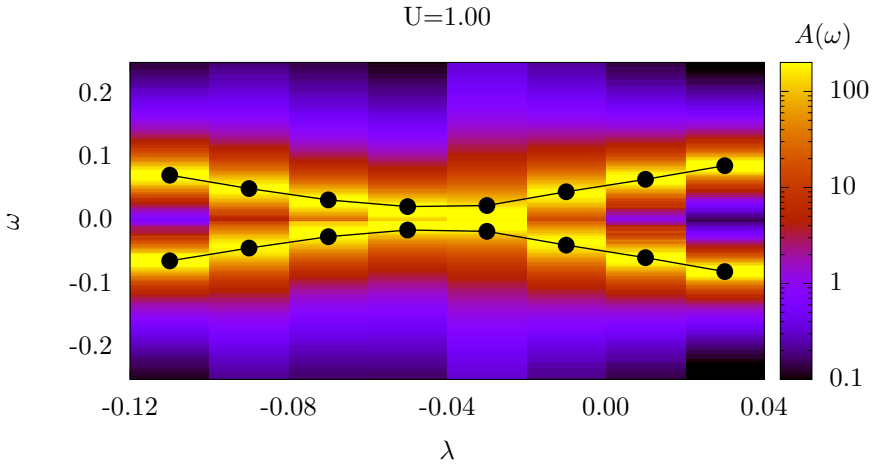

Figure 5.3.: Comparison of the single-particle spectrum $A(\omega)$ at the Dirac point $k = (\pi, \pi)$ extracted by analytic continuation using the stochastic maximum entropy method, with the band dispersion (solid black line) extracted from fitting the tail of time-displace Greens function. This proves that the assumption of a single low-energy excitation is justified.

ergy $\partial F/\partial U = -\beta/U\langle \mathcal{H}_{\text{int}}\rangle$ signals a first-order phase transition for increasing interaction strength U. To detect second-order phase transitions, we define a correlation ratio $r = 1 - \frac{S(\mathbf{q}=\delta\mathbf{q})}{S(\mathbf{q}=\mathbf{0})}$ where $S(\mathbf{q})$ is the correlation function in momentum space and $\delta\mathbf{q}$ the smallest but finite momentum available on the given lattice size. Observe that $\mathbf{q} = \mathbf{0}$ assumes a homogeneous instability which is justified according to the mean-field analysis. The correlation function is given as

$$S(\mathbf{q}) = \frac{1}{L^2}\sum_{\mathbf{i},\mathbf{j}} \exp[i\mathbf{q}(\mathbf{i}-\mathbf{j})] \sum_{\beta=x,y} \left\langle M^{\beta}_{\mathbf{i}} M^{\beta}_{\mathbf{j}} \right\rangle . \tag{5.13}$$

In case of long-range homogeneous order $S(\mathbf{0})$ diverges linear with system size L^2 whereas the correlation function remains finite for any other value of $\mathbf{q}$, hence $r = 1$ for the thermodynamic limit. In systems without long-range order, $S(\mathbf{q})$ is a smooth function such that r converges to zero for large lattices. As r is an RG-invariant quantity it exhibits a crossing point for different system sizes at the phase transition.

The third observable of interest is the single-particle gap that allows us to track the semimetallic Dirac cones that separate the insulators of different topology for $U = 0$. The single-particle greens functions are given by $G^{p}_{\mathbf{k}}(\tau) = \sum_o \langle \mathcal{T}\Psi_{\mathbf{k},o}(\tau)\gamma^0\Psi^{\dagger}_{-\mathbf{k},o}(0)\rangle$ for particle excitations and $G^{h}_{\mathbf{k}}(\tau) = -\sum_o \langle \mathcal{T}\Psi_{\mathbf{k},o}(0)\gamma^0\Psi^{\dagger}_{-\mathbf{k},o}(\tau)\rangle$ for hole excitations. If we assume a single quasi-particle mode at low energies gapped from higher energy excitations, then both greens function behave as $G_{\mathbf{k}}(\tau) \sim a_{\mathbf{k}} \exp(-\tau\varepsilon_{\mathbf{k}})$ for large values of τ where $\varepsilon_{\mathbf{k}}$ is the excitation energy and $a_{\mathbf{k}}$ its spectral weight. As a sanity check of this assumption, we compare the

extracted energies with the full spectrum (see Fig. 5.3) determined by MaxEnt [140] (see Sec. 2.4) which proves that the assumption is justified.

5.4. Results

We have shown above that the limit of strong interaction generates a gapped and symmetric ground state. Those two properties also apply to both non-interacting ground states, representing $-2 < \lambda < 0$ and $0 < \lambda$, such that the adiabatic connection seems to be plausible, at least in principle. To test this hypothesis, we will track the semi-metallic phase and analyze the most dangerous correlation function identified in the mean-field considerations.

Tracking the semi metal: Note that the two Hamiltonians with $\pm(\lambda+2)$ can be mapped onto each other. First, the mapping has to shift the momenta as $\mathbf{k} \to \mathbf{k}+(\pi,\pi)$ such that $m_{(\lambda+2)}(\mathbf{k}) = -m_{-(\lambda+2)}(\mathbf{k}+(\pi,\pi))$. To absorb the sign changes in the first three terms of Eq. (5.1b) the Dirac spinor has to transform as $\Psi_{\mathbf{k},o} \to \gamma_4 \Psi_{\mathbf{k},o}$. Therefore, the position of the semi-metal with two Dirac cones at $(\pi,0)$ and $(0,\pi)$ has to remain at fixed $\lambda = -2.0$ whereas the Dirac cone at (π,π) generically occurs at renormalized values $\lambda \sim 0$. It is interesting to notice that the γ_4 anti-commutes with R such that the winding $w \to -w$ is inverted and the two Hamiltonian represent opposite topologies.

One might also be concerned that the interaction might lead to a meandering of the Dirac cone within the Brillouin zone. If we had kept the PHS with $\Delta = 0$, then the cones are symmetry constraint to the time-reversal invariant momenta. On one hand, we fine-tuned the symmetry breaking such that the Dirac cones remain gapless in the free fermion system, and on the other hand, the numerical results show that the Dirac cone remain where they are.

Let us introduce $\lambda_c(U)$ as the critical value at which the semi-metal marks the topological phase transition between the TI with winding $w = +4$ and the trivial insulator. For the free fermion system, we have $\lambda_c(0) = 0$. To locate the phase transition, we set a fixed interaction strength, e.g., $U = 1.0$, and scan the single particle spectrum for various values of λ. The resulting excitation energies $\varepsilon_{(\pi,\pi)}$ of the Dirac cone are presented in Fig. 5.4(a). The results depend on the lattice size and a visual extrapolation suggests a semi-metal at $\lambda_c(1.0) = -0.04 \pm 0.02$. We repeat this analysis for various values of U and also confirm the symmetry constrained position $\lambda_c(U) = -2.0$ for the Dirac semi-metal with cones at $(0,\pi)$ and $(\pi,0)$ which separates the $w = +4$ TI from the one with winding $w = -4$ at $-4.0 \lesssim \lambda < -2.0$. The results are summarized in panel (c).

Symmetry-broken phase: Here, we focus on the intermediate region of the phase diagram where the energy scales of the correlation and the kinetic energy compete with each other. During the mean-field analysis (see Sec. 5.2), we have identified this regime between

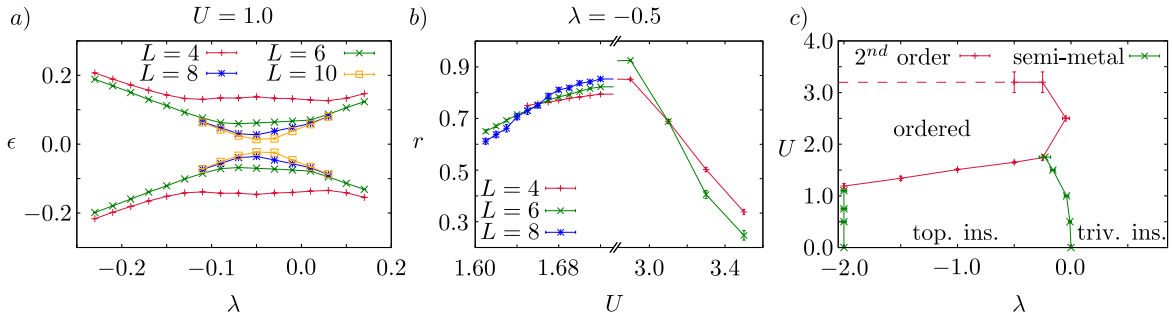

Figure 5.4.: On the left hand side, we present the extracted energies $\varepsilon_{\mathbf{k}=(\pi,\pi)}$ for the lowest particle/hole excitation. The system size scaling suggest a gap closing for $\lambda_c = -0.04 \pm 0.02$. In the central panel, the correlation ratio r is presented and the size scaling is consistent with a symmetry broken phase between $U_c = 1.65 \pm 0.02$ and $U_c = 3.2 \pm 0.2$. The right hand side summarizes various scans in the phase diagram.

the TI and the Mott insulator at strong interactions as the one most prone to spontaneous symmetry breaking with long-range pseudo-magnetic order.

Let us start with a fixed value of $\lambda = -0.5$ and analyze the correlation ratio r with increasing interaction strength U. The resulting data is depicted in Fig. 5.4(b) for various lattice sizes. We clearly see that the ratio systematically decreases with increasing L if the correlation strength is smaller than $U_c = 1.65 \pm 0.02$ or larger than $U_c = 3.2 \pm 0.2$ such that there is no long-range order here. In the intermediate region, the correlation ration increases with system size that indicates spontaneous symmetry breaking due to a finite pseudo-magnetic order in xy-plane of $M_{\mathbf{i}}^{\beta}$. The critical values stated above are extracted from the crossing point where the ratio coincides for all lattices. The second phase transition from the ordered phase to the Mott insulator requires larger interaction strength such that the QMC simulation become more challenging, hence the smaller lattice sizes and larger error estimate. Again, we repeat this calculation for various values of λ and summarize the phase boundary in panel (c).

Phase diagram: In panel (c), we plot the full phase diagram and confirm the expected stability of the Dirac semi metals as well as the insulators at weak coupling strength. The simulations also detect the symmetric state with strong correlation. In the middle of the phase diagram, where kinetic and potential energies are of similar order, we find long-range order in exactly the *dangerous* channel that we have identified in Sec. 5.2. This phase breaks the protecting R symmetry and therefore allows a hybridization of counter-propagating edge modes as shown in Fig. 5.2. As a result, we cannot find an adiabatic path between the two non-interaction topological insulators. Instead, any path in this phase diagram either contains a semi-metallic state or a symmetry-breaking phase.

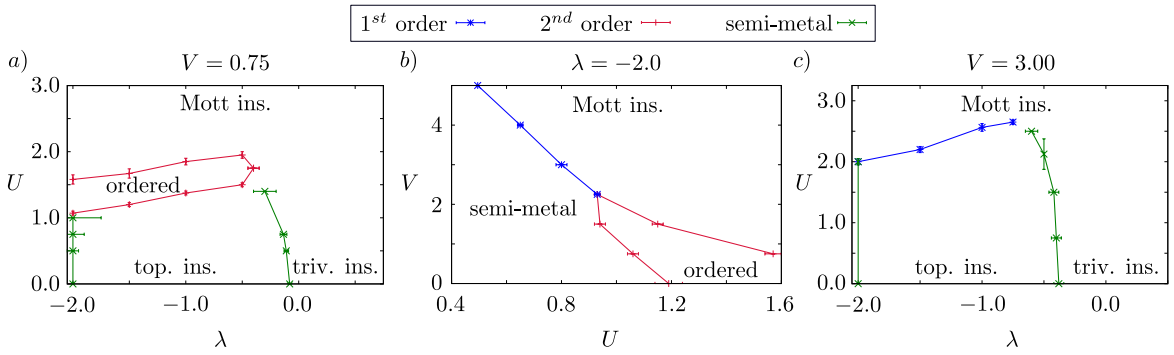

Figure 5.5.: The left hand side show the phase diagram for weak frustration $V = 0.75$ with a smaller region of long-range order compared to $V = 0$ that seems to be most stable for $\lambda = -2$. In the middle, we present the phase diagram for fixed $\lambda = -2.0$ for various frustration strength V. For $V > 2.5$, the symmetry broken phase is replaced by a first order phase transition. On the right hand side, the phase diagram is presented for high levels of frustration.

Can frustration remedy the problem: The main idea is to add the z-component of the pseudo-spins defined in Eq. (5.3) and use this to frustrate the in-plane order without changing the wave functions of the limiting cases. To form a proper $SU(2)$ algebra, we have to drop the γ_5 matrix acting on the Dirac components as $(\gamma_5)^2 = \mathbf{1}$ such that

$$S_{\mathbf{i}}^{1,\alpha,z} = (\Psi_{\mathbf{i},A}^{\dagger}\Psi_{\mathbf{i},B}^{\dagger})s^z \otimes P_\alpha(\Psi_{\mathbf{i},A}, \Psi_{\mathbf{i},B})^T \tag{5.14a}$$

$$S_{\mathbf{i}}^{2,\alpha,z} = (\Psi_{\mathbf{i},C}^{\dagger}\Psi_{\mathbf{i},D}^{\dagger})s^z \otimes P_\alpha(\Psi_{\mathbf{i},C}, \Psi_{\mathbf{i},D})^T . \tag{5.14b}$$

Observe that this z-component generates rotations within the xy-plane of the pseudo-spins that leave the Hamiltonian invariant. Additionally, the transformation $(A \leftrightarrow B)$ combined with $(C \leftrightarrow D)$ also is a symmetry operation under which $S_{\mathbf{i}}^{1/2,\alpha,z} \to -S_{\mathbf{i}}^{1/2,\alpha,z}$ is inverted. Hence, any unique ground state has to be an eigenstate of $\sum_{\mathbf{i},\alpha=\pm}\left(S_{\mathbf{i}}^{1,\alpha,z} + S_{\mathbf{i}}^{2,\alpha,z}\right)$ with a vanishing expectation value. In the large U limit, the sites and α-subblocks decouple such that we introduce an additional interaction term $\mathcal{H}_{\text{frust}} = V\sum_{\mathbf{i},\alpha=\pm}\left(S_{\mathbf{i}}^{1,\alpha,z} + S_{\mathbf{i}}^{2,\alpha,z}\right)^2$ which minimizes S^z locally without changing the ground state.

As depicted in Fig. 5.5, weak frustration does reduce the size of the symmetry broken phase. In panel (a), we present the phase diagram for $V = 0.75$. The symmetry broken phase now extends only to $\lambda \sim 0.5$ whereas in the unfrustrated model it reaches $\lambda \sim 0$. Additionally, we find that the long-range ordered region is shifted towards weaker coupling strength U while also the range in U has been reduced. This trend is also clearly visible in panel (b) where we kept $\lambda = -2.0$ fixed. The Dirac cones at $(\pi, 0)$ and $(0, \pi)$ persist for weak coupling strength U and V. Increasing U generates the long-ranged ordered state before at large U the symmetric Mott insulator appears. With higher level of frustration the symmetry broken phase is replaced by a direct first order phase transition between the Dirac

semi-metal and the Mott insulator. In Fig. 5.5(c), we show that the first order phase transition extends also to $\lambda > -2.0$ and connects to other semi metal of the (π, π) Dirac cone.

5.5. Discussion

In the framework of this study there is no adiabatic path between topological ($w = 4$) and trivial ($w = 0$) insulators. The semi-metal separating the non-interacting insulators persist for small coupling strength in U and is terminated by either a second-order phase transition to a long-range ordered phase or by a first order transition to a symmetric Mott insulator related to the large U limit. Also the topological insulator either undergoes a symmetry breaking second order or a first-order phase transition.

As we did not and can not test all possible interaction terms with the according paths, this does not disprove the reduction from $\mathbb{Z}$ to $\mathbb{Z}_4$. Instead, our results show that the conditions on the form of the interaction presented so far may very well be necessary, but they do not seem to be sufficient. One popular line of argument for the reduction focuses on the topologically protected boundary states and designs interaction terms to gap out the boundary modes symmetrically. Often this reduces the problem to purely local defects, e.g. the boundary of one-dimensional Kitaev chains is zero-dimensional as well as the dimensional reduction scheme, that also generates local defects which inherit the topology of the full bulk system by the according number of modes. However, this decreased dimensionality does have strong implications on the possibility of spontaneous symmetry breaking in the ground state that may only occur in one (two) or higher dimensions for discrete (continuous) symmetries according to Mermin-Wagner theorem [3]. And it is exactly this mechanism which blocks the path we were looking for.

From the two-dimensional bulk perspective, the phase diagram exhibits various critical points. Even though the focus of this study was to establish the phases themselves, it is interesting to discuss those critical theories briefly. There are Wilson-Fisher transitions between the topological insulator and the ordered phase as well as between the ordered phase and the Mott insulator. Additionally, we expect the critical point where the semi-metal is gapped by symmetry breaking to be described by a Gross-Neveu theory [207, 208].

The results of this work raise a few questions, mainly focused on the missing pieces required to find the adiabatic path. In Fig. 5.6, we sketch two alternative scenarios for the bulk phase diagram, (a) the symmetric mass generation for the Dirac cone as well as (b) a separated region of symmetry breaking that terminates the semi-metal line. Several studies have reported the formation of a correlated single-particle gap of $SU(4)$-symmetric Dirac system without the generation of long-range order [209, 210]. Most surprisingly, it is claimed to be a second order transition. In Ref. [211], the authors propose a theory that involves fractionalization in order to explain this exotic phase transition. It would be very promising to include

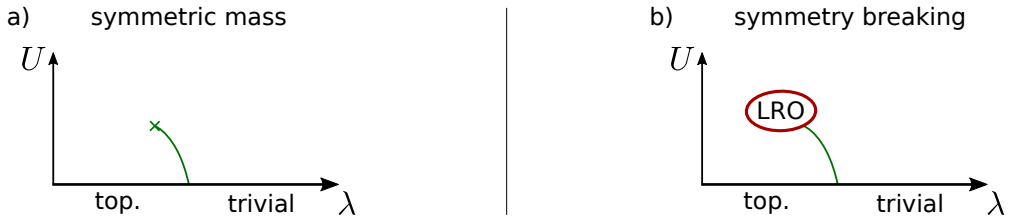

Figure 5.6.: There exist at least two alternative bulk scenarios with (a) symmetric mass generation (green cross) or (b) a symmetry breaking region (red circle) with long-range order (LRO) terminating the semi-metal between topologically distinct non-interacting states. Observe that the region with LRO connects to only one semi-metal and not two both as in our numerical phase diagram in Fig. 5.4(c). Both scenarios allow an adiabatic path and are not realized in the range of parameters investigated in this study.

the same kind of bulk criticality in our setup in order to find the adiabatic connection and then investigate the details of how this affects the topological aspects.

In contrast, the scenario (b) shows that this symmetric mass generation is not required and that there also exist more conventional options in which the symmetry broken region we find is split into two separate ones. However, there is no obvious approach to engineer this phase diagram. One avenue again involves the bulk boundary correspondence and attempts to fine-tune bulk parameter [212] such that the energy scales respect the following hierarchy. The interaction strength should be smaller than the bulk gap $U/t < \Delta_{\text{bulk}}/t$ but still large enough to gap the edge modes $U/v_{\text{edge}} > U^c_{\text{edge}}/v_{\text{edge}}$ where v_{edge} is the Fermi velocity of the edge mode and U^c_{edge} the critical interaction strength.

As many studies make use of the bulk-boundary correspondence, it would also be interesting to test this hypothesis by itself. To this end, one could study the properties of the edge state in the region of the phase diagram that is adiabatically connected to the non-interacting topological states. Does there exist a region, probably at rather strong interactions right before the bulk system undergoes the phase transition, where the edge spectrum is already gapped out? In this case, there are at least two scenarios, (i) the edge state mass originates from spontaneous symmetry breaking [213] as discussed in Ch. 3 or (ii) the edge is symmetrically gapped and topologically trivial. Whereas the former is consistent with the bulk-boundary correspondence, the latter option may constitute a violation of the hypothesis.

CHAPTER 6

Fractional Fermi liquid in a frustrated Kondo lattice model

Thus far, we have been focusing on symmetry protected topological phases and their stability with respect to interactions in Ch. 3 and Ch. 5. In Ch. 4, we have presented an attempt to generate a quantum anomalous Hall state dynamically. In two dimensions, however, there also exists the possibility of topological order which constitutes a distinct state of matter from the scenarios above. Most importantly, this phase does not require a protecting symmetry and is instead characterized by topological ground-state degeneracy. Celebrated examples include electrons in fractional quantum Hall states [65, 66] and – more relevant for this project – quantum spin liquids [68–71] formed by local moments.

This raises the question: What happens if those moments are coupled to extended conduction electrons (c) via Kondo interaction of amplitude J_K? In case of a single magnetic spin-$1/2$ impurity coupled to a metallic environment with time-reversal symmetry, the interaction is relevant and introduces a Kondo cloud of electrons at low temperatures that screen the local moment collectively [93, 102]. In case of multiple local moments on a lattice, this picture breaks down and the problem is much harder to solve. In this lattice setup, the Kondo coupling of conduction electrons with the local moments induces two competing energy scales: the Kondo screening and the indirect Ruderman-Kittel-Kasuya-Yoshida (RKKY) exchange interaction [95–97]. In this domain, possible states are constrained by the Lieb-Schultz-Mattis-Hastings-Oshikawa theorem [79, 80, 106]. In the absence of magnetic order there are at least two possible scenarios: (1) the formation of a heavy Fermi liquid where the local moments contribute to the Fermi volume and thus generates a 'large' Fermi surface of 'heavy' quasiparticles. The Kondo insulator is a special version of this scenario when the 'large' Fermi surface vanishes, e.g. for single-orbital conduction electrons at half filling coupled to one local moment per unit cell. A distinct possibility (2) are local moments that decou-

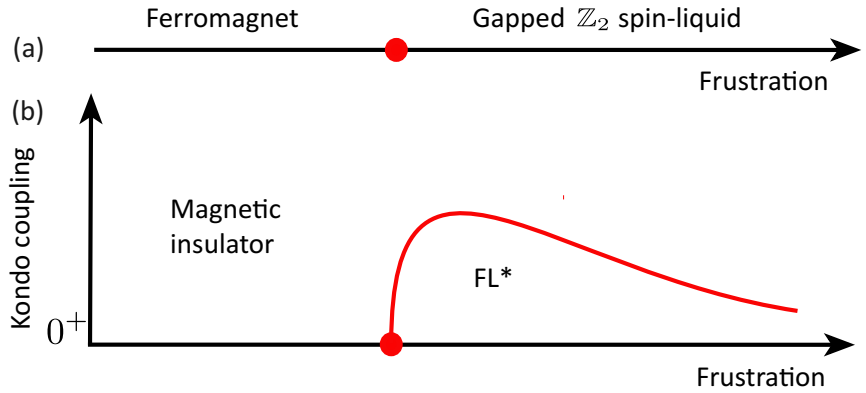

Figure 6.1.: (a) Schematic phase diagram of the BFG model in the absence of Kondo coupling. (b) Schematic phase diagram of the BFG model in the presence of Kondo coupling. The stability of the 'FL*'phase is is set by the gap in the BFG model scales as $(J^{\perp})^2/J^z$ in the strong coupling limit.

ple from the conduction electrons at low energies and form a spin-liquid phase [107, 214]. Here, the spin degrees of freedom no longer contribute to the Fermi volume and therefore the 'small' Fermi surface is restored in the sense that its size is given by the conduction electrons alone. This scenario constitutes a violation of Luttinger's theorem [105] and is also known as a 'fractional Fermi liquid' phase ('FL*' phase), first introduced in Refs. [107, 214].

The transition from the 'large' to the 'small' Fermi surface is often referred to as Kondo breakdown and poses a challenging issue in experiments on heavy fermion materials [103, 107, 215]. In one realization, the Kondo breakdown coincides with the transition between a heavy Fermi liquid and a magnetically ordered phase without screening as it has been observed in $YbRh_2Si_2$ [216] and $CeCu_{6-x}Au_x$ [217]. A different, and more related, case is seen in Co and Ir doped $YbRh_2Si_2$ [218] where transitions of a heavy Fermi liquid or an anti-ferromagnet to a *non-magnetic phase* without Kondo screening are reported. The latter is an exotic phase, inconsistent with a Fermi liquid as the ground state, if the unit cell contains an odd number of spin-1/2 degrees of freedom in the absence of other symmetry breaking, e.g., lattice translations [106, 107, 214]. In this scenario, the local moments either have to be topologically ordered or exhibit a gapless spectrum [80]. We also note that the Kondo breakdown is closely related to the concept of 'orbital selective Mott transition' as discussed in Ref. [219]. Our work might also be relevant for several other heavy fermion materials that show a poorly understood phenomenology such as CePdAl [220–223], κ-$(ET)_4Hg_{2.89}Br_8$ [224], YbAgGe [225], $YbAl_3C_3$ [226] and Yb_2Pt_2Pb [227]. Microscopic descriptions of these systems have indicated that frustration plays an important role here.

In this study, we report the first numerical realization of a fractional Fermi liquid as well as a phase transition to a magnetically ordered phase that exhibits finite Kondo screening. From a technical point of view, we were able to simulate frustrated local moments Kondo coupled

to conduction electrons without suffering the infamous negative-sign problem [228]. The model essentially consists of two building blocks, (1) local moments described by a variant of the Balents-Fisher-Girvin (BFG) model [81–83], first introduced in Ref. [84], and (2) conduction electrons on the honeycomb lattice hosting a Dirac semi-metal at half-filling. The BFG model supports a magnetically ordered state and a transition to a gapped $\mathbb{Z}_2$ spin-liquid upon increasing the frustration as sketched in Fig. 6.1(a). At finite, but weak Kondo coupling and large frustration, the spin-liquid is gapped and the semi-metal has a vanishing density of states at the Fermi level, such that both states are expected to persist. However, this phase violates Luttinger's sum rule as a metallic state should exhibit a 'large' Fermi surface covering half of the Brillouin zone[1]. At larger values of Kondo coupling, the energy scale set by the interaction exceeds the gap of the BFG model such that the topological order is destroyed. Thus, the system enters a conventional phase with electron-like quasiparticles. We test these hypothesis by studying the spectral function of conduction electrons as well as investigating the mutual information that quantifies the amount of entanglement between conduction electrons and local moments to shed light on the formation of Kondo singlets.

This work has been performed under the supervision of F. F. Assaad and T. Grover and is published as Ref. [P2].

6.1. Model

We investigate the following generalized Kondo lattice model (KLM) described by $\mathcal{H} = \mathcal{H}_c + \mathcal{H}_S + \mathcal{H}_K$ with

$$\begin{aligned} \mathcal{H}_c &= -t \sum_{\langle \boldsymbol{x},\boldsymbol{y}\rangle,\sigma} c^\dagger_{\boldsymbol{x},\sigma} c_{\boldsymbol{y},\sigma} + h.c. \\ \mathcal{H}_{\mathrm{S}} &= -J^\perp \sum_{\langle \boldsymbol{i},\boldsymbol{j}\rangle} \left(S^{f,+}_{\boldsymbol{i}} S^{f,-}_{\boldsymbol{j}} + h.c. \right) + J^z \sum_{\hexagon} \left(S^{f,z}_{\hexagon} \right)^2 \\ \mathcal{H}_K &= J_K \sum_{\langle \boldsymbol{x},\boldsymbol{i}\rangle} \left[S^{c,z}_{\boldsymbol{x}} S^{f,z}_{\boldsymbol{i}} - (-1)^{\boldsymbol{x}} \left(S^{c,+}_{\boldsymbol{x}} S^{f,-}_{\boldsymbol{i}} + h.c. \right) \right]. \end{aligned} \tag{6.1}$$

Here, $c^\dagger_{\boldsymbol{x},\sigma}$ creates a conduction electron of spin σ in a Wannier state centered at position $\boldsymbol{x}$. They are subject to hopping processes along nearest neighbors of a honeycomb lattice, labeled as $\langle \boldsymbol{x},\boldsymbol{y}\rangle$. The spin operator of the conduction electrons is $\boldsymbol{S}^c_{\boldsymbol{x}} = \frac{1}{2}\sum_{s,s'} c^\dagger_{\boldsymbol{x},s} \boldsymbol{\sigma}_{s,s'} c_{\boldsymbol{x},s'}$. The local moments (spin-1/2) are described by $\boldsymbol{S}^f_{\boldsymbol{i}}$ located on the kagome lattice, which corresponds to the median of the honeycomb lattice (see Fig.6.2). The Hamiltonian $\mathcal{H}_S$ is a variant of the BFG model (Ref. [81, 84]) containing spin flip processes of amplitude $J^\perp$

[1] Observe that the half-filled honeycomb lattice, which has to orbitals per unit cell, exhibits a vanishing Fermi volume with a Fermi surface of two single points. Adding 3 spin-1/2 degrees of freedom per unit cell amounts occupy an additional half of the Brillouin zone, omitting complete filled bands.

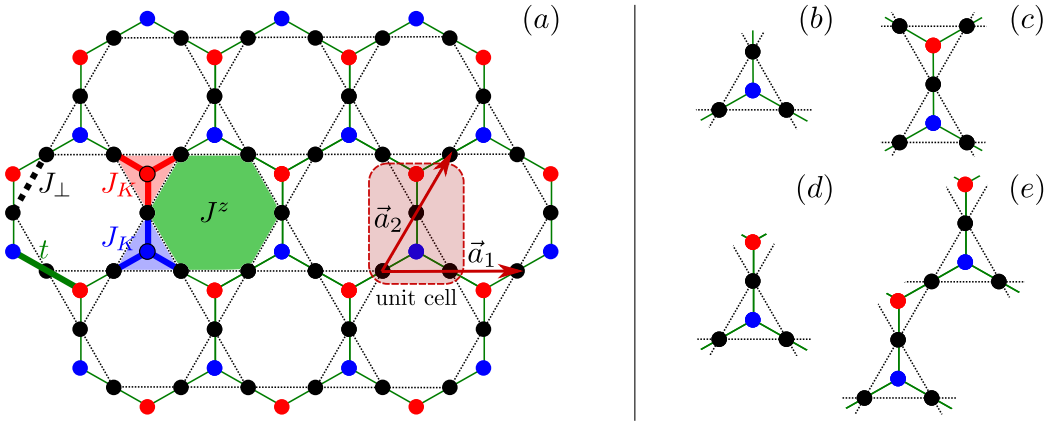

Figure 6.2.: *Left:* The model - The conduction (c-) electrons hop, with matrix element t, between nearest neighbor sites of the honeycomb lattice denoted by the red and blue circles. The kagome lattice (black) supports impurity spins described by the Balents-Fisher-Girvin model with nearest neighbor spin-flip $J^\perp$ and interactions on hexagons of strength J^z (green). The two systems are Kondo-coupled with strength J_K for each bond in the elemental triangles (thick red and blue bonds). For details see Eq. (6.1). *Right:* Various patches Γ used to extract the Renyi mutual information. Subsets (b) and (c) belong to the triangle sequence, (d) and (e) are built out of unit cells.

on nearest neighbor bonds, indexed by $\langle \boldsymbol{i},\boldsymbol{j}\rangle$. The interaction of strength J^z minimizes the total z-component of spin on a hexagon $S^{f,z}_{\hexagon} = \sum_{\boldsymbol{i}\in\hexagon} S^{f,z}_{\boldsymbol{i}}$. Finally, the conduction electrons and the local moments are Kondo coupled, according to $\mathcal{H}_K$, along nearest neighbor bonds $\langle \boldsymbol{x},\boldsymbol{i}\rangle$ between the kagome and honeycomb lattices (Fig. 6.2). The factor $(-1)^{\boldsymbol{x}}$, which takes the value 1 (-1) on the A (B) sublattice of the honeycomb lattice, is necessary to avoid the negative sign problem. In particular it cannot be gauged away since the kagome lattice is not bipartite. In relation to Fig.6.1, J^z plays the role of frustration, and J_K is the Kondo coupling. Due to the energy gap of the spin liquid and the associated stability of the phase, the sign structure of the Kondo interaction is not relevant for the 'fractional' Fermi liquid phase. It does however influence the possibility of non-magnetic 'heavy' fermion phases.

6.1.1. Symmetries & heavy fermi liquids

In this section, we consider possible non-magnetic mean-field scenarios in the context of our model such as the Kondo insulator and the heavy Fermi liquid phase which are often realized in conventional Kondo lattice systems. To this end, it is convenient to introduce the following two operators $\Delta^0_{\boldsymbol{x},\boldsymbol{i}} = \sum_s c^\dagger_{\boldsymbol{x},s} f_{\boldsymbol{i},s} + h.c.$ and $\Delta^z_{\boldsymbol{x},\boldsymbol{i}} = c^\dagger_{\boldsymbol{x},\uparrow} f_{\boldsymbol{i},\uparrow} - (-1)^{\boldsymbol{x}} c^\dagger_{\boldsymbol{x},\downarrow} f_{\boldsymbol{i},\downarrow} + h.c.$ so that the Kondo coupling of Eq. (6.1) can be written as $\mathcal{H}_K = -\frac{J_K}{4}\sum_{\langle \boldsymbol{x},\boldsymbol{i}\rangle}(\Delta^z_{\boldsymbol{x},\boldsymbol{i}})^2$. Whereas the former usually generates the Kondo insulator in conventional Kondo lattice systems at half filling as well as the heavy Fermi liquid at finite doping [103, 104], the later is more natural in the model defined by Eq. (6.1) due to the sign structure of the Kondo coupling. In the

U	σ^x	σ^z	σ^0	σ^0
α	$-$	$-$	$+$	$-$
β_x	$-$	$+$	$-$	$-$
β_y	$+$	$+$	$+$	$-$
β_z	$+$	$-$	$-$	$-$

Table 6.1.: Table of independent particle-hole symmetries. See the Sec. 6.1.1 for the notation.

following, we first describe the symmetries of the model and then discuss their implications for non-magnetic mean-field approximations.

Our system, defined by Eq. (6.1), has several continuous and discrete symmetries. There exist two distinct $U(1)$ symmetries. First, the total number of conduction electrons is conserved. Second, the Hamiltonian is invariant under spin rotations aroung the z-axis, generated by $\sum_{\boldsymbol{x}} S^{c,z}_{\boldsymbol{x}} + \sum_{\boldsymbol{i}} S^{f,z}_{\boldsymbol{i}}$ such that the total S^z-component is also conserved. Additionally, the system exhibits several discrete, unitary and anti-unitary particle-hole symmetries that are listed in Table 6.1. They are implemented with the help of a unitary matrix U, acting as $c^\dagger_{\boldsymbol{x},s} \to (-1)^{\boldsymbol{x}} U_{s,s'} c_{\boldsymbol{x},s'}$ and $f^\dagger_{\boldsymbol{i},s} \to U_{s,s'} f_{\boldsymbol{i},s'}$. The transformation may ($\alpha = -1$) or may not ($\alpha = +1$) include a complex conjugation acting as $\sqrt{-1} \to \alpha\sqrt{-1}$ such that the sign α distinguishes between unitary and anti-unitary transformations. We characterize their action on the spin operators using the sign-tuple $\boldsymbol{\beta} = (\beta_x, \beta_y, \beta_z)$ that specifies the transformation of both $S^{c,l}_{\boldsymbol{x}} \to \beta_l S^{c,l}_{\boldsymbol{x}}$ and $S^{f,l}_{\boldsymbol{i}} \to \beta_l S^{c,l}_{\boldsymbol{i}}$.

At the level of free fermion band-structure, the particle-hole symmetries listed above guarantee the existence of flat bands. In particular, either of the symmetries $(U, \alpha) = (\sigma^0, -)$ and $(U, \alpha) = (\sigma^z, -)$ guarantee that there is a flat band. This is because these transformations do not mix up and down spin components, which leads to an odd number (=five) of bands for each spin sector. Furthermore, the anti-unitary nature of the symmetry implies that $c(k) \to c^\dagger(k)$. Thus there always exists a flat band at zero energy in each spin sector. Such a flat band will generically be unstable with respect to interactions. For example, a magnetically ordered state in the z-direction will break both of these particle-hole symmetries, according to Table 6.1.

A natural mean-field approximation uses the hybridization term $\Delta^z = \sum_{\langle \boldsymbol{x},\boldsymbol{i} \rangle} \Delta^z_{\boldsymbol{x},\boldsymbol{i}}$ which preserves the particle-hole symmetry listed as (σ^x, -) in Table 6.1, but breaks $(\sigma^z, -), (\sigma^0, +)$ and $(\sigma^0, -)$, as well as TR_1 and TR_2. The mean-field Hamiltonian $\mathcal{H}_c + \Delta^z$ still has a spin-degenerate flat band at the chemical potential. However, this band is not protected by symmetries. For example, a magnetization in the z-direction, which respects the remaining S^z-spin-rotation as well as the particle-hole symmetry with $(\sigma^x, -)$, can induce a single-particle gap should therefore be included as well. This generates a magnetically order state and numerically we do not find any evidence for a finite magnetization in the z-direction.

Let us next consider mean-field solutions based on symmetry arguments. As discussed

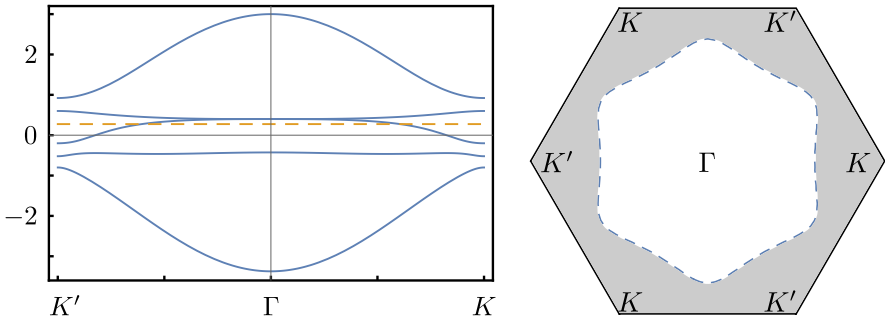

Figure 6.3.: Cut of the spectrum from K' to K with the Fermi energy marked by the dashed, orange line constraint to the half filled case and Fermi surface (blue, dashed) of a heavy Fermi Liquid state with $\Delta = 0.4$ and $t' = 0.2$. The shaded area marks the occupied part of the BZ.

before, to obtain dispersive bands requires the breaking of at least some symmetries. One option is the uniform hybridization, $\sum_{\langle \boldsymbol{x},\boldsymbol{i}\rangle} \Delta^0_{\boldsymbol{x},\boldsymbol{i}}$, that preserves the time reversal symmetries TR_1 and TR_2, but violates all particle-hole symmetries. As a consequence, direct f-electron hopping terms given by $\sum_{\langle \boldsymbol{i},\boldsymbol{j}\rangle,s} f^\dagger_{\boldsymbol{i},s} f_{\boldsymbol{j},s} + h.c.$, are no longer excluded by symmetry and should then also be taken into account. The mean-field Hamiltonian for such a heavy Fermi Liquid is defined by

$$\mathcal{H}_{\text{hFL}} = \mathcal{H}_c + \Delta \sum_{\langle \boldsymbol{x},\boldsymbol{i}\rangle} \Delta^0_{\boldsymbol{x},\boldsymbol{i}} + t' \sum_{\langle \boldsymbol{i},\boldsymbol{j}\rangle,s} f^\dagger_{\boldsymbol{i},s} f_{\boldsymbol{j},s} + h.c.. \tag{6.2}$$

The resulting band-structure is shown in Fig. 6.3 where we have used the (arbitrary) parameters $\Delta = 0.4$ and $t' = 0.2$. The left hand side depicts a cut from K' to Γ to K and we clearly recognize a dispersive band in the middle of the spectrum replacing the aforementioned flat band at zero energy. Each band is spin degenerate which enhances the S_z symmetry to a full $SU(2)$ and consequently, the state is paramagnetic. The right hand side presents the required Fermi surface (blue, dashed) in order to keep the electron density fixed at half-filling. Consistent with Oshikawa's argument [106], we find a 'large' Fermi surface that encloses half of the Brillouin zone as depicted by the shaded area in Fig.6.3. The effective chemical potential required for half filling is marked by the dashed orange line in the left panel.

To summarize, the natural mean-field decoupling of Eq. (6.1) leads to a magnetic phase and a symmetry-based approach generates a heavy Fermi liquid that we do not find numerically in the investigated range of parameters. Additional AFM scenarios will be discussed in the following section on limiting cases.

6.1.2. limiting cases

Let us consider various limiting cases of the Hamiltonian $\mathcal{H}$, already sketched in Fig. 6.1, and start with the limit $J^\perp \gg J^z, J_K$ and arbitrary values of t, representing the region around

the origin of the sketch. Here, the ground state of the pure BFG model is ferromagnetically ordered in the XY plane [84]. Owing to the sign structure $(-1)^{\boldsymbol{x}}$ of the Kondo interaction, this induces an anti-ferromagnetic in-plane order of the conduction electrons. Thus the Dirac cones exhibit a single-particle gap such that the full system forms a magnetic insulator.

Next, let us discuss the limit $J_K \gg J^\perp \gtrsim J^z, t$ and first set all parameters but J_K to zero. Here the transformation $c_{\boldsymbol{x},\downarrow} \to -(-1)^{\boldsymbol{x}} c_{x,\downarrow}$ maps the Kondo interaction onto an anti-ferromagnetic Heisenberg model. The Kagome and the honeycomb lattices constitute a bipartition such that the interaction is not frustrated. This leads to a ground state with AFM order where the local moments and the conduction electron have opposite polarization. Reverting above transformation flips the in-plane components for the odd honeycomb sublattice. Now let us switch on $J^\perp, J^z$ with $J^\perp \gtrsim J^z$ such that the in-plane polarization is more favorable that those with finite z-components as the latter is breaking the additional symmetry $S^{f,z}_{\boldsymbol{i}} \to -S^{f,z}_{\boldsymbol{i}}, S^{f,x}_{\boldsymbol{i}} \to S^{f,x}_{\boldsymbol{i}}, S^{f,y}_{\boldsymbol{i}} \to S^{f,y}_{\boldsymbol{i}}$. Observe that the XY spin texture is identical to the limit discussed in the previous paragraph. Hence, we expect an adiabatic connection between the two limits without another phase transition in-between. Also this phase is stable with respect to finite values of t due to the stiffness associated with symmetry breaking.

The most interesting limit is $J^z \gg J^\perp \gg J_K$. Let us begin with the parameter set where only J^z and t are finite while every other one vanishes. Here the conduction electrons form a Dirac semi-metal at half filling and the ground state of the (classical) spins is highly degenerate which diverges exponentially with system size [81]. Finite values for $J^\perp/J^z \ll 1$ introduce quantum fluctuations that lift the classical degeneracy and the local moments form a gapped $\mathbb{Z}_2$ spin-liquid with topological order [81]. It is remarkable to notice that small values of Kondo coupling do not change this phase considerably as it is discussed in Refs. [107, 214]. From a renormalization group perspective this stems from the irrelevance of the Kondo coupling at the fixed point of a Dirac semi-metal and a gapped $\mathbb{Z}_2$ spin liquid, based on weak-coupling perturbative arguments. Hence, the conduction electrons and local moments decouple at low energies and form a fractional non-Fermi liquid 'FL*' phase with a 'small' Fermi surface as introduced in Refs. [107, 214]. Physically, in this phase the local moments are highly entangled with each other such that the formation of Kondo singlets or the tendency to magnetic order is suppressed.

To appreciate the exotic nature of the 'FL*' phase, it should be compared to conventional heavy Fermi liquids that satisfy the Luttinger sum rule [107, 108]:

(i) In a 'heavy' Fermi liquid, the Fermi volume is given by $\mathcal{V}_{\mathrm{hFL}} = K(n_{tot} \bmod 2)$ where $n_{tot} = n_c + n_f$ is the total number of conduction and f-electrons per unit cell and $K = (2\pi)^2/(2v_0)$ is the phase space factor for a unit cell of size v_0. In contrast, the local moments do not contribute to the Fermi volume $\mathcal{V}_{\mathrm{FL}^*} = K(n_c \bmod 2)$ in the 'FL*' phase. Here, we have two electrons from the two orbital honeycomb lattice (semi-metal with completely filled bands apart from the Dirac points) and three spin-1/2

degrees of freedom per unit cell. Hence, Kondo screening induces a 'large' Fermi surface $\mathcal{V}_{\mathrm{hFL}} = K$ that encloses half of the Brillouin zone whereas the Fermi volume of the fractional Fermi liquid vanishes $\mathcal{V}_{\mathrm{FL}^*} = 0$.

(ii) In addition to conventional electronic quasiparticle, the 'FL*' phase also exhibits non-local emergent vison excitations that stem from the topological degeneracy of the spin-liquid ground states. In Ref. [106, 107], it is argued that these excitation allow the formation of a 'small' Fermi surface of volume $\mathcal{V}_{\mathrm{FL}^*}$.

Previously, we discussed several mean-field ansätze and showed that the nature of possible Fermi liquid states strongly depend on symmetries. When the $SU(2)$ spin rotation as well as the particle-hole symmetry is preserved then there has to exist a spin-degenerate flat band pinned at the Fermi level. Such a state is inherently unstable as discussed in Sec. 3 and Refs. [33,35,44,45,127,142,173,187,213]. We also found essentially two ways to introduce Kondo screening via hybridization of c- and f-electrons that either break PHS – in case of uniform hybridization – or TRS – when the sign structure $(-1)^{\boldsymbol{x}}$ of the Kondo coupling is incorporated. The latter term requires fine-tuning in order to remain paramagnetic whereas the former naturally generates a non-magnetic heavy Fermi liquid. However, in the range of parameters studied here, we do not find such phases. It is interesting to notice that the TRS breaking hybridization does not violate any additional symmetry of the magnetic phase. Hence it should be relevant especially for large J_K and might be one source of entanglement between c- and f-electrons.

6.2. Method & observables

We investigate the Hamiltonian defined in Eq. (6.1) using the auxiliary field quantum Monte Carlo method [110, 121, 229]. The pure BFG model has been solved using the bosonic stochastic series expansion without suffering from the negative-sign problem given that $J^{\perp} \geq 0$ renders the coupling ferromagnetic [84]. The conduction electron subsystem is amendable to the fermionic BSS algorithm. In Ref. [228] the authors show that it is then possible to introduce a Kondo coupling in the form of $\mathcal{H}_K$ between the spin model and the particle-hole symmetric conduction fermions without generating a negative-sign problem. In order to apply the fermionic auxiliary field method, we fermionize the local moments by introducing f-electrons that are subject to the constraint of single-occupied sites $\sum_s f^{\dagger}_{\boldsymbol{i},s} f_{\boldsymbol{i},s} = 1$. The local moments are then given by $\boldsymbol{S}^f_{\boldsymbol{i}} = \frac{1}{2}\sum_{s,s'} f^{\dagger}_{\boldsymbol{i},s} \boldsymbol{\sigma}_{s,s'} f_{\boldsymbol{i},s'}$. Similar to simulations of generic Kondo lattice models [101, 230] this condition corresponds to a local conservation law. Hence, it can be imposed very efficiently with the help of an intrinsic Hubbard interaction. We have used the ALF package [138] to carry out the numerical investigation and some more details of our implementation are outlined in the following section 6.2.1.

Despite the absence of sign problem, the simulations of this model are challenging. On one hand, the fermionization leads to a large number of auxiliary fields, 33 per unit cell, and, on the other hand, the efficient projection onto single-occupied f-electron sites with an effective Hubbard interaction of strength $U = J^{\perp} + 4J^{z}$ generates comparatively large scales in $\mathrm{e}^{-\Delta\tau\mathcal{H}}$. This renders the simulation relatively prone to numerical instabilities. As a consequence, we have used a small imaginary time step $\Delta\tau t = 0.01$. In addition to the stability issues, this model also generates exponentially large scales in $\mathrm{e}^{-\beta\mathcal{H}}$ that lay beyond the range of double precision variables. To overcome this issue, we introduced the logarithmic stabilization scheme as discussed in Sec. 2.3.

The biggest challenge turns out to be the long autocorrelation times. We tried to improve this issue by using global moves that mimic the ring-exchange processes related to vison excitations, as well as by implementing parallel tempering schemes. Nevertheless, these long autocorrelation times remain the limiting factor to access system sizes bigger than those presented here, in particular 3×3 and 6×3 unit cells. For both lattices sizes, and the considered periodic boundary conditions, Dirac points are present. However, only the 6×3 allows to simultaneously satisfy $S^{f,z}_{\hexagon} = 0$ in all hexagons. Observe that our model contains 2 spin-full fermionic and 3 spin-1/2 degrees of freedom per unit cell such that the many-body Fock-space is 2^{63} and 2^{126} dimensional and therefore well beyond the capabilities of state-of-the-art exact diagonalization algorithms that may reach cluster sizes of up to 48 spins [231].

We compute spin-spin correlations $S_{AFM} = 1/L \sum_{\boldsymbol{IJ}} \langle S^x_{\boldsymbol{I}} S^x_{\boldsymbol{J}} + S^y_{\boldsymbol{I}} S^y_{\boldsymbol{J}} \rangle$ where the net spin per unit cell $\boldsymbol{I}$ is defined as $\boldsymbol{S_I} = \sum_{\boldsymbol{i}\in\boldsymbol{I}} \boldsymbol{S^f_i} + \sum_{\boldsymbol{x}\in\boldsymbol{I}} (-1)^{\boldsymbol{x}} \boldsymbol{S^c_x}$ and captures the aforementioned ferro-antiferromagnetic order of both f-spins and conduction electrons. The spectral function of the conduction electrons $A_c(\boldsymbol{k},\omega) = -\frac{1}{\pi}\,\mathrm{Im}\, G^{\mathrm{ret}}_c(\boldsymbol{k},\omega)$ can be extracted from the imaginary time resolved Greens function $G_c(\boldsymbol{k},\tau) = \sum_{\alpha,\sigma} \langle c^{\dagger}_{\boldsymbol{k},\alpha,\sigma}(\tau) c_{\boldsymbol{k},\alpha,\sigma}(0) \rangle$ by using the maximum-entropy method [139, 140] (see also Sec. 2.4). Here α is the orbital index for the honeycomb lattice. The auxiliary field QMC method also allows to study the entanglement properties of fermionic models [232–237]. In particular, as shown in Refs. [233, 234], the second Renyi entropy S_2 can be computed from the knowledge of Greens-functions G_A, restricted to subsystem A for two independent Monte Carlo samples. An alternative approach exploits the replica trick, e.g. for fermionic [238–241], bosonic [84], or spin systems [242, 243]. For a given subsystem of conduction electrons Γ_c and of local moments Γ_f, the Renyi mutual information between Γ_c and Γ_f is $I_2(\Gamma_c,\Gamma_f) \equiv -S_2(\Gamma_c \cup \Gamma_f) + S_2(\Gamma_c) + S_2(\Gamma_f)$. Here, we define two sequences of Γs as shown in Fig. 6.2(b), (c) and, Fig. 6.2(d),(e), respectively. In the calculation of the Renyi mutual information we use an improved estimator that restores the C_3 lattice symmetry by averaging over rotationally equivalent Γs.

6.2.1. Fermionization & implementation of the model

Let us first state the fermionized Hamiltonian that is simulated, $\mathcal{H}_{\text{qmc}}$, and then show its equivalence to Eq. (6.1).

$$\begin{aligned}\mathcal{H}_{\text{qmc}} &= -t\sum_{\langle \boldsymbol{x},\boldsymbol{y}\rangle,\sigma}\tilde{c}^{\dagger}_{\boldsymbol{x},\sigma}\tilde{c}_{\boldsymbol{y},\sigma}+h.c.-\frac{J^{\perp}}{4}\sum_{\langle \boldsymbol{i},\boldsymbol{j}\rangle}\left[2\left(\sum_{\sigma}\tilde{f}^{\dagger}_{\boldsymbol{i},\sigma}\tilde{f}_{\boldsymbol{j},\sigma}+h.c.\right)^2+\left(n^{\tilde{f}}_{\boldsymbol{i}}+n^{\tilde{f}}_{\boldsymbol{j}}-1\right)^2\right]\\ &\quad -\frac{J^{z}}{4}\sum_{\hexagon}\sum_{\boldsymbol{i}_{\hexagon}<\boldsymbol{j}_{\hexagon}}\left(n^{\tilde{f}}_{\boldsymbol{i}}-n^{\tilde{f}}_{\boldsymbol{j}}\right)^2-\frac{J_K}{4}\sum_{\langle \boldsymbol{i},\boldsymbol{x}\rangle}\left(\sum_{\sigma}\tilde{f}^{\dagger}_{\boldsymbol{i},\sigma}\tilde{c}_{\boldsymbol{x},\sigma}+h.c.\right)^2, \qquad (6.3)\end{aligned}$$

with $(\tilde{c}^{\dagger}_{\boldsymbol{x},\uparrow},\tilde{c}^{\dagger}_{\boldsymbol{x},\downarrow})=(c^{\dagger}_{\boldsymbol{x},\uparrow},(-1)^{\boldsymbol{x}}c_{\boldsymbol{x},\downarrow})$ and $(\tilde{f}^{\dagger}_{\boldsymbol{i},\uparrow},\tilde{f}^{\dagger}_{\boldsymbol{i},\downarrow})=(f^{\dagger}_{\boldsymbol{i},\uparrow},f_{\boldsymbol{i},\downarrow})$. The Hamiltonian above is identical to Eq. (6.1) up to the following five terms:

$$\begin{aligned}\mathcal{H}_{\text{qmc}}-\mathcal{H} &= +(J^{\perp}+4J^{z})\sum_{\boldsymbol{i}}(n^{f}_{\boldsymbol{i}}-1)^2 \qquad (6.4a)\\ &\quad +J^{\perp}\sum_{\langle \boldsymbol{i},\boldsymbol{j}\rangle}f^{\dagger}_{\boldsymbol{i},\uparrow}f^{\dagger}_{\boldsymbol{i},\downarrow}f_{\boldsymbol{j},\downarrow}f_{\boldsymbol{j},\uparrow}+\frac{J_K}{2}\sum_{\langle \boldsymbol{i},\boldsymbol{x}\rangle}(-1)^{\boldsymbol{x}}f^{\dagger}_{\boldsymbol{i},\uparrow}f^{\dagger}_{\boldsymbol{i},\downarrow}c_{\boldsymbol{x},\downarrow}c_{\boldsymbol{x},\uparrow}+h.c. \qquad (6.4b)\\ &\quad +\frac{J^{\perp}}{2}\sum_{\langle \boldsymbol{i},\boldsymbol{j}\rangle}(n^{f}_{\boldsymbol{i}}-1)(n^{f}_{\boldsymbol{j}}-1)+\frac{J_K}{4}\sum_{\langle \boldsymbol{i},\boldsymbol{x}\rangle}(n^{f}_{\boldsymbol{i}}-1)(n^{c}_{\boldsymbol{x}}-1)\,. \qquad (6.4c)\end{aligned}$$

The first term, Eq. (6.4a), is the well known repulsive Hubbard interaction that suppress charge fluctuations of f-electrons. The local parity of the f-electrons $(n^{f}_{\boldsymbol{i}}-1)^2$ commutes with the Hamiltonian as the relevant terms, Eq. (6.4b), describe pair-hopping processes that modify the local occupation by 2. Hence the Hubbard interaction projects onto the sector with single-occupied f-electron sites exponentially fast and the relevant scale is set by $\beta(J^{\perp}+4J^{z})$. In this subspace of single-occupied f-electron sites, pair-hopping terms are blocked by the Pauli exclusion principle and also the other contributions in Eq. (6.4c) vanish such that $\mathcal{H}_{\text{qmc}}|_{(n^{f}_{\boldsymbol{i}}-1)^2=0}=\mathcal{H}$. The interested reader is referred to the supplemental material of Ref. [228], in particular Eq. (9), for more information. Observe that $\mathcal{H}_{\text{qmc}}$ is explicitly $SU(2)$ invariant and that all interaction terms are attractive for $J^{\perp},J^{z},J_K>0$. In this case, the negative-sign problem is absent.[2]

6.3. Results

The pure BFG model supports a second order phase transition between a magnetic ordered phase and a $\mathbb{Z}_2$ spin liquid at $J^{z}_{c}/J^{\perp}\simeq 7.07$ [84]. Recently, the dynamics of this model have been investigated in Ref. [244] where the authors report a spin and a vision gap at an inter-

[2]The attractive interaction assure a real Hubbard-Stratonovich decoupling with Eq. (2.11) as $-\Delta\tau(-J)>0$. Hence the determinate is real and its square, due to the $SU(2)$-symmetry, is positive.

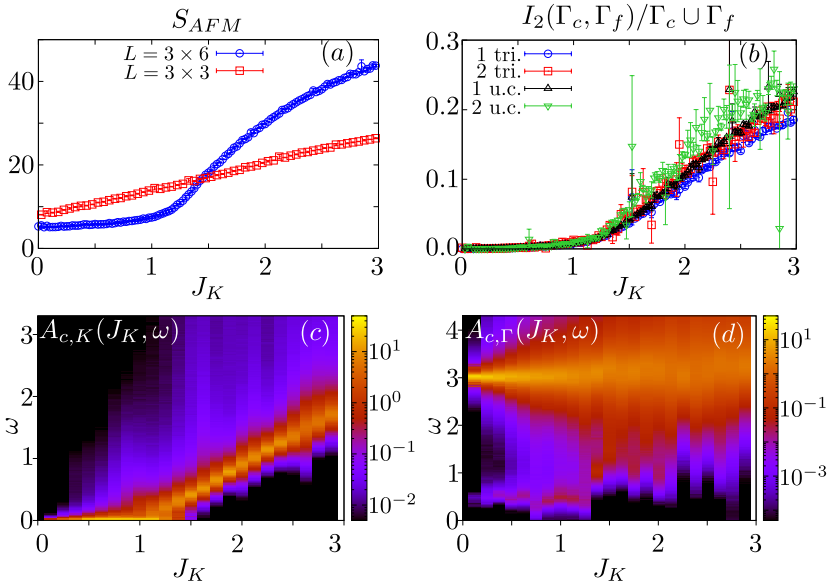

Figure 6.4.: We consider lattices $L = 3 \times 3$ and $L = 3 \times 6$ unit cells at an inverse temperature $\beta = 12$ and at $J^z = 7.5$. (a) Spin-spin correlations S_{AFM} (See text), (b) Renyi mutual informations $I_2(\Gamma_c, \Gamma_f)$ per site of the patch $\Gamma_c \cup \Gamma_f$ for $L = 3 \times 6$. Here we consider the patches listed in Fig. 6.2(b)-(e). (c) Conduction electron spectral function at the Dirac point $\boldsymbol{K}$ for the 3×6 lattice. (d) Same as (c), but at the Γ-point. The imaginary time data from which panels (c) and (d) stem are presented in the Fig. 6.6.

action strength of $J^z/J^\perp = 8.\overline{3}$ as $\Delta_s/J^\perp \simeq 7.12$ and $\Delta_v/J^\perp \simeq 0.2$, respectively. The vision excitation remains gapped at the phase transition whereas the spin gap scales as $(J^z - J^z_c)^{\nu z}$ with the dynamical critical exponent $z = 1$ and $\nu \simeq 0.67$, which correspond to the exponents of the 3D XY* model [82, 86, 245]. We have fixed the temperature to $\beta t = 12$ and from the discussion above, this choice of temperature places us well below the spin gap and allows us to resolve the vison excitation gap. From here on out, we fix $J^\perp = t$ and use $t = 1$ as the unit of energy[3].

The numerical results for a scan in J_K at a fixed value of $J^z = 7.5$ are presented in Fig. 6.4. Starting at $J_K = 0.0$, the conduction electrons and the local moments are explicitly decoupled such that the electrons form a Dirac semi-metal. With increasing J_K, the Dirac cone remains stable as apparent from the gapless single-particle spectrum at the Dirac point K reported in panel (c). In comparison to the non-interacting limit, the spectral weight is being reduced and broadened, until a full gap opens up around $J_K \sim 1.3$. This transition coincides with the sharp upturn of the magnetization as presented in panel (a). For values below $J_K \lesssim 1.5$, the response decreases with system size whereas it increases for larger values. This is in agree-

[3]This arbitrary choice is not expected to have a tremendous effect on the results here. Mainly because we are interested in the numerical realization of the 'fractional Fermi liquid' phase. $(J^\perp)^2/J^z$ sets the gap of the spin liquid such that the 'FL*' phase persists for small enough Kondo couplings, relatively insensitive to the conduction-electron energy scale t.

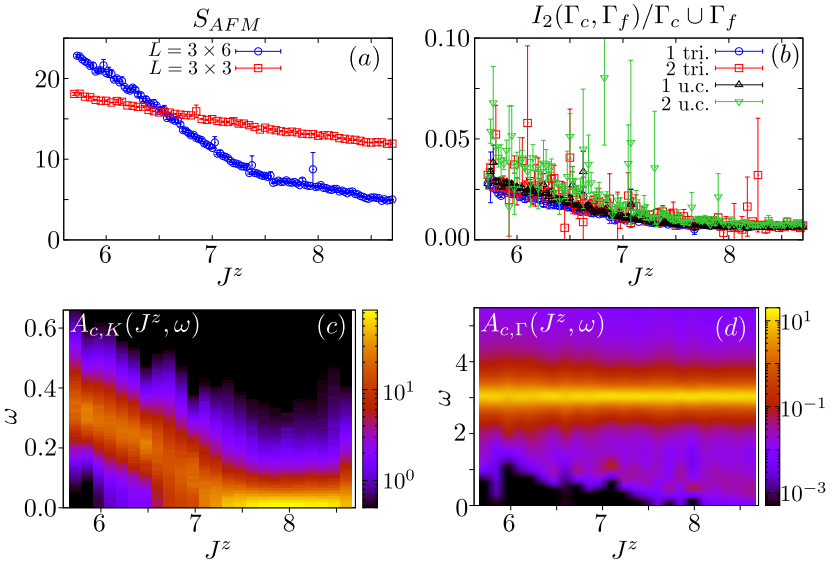

Figure 6.5.: We consider lattices $L = 3 \times 3$ and $L = 3 \times 6$ unit cells at an inverse temperature $\beta = 12$ and at $J_K = 1$. (a) Spin-spin correlations S_{AFM} (See text), (b) Renyi mutual information $I_2(\Gamma_c, \Gamma_f)$ per site of the patch $\Gamma_c \cup \Gamma_f$ for $L = 3 \times 6$. Here we consider the patches listed in Fig. 6.2(b)-(e). (c) Conduction electron spectral function at the Dirac point $\boldsymbol{K}$ for the 3×6 lattice. (d) same as (c), but at the Γ-point. The imaginary time data from which panels (c) and (d) stem are presented in the Fig. 6.6.

ment with spontaneous symmetry breaking and the establishment of a finite magnetization as discussed in the limiting cases of Sec. 6.1.2.

The attentive reader might have realized that the weak interaction strength also set comparatively small Kondo scales that might be hard to resolve, especially within the limited lattice sizes and finite temperatures accessible by the QMC simulation. To address this point, we report a complementary scan with various levels of frustration J^z and fixed Kondo coupling $J_K = 1$ in Fig. 6.5. At weak level of frustration, we expect a magnetic insulator and the single-particle gap presented in panel (c) as well as the scaling behavior of the spin-spin correlation function shown in panel (a) are consistent with this. At higher frustration, the gap of the Dirac cone is first reduced until a gapless spectrum is recovered for $J^z \gtrsim 7$ when the local moments form a $\mathbb{Z}_2$ spin liquid.

Additionally, there are interesting features present in the spectrum of the conduction electrons at the center of the Brillouin zone Γ. We find a weak but finite signal at low energies $\omega \sim 0.5$ in Fig. 6.4(d) for weak Kondo coupling which disappears around $J_K \sim 1.3$. Hence it is only present in the 'FL*' phase where the local moments exhibit topological order. A similar mode is present in Fig. 6.5(d) starting at $J^z \sim 7$, again only for the fractional Fermi liquid state. As shown in the following section (see Sec. 6.3.1), this is not an artifact of the MaxEnt method but also directly visible in the imaginary-time resolved greens function. The energy scale of this mode and its disappearance when the topological order is destroyed

suggest that this feature is related to the vison excitation of the spin liquid. Indeed the vison does not carry a $\mathbb{Z}_2$ gauge charge such that it generically couples to conduction electrons.

It is also worth to study alternative, more direct measure of Kondo screening. Therefore we investigate the (second) Renyi mutual information I_2 between the c-electrons and the local moments as reported in Ref. [246]. This quantity is sensitive to all energy scales[4], hence even for the perfectly decoupled 'FL*' ground state, we expect a small but still finite value. Therefore the mutual information only vanishes at $J_K = 0$ where the full Hilbert space decouples and not only the ground state. In the opposite limit of maximal entanglement, two singlets might be formed between two conduction electrons and two out-of the three local moments per unit cell such that $4\log(2)/5$ is the upper bound on the mutual information per site. The magnetic phase lies in between those limits as the local moments and the conduction electrons will also develop a finite entanglement within each other.

In Fig. 6.4 (b) and Fig. 6.5 (b) we report an entanglement that seems to follow a volume law as the various patch sizes fall on top of each other. They systematically grow as the Kondo interaction is increased or the frustration reduced, respectively. The (almost) vanishing entanglement for $J_K \lesssim 1.3$ and $J^z \gtrsim 7$, respectively, is consistent with decoupled c- and f-electrons as in the ground state of the 'FL*' phase. Note that the values found here are much smaller than those reported for generic, unfrustrated Kondo lattice model oin Ref. [246]. Furthermore, even on a limited size lattices such as ours, one can already see signatures of the transition from the magnetically ordered phase to the 'FL*' phase as indicated by the changing slope in the coefficient of the Renyi mutual information at the transition.

6.3.1. Time displaced Greens function

Here we report the imaginary-time displaced Greens functions of conduction electrons, $G_c(\boldsymbol{k},\tau) = \sum_{\alpha,\sigma}\langle c^\dagger_{\boldsymbol{k},\alpha,\sigma}(\tau)c_{\boldsymbol{k},\alpha,\sigma}(0)\rangle$ where α is the orbital and σ the spin index. The dynamical data presented before, is obtained by solving

$$G_c(\boldsymbol{k},\tau) = \frac{1}{\pi}\int d\omega \frac{e^{-\tau\omega}}{1+e^{-\beta\omega}} A_c(\boldsymbol{k},\omega) \tag{6.5}$$

for $A_c(\boldsymbol{k},\omega)$ using the stochastic maximum entropy method [139, 140]. The features presented so far can clearly be detected in the imaginary time data presented here and are thus not an artifact of the cumbersome analytic continuation. In Fig. 6.6, the left hand side panels presents the J_K scan at a fixed $J^z = 7.5$ whereas on the right hand side we show the J^z scan at constant $J_K = 1.0$.

Panels (a) and (b) depict the Greens function at the Dirac points. In both cases, the gapless mode is clearly visible in the 'FL*'phase since $G_c(\boldsymbol{K},\tau)$ shows a plateau at *large* imaginary

[4]The mutual information falls into the class of equal-time correlators which effectively integrate over all frequencies.

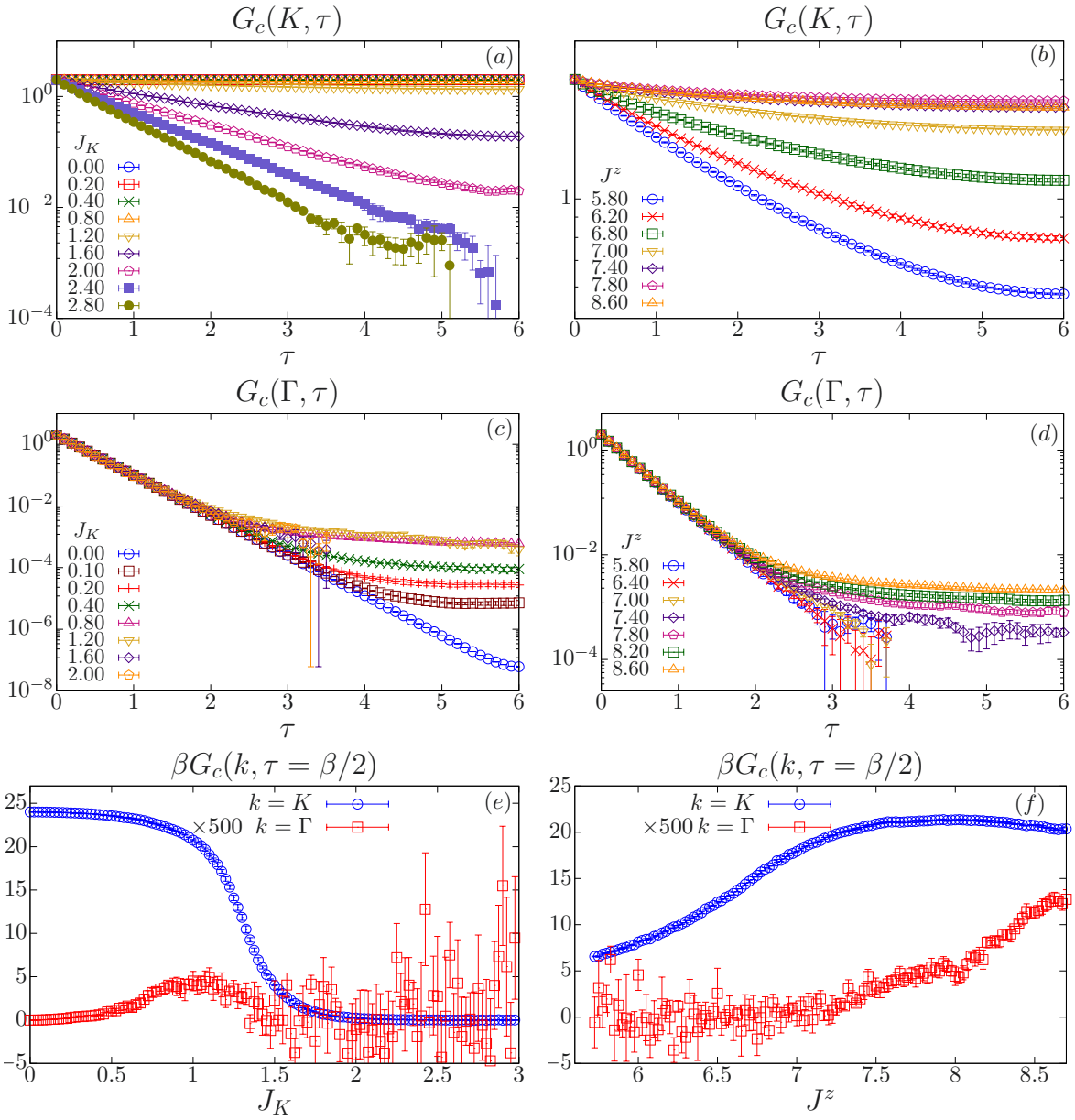

Figure 6.6.: The simulations were performed on the $L = 3 \times 6$ lattice at an inverse temperature of $\beta = 12$. Left panels corresponds to the J_K scan at $J^z = 7.5$ and the right to the J^z scan at $J_K = 1.0$. For large J_K or small J^z, we restricted the time domain in (c) and (d) to $\tau < 3.5$ and $\tau < 3.75$, respectively, since beyond this scale, the data becomes very noisy.

times. The height of this plateau encodes the quasi-particle residue.

Panels (c) and (d) present the equivalent data for the center of the Brillouin zone at the Γ point. In the 'FL*'phase we see a clear feature with small intensity at *large* values of τ. It is this feature in the imaginary time Green function that generates the low energy spectral weight in Figs. 6.4(d) and 6.5(d) in the 'FL*'phase. As mentioned before, we interpret this feature as a signature of the vison excitation.

Another possible analysis makes use of the identity,

$$\lim_{\beta\to\infty} \beta G_c(\boldsymbol{k}, \tau = \beta/2) = A_c(\boldsymbol{k}, \omega = 0), \tag{6.6}$$

that holds when $A_c(\boldsymbol{k}, \omega)$ is a smooth function. At finite temperatures, $\beta G_c(\boldsymbol{k}, \tau = \beta/2)$ will provide an estimate of the spectral weight in an energy window around $\omega = 0$ with a width set by $1/\beta$. Panels (e) and (f) plot this quantity both at the Γ and Dirac points. Overall, these panels again confirm that in the 'FL*'phase we observe low energy excitations with small intensity at the Γ point and low energy excitations with large spectral weight at the Dirac point. Note that in panel (e), corresponding to the J_K scan, the intensity of the feature at the Γ point first grows and then decreases since both at $J_K = 0$, where the spin and conduction electrons decouple and the conduction electrons form a Dirac spectrum, and at $J_K \gg 1$ where in the magnetic insulating phase, no low lying single particle weight is expected at the Γ point.

6.4. Discussion

In this study, we simulated a frustrated Kondo lattice model using a quantum Monte Carlo method without suffering the infamous negative-sign problem. Therefore, we can report the first numerical realization of a fractional Fermi liquid that remarkably violates Luttinger's sum rule by having a 'small' Fermi surface due to topological order. The numerics are extremely challenging, mainly due to long auto-correlation times, and they should therefore be viewed as a prove of principle. To improve future numerical studies, it might be helpful to directly simulate spinon systems subject to $\mathbb{Z}_2$ gauge fields, e.g., following Refs. [191, 247, 248], and couple them to conduction electrons. This is promising as we had to generate the 'emergent' topological order dynamically from regular spins on a lattice. With the help of improved models, it should be possible to access the phase transition numerically and test the proposed field theory of the critical point [86]. The Kondo coupling is claimed to be irrelevant due to the large anomalous exponent of the spin system. Therefore one expects well defined electronic quasiparticles at the phase transition and the spin part should be characterized by the critical exponents of the 3D XY* transition [82, 245].

In addition, it would be interesting to study the sub-leading contributions to the Renyi en-

tanglement entropy, a quantity that has already been used in Ref. [84] to identify the topological order in the pure BFG model. Within the fractional Fermi liquid phase, the sub-leading corrections are given as $\gamma = \gamma_{\text{topo}} + \gamma_{\text{Dirac}}$, where $\gamma_{\text{topo}} = \log(2)$ stems from the topological order of the BFG model and γ_{Dirac} is the shape-dependent universal contribution from the Dirac semi-metal [249, 250]. At the phase transition, however, $\gamma = \gamma_{\text{topo}} + \gamma_{\text{Dirac}} + \gamma_{\text{3D XY}}$ picks up the additional contribution of the universality class due to irrelevance of Kondo coupling [249].

To conclude, let us reconnect with the introduction where we have discussed on the relevance of frustration in experiments on heavy fermion systems. Our simulations demonstrate that among other things, the frustration can give rise to universal features like a 'small' Fermi surface and therefore illustrates one possible explanation of Kondo breakdown.

CHAPTER 7

Conclusion & outlook

In recent years, there has been tremendous progress in the field of topological free fermion systems [14–17], stimulated by the discovery of topological band insulators [11–13]. The inclusion of interaction poses questions that are harder to solve and during the course of this thesis, we gained access to four different aspects of correlated topological model systems. Our methods of choice were two flavors of quantum Monte Carlo algorithms, namely the continuous-time interaction expansion approach (CT-INT) and the auxiliary-field method (BSS). Both algorithms solve the model Hamiltonian in polynomial compute time, given that the negative-sign problem is absent. In Ch. 3, the model generically exhibits the negative-sign problem and we experienced its implication first hand, when the extrapolation to the thermodynamic limit was too expensive and we were left with the discussion of leading instabilities instead of long-range order.

However, numerical simulations can still be challenging even in the absence of the infamous sign problem. In Ch. 4, the (squared) order parameter exhibited a fat tail in its probability distribution for the CT-INT method such that the central-limit theorem was inapplicable. We saw that this issue strongly depends on the details of the QMC method and we could rely on the BSS algorithm to study the phase transition. Interestingly, the continuous-time auxiliary-field method, which usually interpolates between the CT-INT and BSS algorithm, could not connect the two methods in this model. Additionally, long auto-correlation times may lead to inefficient numerical simulations as apparent from Ch. 6 and parallel tempering schemes and/or global moves that mimic physical excitation can improve the efficiency.

In Ch. 3, we discussed a nodal topological superconductor that exhibits Majorana flat-bands at zero energy which are located between the projection of the bulk nodes within the boundary Brillouin zone. Several studies had discussed various mean-field scenarios before,

however, we reported the first numerical exact QMC solution that properly addresses the influence of quantum fluctuation which are expected to be large due to the low dimensionality and the high density of states along the edge. We find the ferromagnetic instability in case of repulsive interaction and charge-density-wave and/or additional *i*s-wave order for attractive couplings. Both are in agreement with the previous insights. However, we demonstrate the importance of the edge mode's chirality in a refined mean-field discussion that induce linear superposition of normal and superconducting order parameters. The QMC simulation confirm that, for example, the ferromagnetic order is coherently mixed with triplet pairing. We also proposed an experimental setup that should be able to detect this coherence. In future studies, it would be interesting to extend this model to non-centrosymmetric lattices in which spin-orbit coupling as well as the mixing of singlet and triplet superconductivity have to be taken into account. This can lead to a single Majorana flat-band, compared to two bands from before, that should modify its stability.

In Ch. 4, we considered spinless fermions with nearest-neighbor repulsion, motivated by a scenario in which spontaneous time-reversal-symmetry breaking generates a topological Chern insulator. Instead we found the formation of charge-density-wave order as a thermodynamic instability that breaks the particle-hole-symmetry and effectively dopes the lattice model to a filling fraction of $1/3$ or $2/3$. This insight led to the proposal that uses the particle-hole-symmetry to guarantee the absence of the negative-sign problem as well as the thermodynamic instability to effectively dope a second 'target' layer in order to investigate models away from half filling and thereby increase the range of solvable models. We also compared the two QMC flavors and argued that a third option, the continuous-time auxiliary field algorithm, should be the method of choice for such models as it combines the advantages of the weak coupling expansion and the more favorable probability distribution of the BSS method, which exhibits less severe fat tails.

In Ch. 5, we explicitly tested the adiabatic connection of bulk states that represent topologically distinct free fermion phases in a numerically exact manner. This setup was motivated by previous works that had derived specific types of interaction terms which symmetrically gap the degenerate topological boundary states. We found an extended symmetry broken regime that separates the topological phases, in addition to the (non-interacting) Dirac semimetal. Adding frustration does not pave the way of the adiabatic connection as a direct first-order phase transition then replaces the long-range ordered state. We discussed several implications of our finding that mainly evolve around the statement that the conditions introduced so far may very well be necessary, however they do not appear to be sufficient in the context of this study. For future investigations, we propose to either fine-tune bulk parameters, which, for example, concentrate the currently homogeneous Berry curvature within the Brillouin zone, such that the model is more friendly with respect to the hierarchy of energy scales used in the boundary state based arguments. Alternatively, we also discuss the phase diagram from a bulk criticality point of view and review the symmetric mass generation in

a $SU(4)$ symmetric 'graphene' model [209–211]. This is one possibility to terminate the semi-metal, however, a small symmetry broken domain at the end point constitutes a more conventional setup. Finally, it would be very interesting to test the bulk-boundary correspondence on its own as it might be possible to gap out the boundary modes even though the bulk is still deformable to representations of non-trivial topological free fermion phases. This could be the first example where the bulk-boundary correspondence is violated.

In Ch. 6, we report a numerical simulation of frustrated local moments Kondo coupled to a Dirac semi-metal that does not exhibit the negative-sign problem. We present convincing evidence for a decoupling of the spin system and the conduction electrons at strong frustration and weak Kondo coupling. On one hand, we find an (almost) vanishing mutual information between the spin and the electron subsystem and, on the other hand, the Dirac cone remains massless such that the electrons exhibit a 'small' Fermi surface which violates Luttinger's theorem. Combining both observations strongly indicates that this phase is not a regular but rather a 'fractional Fermi liquid'. From a technical perspective, the simulation were limited by long auto-correlation times which restricted the accessible lattice size as well as the temperature range. We believe that it will be rewarding to further investigate the exotic phase transition between the 'fractional Fermi liquid' and the magnetically ordered phase (at low frustration). To overcome the algorithmic challenges, we propose to design a similar model of spinons with a $\mathbb{Z}_2$ gauge interaction, the fundamental excitations of the quantum spin liquid, and couple them directly to conduction electrons rather then generating those degrees of freedom dynamically in frustrated spin-$1/2$ models.

In summary, we have investigated four different model systems that – in principle – represent the distinct scenarios for the interplay of topology and interactions. We showed that correlations can induce spontaneous symmetry breaking that gaps the topological boundary modes in Ch. 3. An attempt to dynamically generate a topological mass term was reported in Ch. 4 where we found another kind of symmetry breaking. The first realization of that has now been provided in Ref. [48]. In Ch. 5, we determined the phase diagram for an SPT model and concluded that the current arguments on the reduced classification of correlated topological states might contain necessary but not sufficient conditions. Finally, we present the first numerical realization of a 'fractional Fermi liquid' in Ch. 6.

Appendices

APPENDIX A

Topology, edge states and mass terms

Let us interpret the two-dimensional model defined by Eq. (3.1) as a set of one-dimensional chains indexed by $k_\parallel$. These subsystems are then described by the Hamiltonian $\mathcal{H}_{k_\parallel} = \sum_{k_\perp} \Psi^\dagger_{\mathbf{k}} H_{k_\parallel}(k_\perp)\Psi_{\mathbf{k}}$ with

$$H_{k_\parallel}(k_\perp) = -(2t\cos(k_\perp) + \mu_{k_\parallel})\tau_z + \Delta_{k_\parallel}\sin(k_\perp)\tau_x\,. \tag{A.1}$$

Before we derive the edge state of Eq. (A.1), we start by discussing symmetry class of each model Hamiltonian for a given and fixed $k_\parallel$. Within each one-dimensional system, there exists one commuting time-reversal symmetry $\mathcal{T}_{k_\parallel} = U_T\mathcal{K}$ (TRS) and one anti-commuting $\mathcal{C}_{k_\parallel} = U_C\mathcal{K}$ (PHS). Observe that the complex conjugation $\mathcal{K}$ inverts only the perpendicular momentum $k_\perp$ but leaves the parallel contribution invariant which stresses the index character of this part ($\mathcal{K}\Psi_{k_\parallel,k_\perp}\mathcal{K} = \Psi_{k_\parallel,-k_\perp}$). Consequently, the unitary parts act as $U^\dagger_{T,C}H_{k_\parallel}(k_\perp)U_{T,C} = \pm H^*_{k_\parallel}(-k_\perp)$ and are given by $U_T = -\tau_z$ and $U_C = i\tau_x$ for TRS and PHS, respectively. It is straight forward to show that both symmetry operations square to unity, $\mathcal{C}^2_{k_\parallel} = +\mathbf{1}$ and $\mathcal{T}^2_{k_\parallel} = +\mathbf{1}$.[1] These properties places each system $\mathcal{H}_{k_\parallel}$ into symmetry class BDI [18, 37].

Actually, for a fixed $k_\parallel$, Eq. (A.1) is an instance of the Kitaev chain specified by the parameters $\mu_{k_\parallel} = \mu + 2t\cos(k_\parallel)$ and $\Delta_{k_\parallel} = \Delta_{d_{xy}}\sin(k_\parallel)$ [53]. Hence, the one-dimensional system is topologically non-trivial for $2|t| > |\mu_{k_\parallel}|$, provided $\Delta_{k_\parallel} \neq 0$. The topological invariant is the winding number $W_{k_\parallel} = (2\pi i)^{-1}\int_0^{2\pi} d\,k_\perp \partial_{k_\perp}\ln(q_{\mathbf{k}})$, where we used $q_{\mathbf{k}} = \varepsilon_{\mathbf{k}} + i\Delta_{\mathbf{k}}$ [251]. In Fig. A.1(a), we present a vector plot of the phase $q_{\mathbf{k}}/|q_{\mathbf{k}}|$ for a finite chemical potential. The

[1] We made explicit use of the spin-symmetry, namely σ_z, by block-diagonalizing the full Hamiltonian. Eq. (3.1) represents the $\uparrow\uparrow$-sector (still containing all physical information), hence $\mathcal{T}^2_{k_\parallel} \neq -\mathbf{1}$.

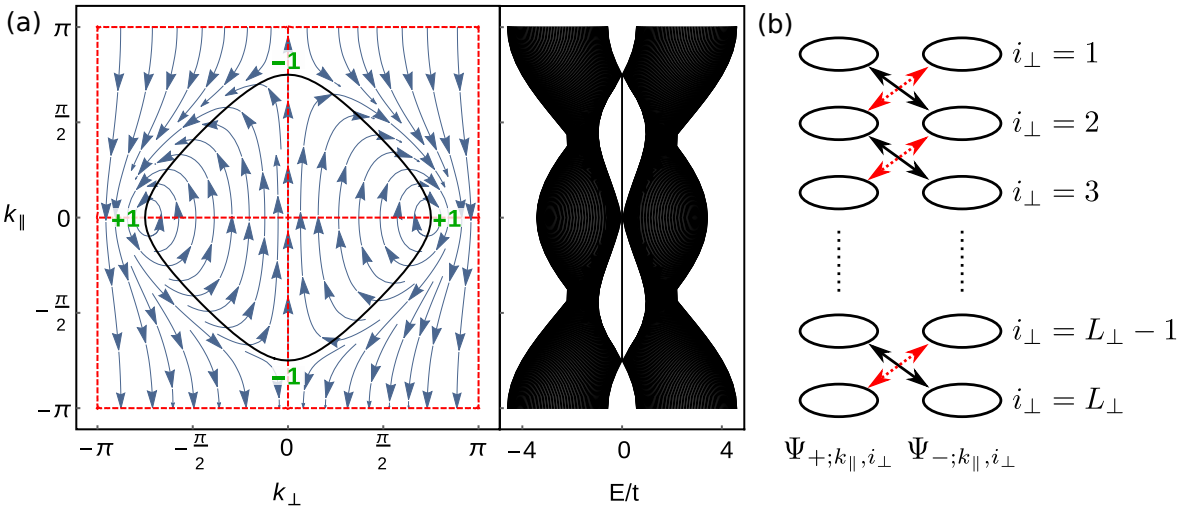

Figure A.1.: (a) Wave-function topology of Eq. (3.1). The left part shows the normal state Fermi surface (black, solid), the nodal lines of $\Delta_{\mathbf{k}}$ (red, dashed), the phase of $\varepsilon_{\mathbf{k}} + i\Delta_{\mathbf{k}}$ (blue arrows), and the topological charge of the bulk nodes (green). The right part shows the edge spectrum containing zero-energy flat-bands. (b) Visualization of Eq. (A.2): Hopping along the black (dashed red) bonds for $s_{k_\parallel} = \mathrm{sgn}(t\Delta_{k_\parallel})$ positive (negative); unpaired zero-energy modes $\Psi^\dagger_{\pm;k_\parallel,i_\perp=1}$ and $\Psi^\dagger_{\mp;k_\parallel,i_\perp=L_\perp}$ at the ends of the chain.

Fermi surface is depicted as a solid black line and the nodes of the superconducting pairing is represented as dashed red lines. Traversing $k_\perp$ for a fixed value $k_\parallel \approx \pm\pi$ nicely shows both the trivial winding, namely none, as well as the absence of zero-energy edge states. For $k_\parallel \approx \pm 0$, the phase winds around the origin of the complex plane once and the does exist a zero-energy mode in the spectrum.

Next, let us use a heuristic but very intuitive argument to illustrate the existence of edge states. It is common to distinguish two pairing regimes, the weak-pairing one ($2|t| > |\mu_{k_\parallel}|$) and the strong-pairing limit ($2|t| < |\mu_{k_\parallel}|$). Observe that any representation in the latter can be adiabatically connected to a band insulator, with either a fully occupied or unoccupied single band, by turning of the pairing completely $\Delta_{k_\parallel} = 0$. Hence this regime is topologically trivial. For the opposite regime, we may adiabatically tune the weak-pairing Hamiltonian to the high-symmetry point with $(\mu_{k_\parallel}, \Delta_{k_\parallel}) = (0, 2t\,\mathrm{sgn}[t\Delta_{k_\parallel}])$. Here, we can readily infer $q_{k_\parallel} = -2t\exp(-i\,\mathrm{sgn}[t\Delta_{k_\parallel}]k_\perp)$ and conclude that this phase shows a non-trivial winding with its sign determined by $\mathrm{sgn}[t\Delta_{k_\parallel}]$. Hence, the region $k_\parallel \approx \pm\pi$ in Fig. A.1(a) is representing the trivial strong-pairing regime whereas $k_\parallel \approx 0$ stands for the weak-pairing scenario. The figure also nicely shows that the topology can only change at the nodal points of the bulk spectrum and thus that the flat bands always connect projection of those nodes to the edge Brillouin zone.

With this picture at hand, we are equipped to derive the edge states more rigorously and also determine the form of their wave functions. We can combine TRS and PHS into the

chiral symmetry $\mathcal{S}_{k_\parallel} = \mathcal{C}_{k_\parallel}\mathcal{T}_{k_\parallel} = -\tau_y$ which anti-commutes with the Hamiltonian. In the chiral basis, $\Psi_{\pm;k_\parallel}$, the Eq. (A.1) is off-diagonal. Lastly, we perform a Fourier transformation in the perpendicular direction $k_\perp$ and obtain

$$\mathcal{H}_{k_\parallel} \sim -2t\sum_{i_\perp}\Psi^\dagger_{+s_{k_\parallel};k_\parallel,i_\perp}\Psi_{-s_{k_\parallel};k_\parallel,i_\perp+1} + h.c.\,, \tag{A.2}$$

where we introduced the short hand notation $s_{k_\parallel} = \mathrm{sgn}(t\Delta_{k_\parallel})$. In Fig. A.1(b), we depict an illustration of Hamiltonian (A.2). Depending on the sign $s_{k_\parallel}$, either the black (positive) or the dashed red bonds (negative) are non-zero whereas the other one vanishes. Hence, the chain is decoupled into pairs of Majorana operators with opposite chiral eigenvalue. For open boundary conditions, the Majorana operators $\Psi^\dagger_{-s_{k_\parallel};k_\parallel,i_\perp=1}$ and $\Psi_{+s_{k_\parallel};k_\parallel,i_\perp=L_\perp}$ are unpaired, realizing Majorana zero modes localized at the ends of the chain. By tuning the parameters $(\mu_{k_\parallel},\Delta_{k_\parallel})$ away from the high symmetry point, the edge modes acquire a finite decay length and are now described by $\gamma^\dagger_{k_\parallel} = \sum_{i_\perp}\phi_{k_\parallel}(i_\perp)\Psi^\dagger_{-s_{k_\parallel};k_\parallel,i_\perp}$, with the wave function $\phi_{k_\parallel}(i_\perp)$ [53]. This result is derived in the remaining part of this section

The chiral symmetry $\mathcal{S}_{k_\parallel}$ allows to classify zero energy edge states by their chirality and we therefore use the chiral basis $|\pm\rangle = \frac{1}{\sqrt{2}}(1,\mp i)^T$ with $\mathcal{S}_{k_\parallel}|s\rangle = s|s\rangle$. This leads to the ansatz $\Phi_s(y) = e^{\kappa_s y}|s\rangle$ and the requirement of $\mathcal{H}_{k_\parallel}\Phi_s(y) = E\Phi_s(y)$ with $E=0$ generates the secular equation

$$0 = 2\frac{t_{k_\parallel}}{\Delta_{k_\parallel}}\cosh(\kappa_s) + \frac{\mu_{k_\parallel}}{\Delta_{k_\parallel}} + s\sinh(\kappa_s), \tag{A.3a}$$

that determines $\kappa_{s,\alpha}$

$$e^{\kappa_{s,\pm}} = \frac{-\mu_{k_\parallel} \pm \sqrt{\Delta^2_{k_\parallel} - (4t^2 - \mu^2_{k_\parallel})}}{2t + s\Delta_{k_\parallel}}. \tag{A.3b}$$

To fulfill the boundary conditions $\Phi_s(y=0) = 0$ and $\Phi_s(y\to\infty) = 0$ for a half-infinite geometry, the wave function has to be proportional to $e^{\kappa_{s,+}y} - e^{\kappa_{s,-}y}$. Additionally, normalizability requires that both $|e^{\kappa_{s,\pm}}|$ are either smaller or larger than 1. The former (latter) is then localized around $y=1$ ($y=L_\perp$). In the weak paring limit, we can use $|\sqrt{\Delta^2_{k_\parallel} - (4t^2-\mu^2_{k_\parallel})}| < |\Delta_{k_\parallel}|$ to approximate $|e^{\kappa_{s,\pm}}| < \frac{|2t|+|\Delta_{k_\parallel}|}{|2t+s\Delta_{k_\parallel}|}$. Hence, the chirality $s = \mathrm{sgn}(t\Delta_{k_\parallel})$ state is exponentially localized around $y=1$, whereas the state of opposite chirality is localized on the other edge, which can be inferred from the relation $e^{\kappa_{+,\pm}} = e^{-\kappa_{-,\mp}}$.

From now on, we focus on the top edge ($y=1$) and introduce the creation operator $\gamma^\dagger_{k_\parallel}$ for the according bound state $\Phi_{k_\parallel}$ with momentum $k_\parallel$ and chirality $s_{k_\parallel} = \mathrm{sgn}(t\Delta_{k_\parallel})$

$$\gamma^\dagger_{k_\parallel} = \sum_{i_\perp=1}^{L_\perp}\phi_{k_\parallel}(i_\perp)\frac{1}{\sqrt{2}}(c^\dagger_{k_\parallel,i_\perp\uparrow} - i s_{k_\parallel} c_{-k_\parallel,i_\perp\downarrow}), \tag{A.4a}$$

$$\phi_{k_\parallel}(y) = \mathcal{N}^{-1}(e^{y\kappa_{s_{k_\parallel},+}} - e^{y\kappa_{s_{k_\parallel},-}}), \tag{A.4b}$$

with the normalization $\mathcal{N}^2 = \sum_{y=1}^{L_\perp} |e^{y\kappa_{s_{k_\parallel},+}} - e^{y\kappa_{s_{k_\parallel},-}}|$. As $e^{\kappa_{s_{k_\parallel},\pm}}$ are either both real or a complex conjugate pair, $\phi_{k_\parallel}(y)$ can be chosen to be real, which is assumed from now on. We also observe that $\phi_{-k_\parallel}(y) = \phi_{k_\parallel}(y)$.

These edge states are charge neutral, carry a spin of $S_z = +1$ and their chirality is locked to the momentum as $\mathrm{sgn}(k_\parallel)$. In analogy to the edge states of a quantum-spin-hall system, the state with opposite chirality is bound to the second edge at infinity. Observe that the neutral edge states can still carry an electrical current as the electron-like contribution propagates in the opposite way as the hole-like part. In contrast, it cannot contribute to spin currents along the edge.

The flatness of the Majorana fermions ($E = 0$) is protected by the standard TRS ($c_{\mathbf{k}} \to i\sigma_y c_{-\mathbf{k}}$) and translation symmetry along the edge. All possible mass terms are given by

$$\mathcal{H}_q = \sum_{k_\parallel} \left[a_q(k_\parallel) \gamma^\dagger_{k_\parallel} \gamma_{k_\parallel + q} + b_q(k_\parallel) \gamma_{-k_\parallel} \gamma_{k_\parallel + q} + h.c. \right]. \tag{A.5}$$

The edge state operators transform under TRS as $\gamma^\dagger_{k_\parallel} \to -is_{k_\parallel} \gamma_{k_\parallel}$ and Eq. (A.5) accordingly as

$$\mathcal{H}_q \to -\sum_{k_\parallel} \mathrm{sgn}\left(\sin(k_\parallel)\sin(k_\parallel + q)\right) \left[a_q(k_\parallel) \gamma^\dagger_{k_\parallel} \gamma_{k_\parallel + q} + b_q(k_\parallel) \gamma_{-k_\parallel} \gamma_{k_\parallel + q} + h.c. \right]. \tag{A.6}$$

All homogeneous mass terms with $q = 0$ break only TRS, whereas all other terms with $q \neq 0, \pi$ break both TRS and translation symmetry. The instability with $q = \pi$ is special, since it only breaks translation, but not TRS.

Bibliography

[1] J. M. KOSTERLITZ and D. J. THOULESS. *Long range order and metastability in two dimensional solids and superfluids. (Application of dislocation theory)*. Journal of Physics C: Solid State Physics, **5**(11):L124–L126 (1972).

[2] J. M. KOSTERLITZ and D. J. THOULESS. *Ordering, metastability and phase transitions in two-dimensional systems*. Journal of Physics C: Solid State Physics, **6**(7):1181 (1973).

[3] N. D. MERMIN and H. WAGNER. *Absence of Ferromagnetism or Antiferromagnetism in One- or Two-Dimensional Isotropic Heisenberg Models*. Phys. Rev. Lett., **17**:1133–1136 (1966).

[4] K. V. KLITZING, G. DORDA and M. PEPPER. *New Method for High-Accuracy Determination of the Fine-Structure Constant Based on Quantized Hall Resistance*. Phys. Rev. Lett., **45**:494–497 (1980).

[5] E. H. HALL. *On a New Action of the Magnet on Electric Currents*. American Journal of Mathematics, **2**(3):287–292 (1879).

[6] D. J. THOULESS, M. KOHMOTO, M. P. NIGHTINGALE and M. DEN NIJS. *Quantized Hall Conductance in a Two-Dimensional Periodic Potential*. Phys. Rev. Lett., **49**:405–408 (1982).

[7] F. D. M. HALDANE. *Model for a Quantum Hall Effect without Landau Levels: Condensed-Matter Realization of the "Parity Anomaly"*. Phys. Rev. Lett., **61**:2015–2018 (1988).

[8] C. L. KANE and E. J. MELE. *Z_2 Topological Order and the Quantum Spin Hall Effect*. Phys. Rev. Lett., **95**(14):146802 (2005).

[9] C. L. KANE and E. J. MELE. *Quantum Spin Hall Effect in Graphene*. Phys. Rev. Lett., **95**(22):226801 (2005).

[10] F. REIS, G. LI, L. DUDY, M. BAUERNFEIND, S. GLASS, W. HANKE, R. THOMALE, J. SCHÄFER and R. CLAESSEN. *Bismuthene on a SiC substrate: A candidate for a high-temperature quantum spin Hall material*. Science, **357**(6348):287–290 (2017).

[11] B. A. BERNEVIG, T. L. HUGHES and S.-C. ZHANG. *Quantum Spin Hall Effect and Topological Phase Transition in HgTe Quantum Wells*. Science, **314**:1757– (2006).

[12] M. KÖNIG, S. WIEDMANN, C. BRÜNE, A. ROTH, H. BUHMANN, L. W. MOLENKAMP, X.-L. QI and S.-C. ZHANG. *Quantum Spin Hall Insulator State in HgTe Quantum Wells*. Science, **318**:766 (2007).

[13] D. HSIEH, D. QIAN, L. WRAY, Y. XIA, Y. S. HOR, R. J. CAVA and M. Z. HASAN. *A topological Dirac insulator in a quantum spin Hall phase*. Nature, **452**:970–974 (2008).

[14] M. Z. HASAN and C. L. KANE. *Colloquium: Topological insulators*. Rev. Mod. Phys., **82**(4):3045–3067 (2010).

[15] X.-L. QI and S.-C. ZHANG. *Topological insulators and superconductors*. Rev. Mod. Phys., **83**:1057–1110 (2011).

[16] C.-K. CHIU, J. C. Y. TEO, A. P. SCHNYDER and S. RYU. *Classification of topological quantum matter with symmetries*. Rev. Mod. Phys., **88**:035005 (2016).

[17] A. W. W. LUDWIG. *Topological phases: classification of topological insulators and superconductors of non-interacting fermions, and beyond*. Physica Scripta, **T168**:014001 (2015).

[18] A. P. SCHNYDER, S. RYU, A. FURUSAKI and A. W. W. LUDWIG. *Classification of topological insulators and superconductors in three spatial dimensions*. Phys. Rev. B, **78**:195125 (2008).

[19] S. RYU, A. P. SCHNYDER, A. FURUSAKI and A. W. W. LUDWIG. *Topological insulators and superconductors: tenfold way and dimensional hierarchy*. New Journal of Physics, **12**(6):065010 (2010).

[20] L. FU. *Topological Crystalline Insulators*. Phys. Rev. Lett., **106**:106802 (2011).

[21] S.-Y. XU, C. LIU, N. ALIDOUST, M. NEUPANE, D. QIAN, I. BELOPOLSKI, J. D. DENLINGER, Y. J. WANG, H. LIN, L. A. WRAY, G. LANDOLT, B. SLOMSKI, J. H. DIL, A. MARCINKOVA, E. MOROSAN, Q. GIBSON, R. SANKAR, F. C. CHOU, R. J. CAVA, A. BANSIL and M. Z. HASAN. *Observation of a topological crystalline insulator phase and topological phase transition in Pb1-xSnxTe*. Nature Communications, **3**:1192 EP – (2012). Article.

[22] K. SHIOZAKI and M. SATO. *Topology of crystalline insulators and superconductors*. Phys. Rev. B, **90**:165114 (2014).

[23] M. G. VERGNIORY, L. ELCORO, C. FELSER, N. REGNAULT, B. A. BERNEVIG and Z. WANG. *A complete catalogue of high-quality topological materials*. Nature, **566**(7745):480–485 (2019).

[24] C. WU, B. A. BERNEVIG and S.-C. ZHANG. *Helical Liquid and the Edge of Quantum Spin Hall Systems*. Phys. Rev. Lett., **96**:106401 (2006).

[25] F. GOTH, D. J. LUITZ and F. F. ASSAAD. *Magnetic impurities in the Kane-Mele model*. Phys. Rev. B, **88**:075110 (2013).

[26] R. QUEIROZ and A. P. SCHNYDER. *Helical Majorana surface states of strongly disordered topological superconductors with time-reversal symmetry*. Phys. Rev. B, **91**:014202 (2015).

[27] R. QUEIROZ and A. P. SCHNYDER. *Stability of flat-band edge states in topological superconductors without inversion center*. Phys. Rev. B, **89**(5):054501 (2014).

[28] O. FISCHER, M. KUGLER, I. MAGGIO-APRILE, C. BERTHOD and C. RENNER. *Scanning tunneling spectroscopy of high-temperature superconductors*. Rev. Mod. Phys., **79**:353–419 (2007).

[29] P. ROUSHAN, J. SEO, C. V. PARKER, Y. S. HOR, D. HSIEH, D. QIAN, A. RICHARDELLA, M. Z. HASAN, R. J. CAVA and A. YAZDANI. *Topological surface states protected from backscattering by chiral spin texture*. Nature, **460**:1106 EP – (2009).

[30] W.-C. LEE, C. WU, D. P. AROVAS and S.-C. ZHANG. *Quasiparticle interference on the surface of the topological insulator Bi_2Te_3*. Phys. Rev. B, **80**:245439 (2009).

[31] J. S. HOFMANN, R. QUEIROZ and A. P. SCHNYDER. *Theory of quasiparticle scattering interference on the surface of topological superconductors*. Phys. Rev. B, **88**(13):134505 (2013).

[32] M. HOHENADLER and F. F. ASSAAD. *Luttinger liquid physics and spin-flip scattering on helical edges*. Phys. Rev. B, **85**(8):081106(R) (2012).

[33] G. Z. MAGDA, X. JIN, I. HAGYMÁSI, P. VANCSÓ, Z. OSVÁTH, P. NEMES-INCZE, C. HWANG, L. P. BIRÓ and L. TAPASZTÓ. *Room-temperature magnetic order on zigzag edges of narrow graphene nanoribbons*. Nature, **514**(7524):608–611 (2014).

[34] H. FELDNER, Z. Y. MENG, A. HONECKER, D. CABRA, S. WESSEL and F. F. ASSAAD. *Magnetism of finite graphene samples: Mean-field theory compared with exact diagonalization and quantum Monte Carlo simulations*. Phys. Rev. B, **81**(11):115416 (2010).

[35] H. FELDNER, Z. Y. MENG, T. C. LANG, F. F. ASSAAD, S. WESSEL and A. HONECKER. *Dynamical Signatures of Edge-State Magnetism on Graphene Nanoribbons*. Phys. Rev. Lett., **106**:226401 (2011).

[36] Y. TANAKA, M. SATO and N. NAGAOSA. *Symmetry and Topology in Superconductors —Odd-Frequency Pairing and Edge States—*. J. Phys. Soc. Jpn., **81**(1):011013 (2012).

[37] S. MATSUURA, P.-Y. CHANG, A. P. SCHNYDER and S. RYU. *Protected boundary states in gapless topological phases*. New Journal of Physics, **15**(6):065001 (2013).

[38] A. P. SCHNYDER and P. M. R. BRYDON. *Topological surface states in nodal superconductors*. Journal of Physics Condensed Matter, **27**(24):243201 (2015).

[39] A. P. SCHNYDER and S. RYU. *Topological phases and surface flat bands in superconductors without inversion symmetry*. Phys. Rev. B, **84**(6):060504(R) (2011).

[40] M. MATSUMOTO and H. SHIBA. *Coexistence of Different Symmetry Order Parameters near a Surface in d-Wave Superconductors I*. J. Phys. Soc. Jpn., **64**:3384 (1995).

[41] M. MATSUMOTO and H. SHIBA. *Coexistence of Different Symmetry Order Parameters near a Surface in d-Wave Superconductors II*. J. Phys. Soc. Jpn., **64**:4867 (1995).

[42] M. FOGELSTRÖM, D. RAINER and J. A. SAULS. *Tunneling into Current-Carrying Surface States of High- T_c Superconductors*. Phys. Rev. Lett., **79**:281–284 (1997).

[43] C. TIMM, S. REX and P. M. R. BRYDON. *Surface instability in nodal noncentrosymmetric superconductors*. Phys. Rev. B, **91**(18):180503(R) (2015).

[44] C. HONERKAMP, K. WAKABAYASHI and M. SIGRIST. *Instabilities at [110] surfaces of $d_{x^2-y^2}$ superconductors*. EPL, **50**:368–374 (2000).

[45] A. C. POTTER and P. A. LEE. *Edge Ferromagnetism from Majorana Flat Bands: Application to Split Tunneling-Conductance Peaks in High-T_c Cuprate Superconductors*. Phys. Rev. Lett., **112**(11):117002 (2014).

[46] N. B. KOPNIN, T. T. HEIKKILÄ and G. E. VOLOVIK. *High-temperature surface superconductivity in topological flat-band systems*. Phys. Rev. B, **83**(22):220503(R) (2011).

[47] S. RAGHU, X.-L. QI, C. HONERKAMP and S.-C. ZHANG. *Topological Mott Insulators*. Phys. Rev. Lett., **100**(15):156401 (2008).

[48] Y. LIU, Z. WANG, T. SATO, M. HOHENADLER, C. WANG, W. GUO and F. F. ASSAAD. *Superconductivity from the condensation of topological defects in a quantum spin-Hall insulator*. Nature Communications, **10**(1):2658 (2019).

[49] T. SENTHIL, A. VISHWANATH, L. BALENTS, S. SACHDEV and M. P. A. FISHER. *Deconfined Quantum Critical Points*. Science, **303**(5663):1490–1494 (2004).

[50] T. SENTHIL, L. BALENTS, S. SACHDEV, A. VISHWANATH and M. P. A. FISHER. *Quantum criticality beyond the Landau-Ginzburg-Wilson paradigm*. Phys. Rev. B, **70**:144407 (2004).

[51] F. D. M. HALDANE. *O(3) Nonlinear σ Model and the Topological Distinction between Integer- and Half-Integer-Spin Antiferromagnets in Two Dimensions*. Phys. Rev. Lett., **61**(8):1029–1032 (1988).

[52] L. FIDKOWSKI and A. KITAEV. *Effects of interactions on the topological classification of free fermion systems*. Phys. Rev. B, **81**:134509 (2010).

[53] A. Y. KITAEV. *6. QUANTUM COMPUTING: Unpaired Majorana fermions in quantum wires*. Physics Uspekhi, **44**:131 (2001).

[54] E. TANG and X.-G. WEN. *Interacting One-Dimensional Fermionic Symmetry-Protected Topological Phases*. Phys. Rev. Lett., **109**:096403 (2012).

[55] H. YAO and S. RYU. *Interaction effect on topological classification of superconductors in two dimensions*. Phys. Rev. B, **88**:064507 (2013).

[56] T. MORIMOTO, A. FURUSAKI and C. MUDRY. *Breakdown of the topological classification $\mathbb{Z}$ for gapped phases of noninteracting fermions by quartic interactions*. Phys. Rev. B, **92**:125104 (2015).

[57] X.-L. QI. *A new class of (2+1)-dimensional topological superconductors with $\mathbb{Z}_8$ topological classification*. New Journal of Physics, **15**(6):065002 (2013).

[58] R. QUEIROZ, E. KHALAF and A. STERN. *Dimensional Hierarchy of Fermionic Interacting Topological Phases*. Phys. Rev. Lett., **117**:206405 (2016).

[59] A. M. TURNER, F. POLLMANN and E. BERG. *Topological phases of one-dimensional fermions: An entanglement point of view*. Phys. Rev. B, **83**:075102 (2011).

[60] L. FIDKOWSKI and A. KITAEV. *Topological phases of fermions in one dimension*. Phys. Rev. B, **83**:075103 (2011).

[61] Z.-C. GU and M. LEVIN. *Effect of interactions on two-dimensional fermionic symmetry-protected topological phases with Z_2 symmetry*. Phys. Rev. B, **89**:201113 (2014).

[62] C. WANG and T. SENTHIL. *Interacting fermionic topological insulators/superconductors in three dimensions*. Phys. Rev. B, **89**:195124 (2014).

[63] T. SENTHIL. *Symmetry-Protected Topological Phases of Quantum Matter*. Annual Review of Condensed Matter Physics, **6**(1):299–324 (2015).

[64] A. VISHWANATH and T. SENTHIL. *Physics of Three-Dimensional Bosonic Topological Insulators: Surface-Deconfined Criticality and Quantized Magnetoelectric Effect*. Phys. Rev. X, **3**:011016 (2013).

[65] D. C. TSUI, H. L. STORMER and A. C. GOSSARD. *Two-Dimensional Magnetotransport in the Extreme Quantum Limit*. Physical Review Letters, **48**:1559–1562 (1982).

[66] H. L. STORMER, D. C. TSUI and A. C. GOSSARD. *The fractional quantum Hall effect*. Rev. Mod. Phys., **71**:S298–S305 (1999).

[67] M. LEVIN and A. STERN. *Fractional Topological Insulators*. Phys. Rev. Lett., **103**:196803 (2009).

[68] L. BALENTS. *Spin liquids in frustrated magnets*. Nature, **464**:199–208 (2010).

[69] P. A. LEE. *An End to the Drought of Quantum Spin Liquids*. Science, **321**(5894):1306–1307 (2008).

[70] M. YAMASHITA, N. NAKATA, Y. SENSHU, M. NAGATA, H. M. YAMAMOTO, R. KATO, T. SHIBAUCHI and Y. MATSUDA. *Highly Mobile Gapless Excitations in a Two-Dimensional Candidate Quantum Spin Liquid*. Science, **328**(5983):1246–1248 (2010).

[71] S. SACHDEV. *Quantum magnetism and criticality*. Nature Physics, **4**(3):173–185 (2008).

[72] Z. Y. MENG, T. C. LANG, S. WESSEL, F. F. ASSAAD and A. MURAMATSU. *Quantum spin liquid emerging in two-dimensional correlated Dirac fermions*. Nature, **464**(7290):847–851 (2010).

[73] S. SORELLA, Y. OTSUKA and S. YUNOKI. *Absence of a Spin Liquid Phase in the Hubbard Model on the Honeycomb Lattice*. Sci. Rep., **2**:992 (2012).

[74] L. SAVARY and L. BALENTS. *Quantum spin liquids: a review*. Reports on Progress in Physics, **80**(1):016502 (2016).

[75] N. READ and S. SACHDEV. *Large-N expansion for frustrated quantum antiferromagnets*. Phys. Rev. Lett., **66**:1773–1776 (1991).

[76] X. G. WEN. *Mean-field theory of spin-liquid states with finite energy gap and topological orders*. Phys. Rev. B, **44**:2664–2672 (1991).

[77] A. KITAEV. *Fault-tolerant quantum computation by anyons*. Annals of Physics, **303**(1):2 – 30 (2003).

[78] A. KITAEV. *Anyons in an exactly solved model and beyond*. Annals of Physics, **321**(1):2 – 111 (2006).

[79] E. LIEB, T. SCHULTZ and D. MATTIS. *Two soluble models of an antiferromagnetic chain*. Annals of Physics, **16**(3):407 – 466 (1961).

[80] M. B. HASTINGS. *Lieb-Schultz-Mattis in higher dimensions*. Phys. Rev. B, **69**(10):104431 (2004).

[81] L. BALENTS, M. P. A. FISHER and S. M. GIRVIN. *Fractionalization in an easy-axis Kagome antiferromagnet*. Phys. Rev. B, **65**:224412 (2002).

[82] S. V. ISAKOV, Y. B. KIM and A. PARAMEKANTI. *Spin-Liquid Phase in a Spin-*$1/2$ *Quantum Magnet on the Kagome Lattice*. Phys. Rev. Lett., **97**:207204 (2006).

[83] S. V. ISAKOV, A. PARAMEKANTI and Y. B. KIM. *Exotic phase diagram of a cluster charging model of bosons on the kagome lattice*. Phys. Rev. B, **76**:224431 (2007).

[84] S. V. ISAKOV, M. B. HASTINGS and R. G. MELKO. *Topological entanglement entropy of a Bose-Hubbard spin liquid*. Nat. Phys., **7**:772–775 (2011).

[85] S. V. ISAKOV, R. G. MELKO and M. B. HASTINGS. *Universal Signatures of Fractionalized Quantum Critical Points*. Science, **335**(6065):193–195 (2012).

[86] T. GROVER and T. SENTHIL. *Quantum phase transition from an antiferromagnet to a spin liquid in a metal*. Phys. Rev. B, **81**:205102 (2010).

[87] M. CAMPOSTRINI. *Linked-Cluster Expansion of the Ising Model*. J. Stat. Phys., **103**:369–394 (2001).

[88] P. W. ANDERSON. *Localized Magnetic States in Metals*. Phys. Rev., **124**:41–53 (1961).

[89] A. GEORGES and G. KOTLIAR. *Hubbard model in infinite dimensions*. Phys. Rev. B, **45**:6479–6483 (1992).

[90] W. METZNER and D. VOLLHARDT. *Correlated Lattice Fermions in d=∞ Dimensions*. Phys. Rev. Lett., **62**:324–327 (1989).

[91] A. GEORGES, G. KOTLIAR, W. KRAUTH and M. J. ROZENBERG. *Dynamical mean-field theory of strongly correlated fermion systems and the limit of infinite dimensions*. Rev. Mod. Phys., **68**:13–125 (1996).

[92] J. KONDO. *Resistance Minimum in Dilute Magnetic Alloys*. Progress of Theoretical Physics, **32**(1):37–49 (1964).

[93] P. W. ANDERSON. *A poor man's derivation of scaling laws for the Kondo problem*. Journal of Physics C: Solid State Physics, **3**(12):2436 (1970).

[94] K. G. WILSON. *The renormalization group: Critical phenomena and the Kondo problem*. Rev. Mod. Phys., **47**:773–840 (1975).

[95] M. A. RUDERMAN and C. KITTEL. *Indirect Exchange Coupling of Nuclear Magnetic Moments by Conduction Electrons*. Phys. Rev., **96**:99–102 (1954).

[96] T. KASUYA. *A Theory of Metallic Ferro- and Antiferromagnetism on Zener's Model*. Progress of Theoretical Physics, **16**(1):45–57 (1956).

[97] K. YOSIDA. *Magnetic Properties of Cu-Mn Alloys*. Phys. Rev., **106**:893–898 (1957).

[98] S. DONIACH. *The Kondo lattice and weak antiferromagnetism*. Physica B, **91**:231 (1977).

[99] P. COLEMAN. $\frac{1}{N}$ *expansion for the Kondo lattice*. Phys. Rev. B, **28**:5255–5262 (1983).

[100] N. READ, D. M. NEWNS and S. DONIACH. *Stability of the Kondo lattice in the large-N limit*. Phys. Rev. B, **30**:3841–3844 (1984).

[101] F. F. ASSAAD. *Quantum Monte Carlo Simulations of the Half-Filled Two-Dimensional Kondo Lattice Model*. Phys. Rev. Lett., **83**:796–799 (1999).

[102] A. C. HEWSON. *The Kondo Problem to Heavy Fermions*. Cambridge Studies in Magnetism. Cambridge Universiy Press, Cambridge (1997).

[103] P. COLEMAN, C. PÉPIN, Q. SI and R. RAMAZASHVILI. *How do Fermi liquids get heavy and die?* Journal of Physics: Condensed Matter, **13**(35):R723 (2001).

[104] P. COLEMAN. *Heavy Fermions: Electrons at the Edge of Magnetism*. In *Handbook of Magnetism and Advanced Magnetic Materials*, volume 1, 95–148. John Wiley and Sons, Ltd, New York (2007). ISBN 9780470022184. Http://arxiv.org/abs/cond-mat/0612006.

[105] J. M. LUTTINGER. *Fermi Surface and Some Simple Equilibrium Properties of a System of Interacting Fermions*. Phys. Rev., **119**:1153–1163 (1960).

[106] M. OSHIKAWA. *Topological Approach to Luttinger's Theorem and the Fermi Surface of a Kondo Lattice*. Phys. Rev. Lett., **84**:3370–3373 (2000).

[107] T. SENTHIL, S. SACHDEV and M. VOJTA. *Fractionalized Fermi Liquids*. Phys. Rev. Lett., **90**(21):216403 (2003).

[108] U. F. P. SEIFERT, T. MENG and M. VOJTA. *Fractionalized Fermi liquids and exotic superconductivity in the Kitaev-Kondo lattice*. Phys. Rev. B, **97**:085118 (2018).

[109] A. N. RUBTSOV, V. V. SAVKIN and A. I. LICHTENSTEIN. *Continuous-time quantum Monte Carlo method for fermions*. Phys. Rev. B, **72**:035122 (2005).

[110] R. BLANKENBECLER, D. J. SCALAPINO and R. L. SUGAR. *Monte Carlo calculations of coupled boson-fermion systems.* Phys. Rev. D, **24**:2278–2286 (1981).

[111] R. B. LAUGHLIN. *Anomalous Quantum Hall Effect: An Incompressible Quantum Fluid with Fractionally Charged Excitations*. Phys. Rev. Lett., **50**:1395–1398 (1983).

[112] J. HUBBARD. *Electron Correlations in Narrow Energy Bands*. Proceedings of the Royal Society of London A: Mathematical, Physical and Engineering Sciences, **276**(1365):238–257 (1963).

[113] C. LANCZOS. *An iteration method for the solution of the eigenvalue problem of linear*. J. Res. Natl. Bur. Stand., **45**(4):255 (1950).

[114] J. K. CULLUM and R. A. WILLOUGHBY. *Lanczos Algorithms for Large Symmetric Eigenvalue Computations*, volume I & II. Birkhäuser, Boston (1985).

[115] S. WHITE. *Density matrix formulation for quantum renormalization groups*. Phys. Rev. Lett., **69**:2863 (1992).

[116] U. SCHOLLWÖCK. *The density-matrix renormalization group*. Rev. Mod. Phys., **77**:259 (2005).

[117] U. SCHOLLWÖCK. *The density-matrix renormalization group in the age of matrix product states*. Annals of Physics, **326**(1):96 – 192 (2011). January 2011 Special Issue.

[118] W. METZNER, M. SALMHOFER, C. HONERKAMP, V. MEDEN and K. SCHÖNHAMMER. *Functional renormalization group approach to correlated fermion systems*. Rev. Mod. Phys., **84**:299–352 (2012).

[119] E. GULL, A. J. MILLIS, A. I. LICHTENSTEIN, A. N. RUBTSOV, M. TROYER and P. WERNER. *Continuous-time Monte Carlo methods for quantum impurity models*. Rev. Mod. Phys., **83**:349–404 (2011).

[120] D. J. LUITZ. *Numerical methods and applications in many fermion systems*. Ph.D. thesis, Universität Würzburg, Fakultät für Physik und Astronomie (2013).

[121] F. ASSAAD and H. EVERTZ. *World-line and Determinantal Quantum Monte Carlo Methods for Spins, Phonons and Electrons*. In H. FEHSKE, R. SCHNEIDER and A. WEISSE, eds., *Computational Many-Particle Physics*, volume 739 of *Lecture Notes in Physics*, 277–356. Springer, Berlin Heidelberg (2008). ISBN 978-3-540-74685-0.

[122] G. SUGIYAMA and S. KOONIN. *Auxiliary field Monte-Carlo for quantum many-body ground states*. Annals of Physics, **168**(1):1 – 26 (1986).

[123] S. SORELLA, S. BARONI, R. CAR and M. PARRINELLO. *A Novel Technique for the Simulation of Interacting Fermion Systems*. EPL (Europhysics Letters), **8**(7):663 (1989).

[124] N. METROPOLIS, A. W. ROSENBLUTH, M. N. ROSENBLUTH, A. H. TELLER and E. TELLER. *Equation of State Calculations by Fast Computing Machines*. J. Chem. Phys., **21**:1087–1092 (1953).

[125] W. K. HASTINGS. *Monte Carlo sampling methods using Markov chains and their applications*. Biometrika, **57**(1):97 (1970).

[126] A. LÄUCHLI. *Introduction to Frustrated Magnetism*, volume 164 of *Springer Series in Solid-State Sciences*, chapter 18, Numerical Simulations of Frustrated Systems. Spinger, Heidelberg Dordrecht London New York (2011).

[127] M. BERCX, J. S. HOFMANN, F. F. ASSAAD and T. C. LANG. *Spontaneous particle-hole symmetry breaking of correlated fermions on the Lieb lattice*. Phys. Rev. B, **95**:035108 (2017).

[128] U. WOLFF. *Collective Monte Carlo updating for spin systems*. Phys. Rev. Lett., **62**:361–364 (1989).

[129] R. H. SWENDSEN and J.-S. WANG. *Nonuniversal critical dynamics in Monte Carlo simulations*. Phys. Rev. Lett., **58**:86–88 (1987).

[130] H. G. EVERTZ, G. LANA and M. MARCU. *Cluster algorithm for vertex models*. Phys. Rev. Lett., **70**:875–879 (1993).

[131] N. V. PROKOF'EV, B. V. SVISTUNOV and I. S. TUPITSYN. *Exact, complete, and universal continuous-time worldline Monte Carlo approach to the statistics of discrete quantum systems*. Journal of Experimental and Theoretical Physics, **87**(2):310–321 (1998).

[132] A. W. SANDVIK. *Stochastic series expansion method with operator-loop update*. Phys. Rev. B, **59**:R14157–R14160 (1999).

[133] O. F. SYLJUÅSEN and A. W. SANDVIK. *Quantum Monte Carlo with directed loops*. Phys. Rev. E, **66**:046701 (2002).

[134] F. F. ASSAAD and T. C. LANG. *Diagrammatic determinantal quantum Monte Carlo methods: Projective schemes and applications to the Hubbard-Holstein model*. Phys. Rev. B, **76**:035116 (2007).

[135] H. F. TROTTER. *On the product of semi-groups of operators*. Proc. Amer. Math. Soc., **10**:545–551 (1959).

[136] M. SUZUKI. *Relationship between d-Dimensional Quantal Spin Systems and (d+1)-Dimensional Ising Systems: Equivalence, Critical Exponents and Systematic Approximants of the Partition Function and Spin Correlations*. Progress of Theoretical Physics, **56**(5):1454–1469 (1976).

[137] M. SUZUKI. *On the convergence of exponential operators—the Zassenhaus formula, BCH formula and systematic approximants*. Communications in Mathematical Physics, **57**(3):193–200 (1977).

[138] M. BERCX, F. GOTH, J. S. HOFMANN and F. F. ASSAAD. *The ALF (Algorithms for Lattice Fermions) project release 1.0. Documentation for the auxiliary field quantum Monte Carlo code*. SciPost Phys., **3**:013 (2017).

[139] A. SANDVIK. *Stochastic method for analytic continuation of quantum Monte Carlo data*. Phys. Rev. B, **57**:10287–10290 (1998).

[140] K. S. D. BEACH. *Identifying the maximum entropy method as a special limit of stochastic analytic continuation*. eprint arXiv:cond-mat/0403055 (2004).

[141] B. ROY, F. F. ASSAAD and I. F. HERBUT. *Zero Modes and Global Antiferromagnetism in Strained Graphene*. Phys. Rev. X, **4**(2):021042 (2014).

[142] E. TANG and L. FU. *Strain-induced partially flat band, helical snake states and interface superconductivity in topological crystalline insulators*. Nature Physics, **10**:964–969 (2014).

[143] A. H. CASTRO NETO, F. GUINEA, N. M. R. PERES, K. S. NOVOSELOV and A. K. GEIM. *The electronic properties of graphene*. Rev. Mod. Phys., **81**(1):109–162 (2009).

[144] C.-K. CHIU and A. P. SCHNYDER. *Classification of reflection-symmetry-protected topological semimetals and nodal superconductors*. Phys. Rev. B, **90**(20):205136 (2014).

[145] S. RYU and Y. HATSUGAI. *Topological Origin of Zero-Energy Edge States in Particle-Hole Symmetric Systems*. Phys. Rev. Lett., **89**(7):077002 (2002).

[146] Y. TANAKA, T. YOKOYAMA, A. V. BALATSKY and N. NAGAOSA. *Theory of topological spin current in noncentrosymmetric superconductors*. Phys. Rev. B, **79**(6):060505(R) (2009).

[147] Y. LI, D. WANG and C. WU. *Spontaneous breaking of time-reversal symmetry in the orbital channel for the boundary Majorana flat bands*. New J. Phys., **15**(8):085002 (2013).

[148] V. J. KAUPPILA, T. HYART and T. T. HEIKKILÄ. *Collective amplitude mode fluctuations in a flat band superconductor formed at a semimetal surface*. Phys. Rev. B, **93**:024505 (2016).

[149] P. A. LEE, N. NAGAOSA and X.-G. WEN. *Doping a Mott insulator: Physics of high-temperature superconductivity*. Rev. Mod. Phys., **78**:17–85 (2006).

[150] D. J. SCALAPINO. *The case for $d_{x^2-y^2}$ pairing in the cuprate superconductors*. Phys. Rep., **250**:329–365 (1995).

[151] J. GEERK, X. X. XI and G. LINKER. *Electron tunneling into thin films of Y1Ba2Cu3O7*. Zeitschrift fur Physik B Condensed Matter, **73**:329–336 (1988).

[152] J. LESUEUR, L. H. GREENE, W. L. FELDMANN and A. INAM. *Zero bias anomalies in YBa $_2$Cu $_3$O $_7$ tunnel junctions*. Physica C Superconductivity, **191**:325–332 (1992).

[153] M. COVINGTON, R. SCHEUERER, K. BLOOM and L. H. GREENE. *Tunneling and anisotropic charge transport properties of superconducting (110)-oriented $YBa_2Cu_3O_7$ thin films*. Applied Physics Letters, **68**:1717–1719 (1996).

[154] S. KASHIWAYA, Y. TANAKA, M. KOYANAGI, H. TAKASHIMA and K. KAJIMURA. *Origin of zero-bias conductance peaks in high-T_c superconductors*. Phys. Rev. B, **51**:1350–1353 (1995).

[155] L. ALFF, H. TAKASHIMA, S. KASHIWAYA, N. TERADA, H. IHARA, Y. TANAKA, M. KOYANAGI and K. KAJIMURA. *Spatially continuous zero-bias conductance peak on (110) $YBa_2Cu_3O_{7-delta}$ surfaces*. Phys. Rev. B, **55**:14757(R) (1997).

[156] J. Y. T. WEI, N.-C. YEH, D. F. GARRIGUS and M. STRASIK. *Directional Tunneling and Andreev Reflection on $YBa_2Cu_3O_{7-delta}$ Single Crystals: Predominance of d-Wave Pairing Symmetry Verified with the Generalized Blonder, Tinkham, and Klapwijk Theory*. Phys. Rev. Lett., **81**:2542–2545 (1998).

[157] S. KASHIWAYA and Y. TANAKA. *Tunnelling effects on surface bound states in unconventional superconductors*. Reports on Progress in Physics, **63**(10):1641 (2000).

[158] M. COVINGTON, M. APRILI, E. PARAOANU, L. H. GREENE, F. XU, J. ZHU and C. A. MIRKIN. *Observation of Surface-Induced Broken Time-Reversal Symmetry in $YBa_2Cu_3O_7$ Tunnel Junctions*. Phys. Rev. Lett., **79**:277–280 (1997).

[159] R. KRUPKE and G. DEUTSCHER. *Anisotropic Magnetic Field Dependence of the Zero-Bias Anomaly on In-Plane Oriented [100] $Y_1Ba_2Cu_3O_{7-x}$/In Tunnel Junctions*. Phys. Rev. Lett., **83**:4634–4637 (1999).

[160] H. KASHIWAYA, S. KASHIWAYA, B. PRIJAMBOEDI, A. SAWA, I. KUROSAWA, Y. TANAKA and I. IGUCHI. *Anomalous magnetic-field tunneling of $YBa_2Cu_3O_{7-\delta}$ junctions: Possible detection of non-Fermi-liquid states*. Phys. Rev. B, **70**:094501 (2004).

[161] D. J. LUITZ and F. F. ASSAAD. *Weak-coupling continuous-time quantum Monte Carlo study of the single impurity and periodic Anderson models with s-wave superconducting baths*. Phys. Rev. B, **81**:024509 (2010).

[162] D. J. LUITZ, F. F. ASSAAD, T. NOVOTNÝ, C. KARRASCH and V. MEDEN. *Understanding the Josephson Current through a Kondo-Correlated Quantum Dot*. Phys. Rev. Lett., **108**:227001 (2012).

[163] M. HOHENADLER, T. C. LANG and F. F. ASSAAD. *Correlation Effects in Quantum Spin-Hall Insulators: A Quantum Monte Carlo Study*. Phys. Rev. Lett., **106**(10):100403 (2011).

[164] M. HOHENADLER and F. F. ASSAAD. *Rashba coupling and magnetic order in correlated helical liquids*. Phys. Rev. B, **90**(24):245148 (2014).

[165] E. F. HUFFMAN and S. CHANDRASEKHARAN. *Solution to sign problems in half-filled spin-polarized electronic systems*. Phys. Rev. B, **89**:111101 (2014).

[166] A. E. SHEYERMAN, K. Y. CONSTANTINIAN, G. A. OVSYANNIKOV, Y. V. KISLINSKII, A. V. SHADRIN, A. V. KALABUKHOV and Y. N. KHAYDUKOV. *Spin-triplet electron transport in hybrid superconductor heterostructures with a composite ferromagnetic interlayer*. Journal of Experimental and Theoretical Physics, **120**(6):1024–1033 (2015).

[167] P. LEE, T. RICE and P. ANDERSON. *Conductivity from charge or spin density waves*. Solid State Communications, **14**(8):703 – 709 (1974).

[168] C. WU and S.-C. ZHANG. *Sufficient condition for absence of the sign problem in the fermionic quantum Monte Carlo algorithm*. Phys. Rev. B, **71**:155115 (2005).

[169] Z.-X. LI, Y.-F. JIANG and H. YAO. *Solving the fermion sign problem in quantum Monte Carlo simulations by Majorana representation*. Phys. Rev. B, **91**:241117 (2015).

[170] Z.-X. LI, Y.-F. JIANG and H. YAO. *Majorana-Time-Reversal Symmetries: A Fundamental Principle for Sign-Problem-Free Quantum Monte Carlo Simulations*. Phys. Rev. Lett., **117**:267002 (2016).

[171] Z. C. WEI, C. WU, Y. LI, S. ZHANG and T. XIANG. *Majorana Positivity and the Fermion Sign Problem of Quantum Monte Carlo Simulations*. Phys. Rev. Lett., **116**:250601 (2016).

[172] M. HOHENADLER, F. PARISEN TOLDIN, I. F. HERBUT and F. F. ASSAAD. *Phase diagram of the Kane-Mele-Coulomb model*. Phys. Rev. B, **90**:085146 (2014).

[173] E. H. LIEB. *Two theorems on the Hubbard model*. Phys. Rev. Lett., **62**:1201–1204 (1989).

[174] Z.-C. WEI, X.-J. HAN, Z.-Y. XIE and T. XIANG. *Ground state degeneracy of interacting spinless fermions*. Phys. Rev. B, **92**:161105 (2015).

[175] N. GOLDMAN, D. F. URBAN and D. BERCIOUX. *Topological phases for fermionic cold atoms on the Lieb lattice*. Phys. Rev. A, **83**:063601 (2011).

[176] C. WEEKS and M. FRANZ. *Topological insulators on the Lieb and perovskite lattices*. Phys. Rev. B, **82**:085310 (2010).

[177] W. BEUGELING, J. C. EVERTS and C. MORAIS SMITH. *Topological phase transitions driven by next-nearest-neighbor hopping in two-dimensional lattices*. Phys. Rev. B, **86**:195129 (2012).

[178] R. T. SCALETTAR, D. J. SCALAPINO, R. L. SUGAR and S. R. WHITE. *Antiferromagnetic, charge-transfer, and pairing correlations in the three-band Hubbard model*. Phys. Rev. B, **44**:770–781 (1991).

[179] W. NIE, D. ZHANG and W. ZHANG. *Ferromagnetic ground state of the SU(3) Hubbard model on the Lieb lattice*. Phys. Rev. A, **96**:053616 (2017).

[180] K. NODA, K. INABA and M. YAMASHITA. *Magnetism in the three-dimensional layered Lieb lattice: Enhanced transition temperature via flat-band and Van Hove singularities*. Phys. Rev. A, **91**:063610 (2015).

[181] N. C. COSTA, T. MENDES-SANTOS, T. PAIVA, R. R. D. SANTOS and R. T. SCALETTAR. *Ferromagnetism beyond Lieb's theorem*. Phys. Rev. B, **94**:155107 (2016).

[182] B. JAWOROWSKI, A. MANOLESCU and P. POTASZ. *Fractional Chern insulator phase at the transition between checkerboard and Lieb lattices*. Phys. Rev. B, **92**:245119 (2015).

[183] A. DAUPHIN, M. MÜLLER and M. A. MARTIN-DELGADO. *Quantum simulation of a topological Mott insulator with Rydberg atoms in a Lieb lattice*. Phys. Rev. A, **93**:043611 (2016).

[184] V. I. IGLOVIKOV, F. HÉBERT, B. GRÉMAUD, G. G. BATROUNI and R. T. SCALETTAR. *Superconducting transitions in flat-band systems*. Phys. Rev. B, **90**:094506 (2014).

[185] A. JULKU, S. PEOTTA, T. I. VANHALA, D.-H. KIM and P. TÖRMÄ. *Geometric Origin of Superfluidity in the Lieb-Lattice Flat Band*. Phys. Rev. Lett., **117**:045303 (2016).

[186] M. NIŢĂ, B. OSTAHIE and A. ALDEA. *Spectral and transport properties of the two-dimensional Lieb lattice*. Phys. Rev. B, **87**:125428 (2013).

[187] O. DERZHKO, J. RICHTER and M. MAKSYMENKO. *Strongly correlated flat-band systems: The route from Heisenberg spins to Hubbard electrons*. International Journal of Modern Physics B, **29**(12):1530007 (2015).

[188] S. MUKHERJEE, A. SPRACKLEN, D. CHOUDHURY, N. GOLDMAN, P. ÖHBERG, E. ANDERSSON and R. R. THOMSON. *Observation of a Localized Flat-Band State in a Photonic Lieb Lattice*. Phys. Rev. Lett., **114**:245504 (2015).

[189] R. A. VICENCIO, C. CANTILLANO, L. MORALES-INOSTROZA, B. REAL, C. MEJÍA-CORTÉS, S. WEIMANN, A. SZAMEIT and M. I. MOLINA. *Observation of Localized States in Lieb Photonic Lattices*. Phys. Rev. Lett., **114**:245503 (2015).

[190] M. FELDBACHER, F. F. ASSAAD, F. HÉBERT and G. G. BATROUNI. *Coexistence of s-Wave Superconductivity and Antiferromagnetism*. Phys. Rev. Lett., **91**:056401 (2003).

[191] F. F. ASSAAD and T. GROVER. *Simple Fermionic Model of Deconfined Phases and Phase Transitions*. Phys. Rev. X, **6**:041049 (2016).

[192] D. GREEN, L. SANTOS and C. CHAMON. *Isolated flat bands and spin-1 conical bands in two-dimensional lattices*. Phys. Rev. B, **82**:075104 (2010).

[193] W.-F. TSAI, C. FANG, H. YAO and J. HU. *Interaction-driven topological and nematic phases on the Lieb lattice*. New Journal of Physics, **17**(5):055016 (2015).

[194] J. E. GUBERNATIS, D. J. SCALAPINO, R. L. SUGAR and W. D. TOUSSAINT. *Two-dimensional spin-polarized fermion lattice gases*. Phys. Rev. B, **32**:103–116 (1985).

[195] L. WANG, Y.-H. LIU, M. IAZZI, M. TROYER and G. HARCOS. *Split Orthogonal Group: A Guiding Principle for Sign-Problem-Free Fermionic Simulations*. Phys. Rev. Lett., **115**:250601 (2015).

[196] H. SHI and S. ZHANG. *Infinite variance in fermion quantum Monte Carlo calculations*. Phys. Rev. E, **93**:033303 (2016).

[197] S. M. A. ROMBOUTS, K. HEYDE and N. JACHOWICZ. *Quantum Monte Carlo Method for Fermions, Free of Discretization Errors*. Phys. Rev. Lett., **82**:4155–4159 (1999).

[198] K. MIKELSONS, A. MACRIDIN and M. JARRELL. *Relationship between Hirsch-Fye and weak-coupling diagrammatic quantum Monte Carlo methods*. Phys. Rev. E, **79**(5):057701 (2009).

[199] K. HARADA. *Bayesian inference in the scaling analysis of critical phenomena*. Phys. Rev. E, **84**:056704 (2011).

[200] K. S. D. BEACH, P. A. LEE and P. MONTHOUX. *Field-Induced Antiferromagnetism in the Kondo Insulator*. Phys. Rev. Lett., **92**:026401 (2004).

[201] M. V. ULYBYSHEV and S. N. VALGUSHEV. *Path integral representation for the Hubbard model with reduced number of Lefschetz thimbles*. ArXiv:1712.02188 (2017).

[202] X.-L. QI, T. L. HUGHES and S.-C. ZHANG. *Topological field theory of time-reversal invariant insulators*. Phys. Rev. B, **78**:195424 (2008).

[203] C.-X. LIU, X.-L. QI, X. DAI, Z. FANG and S.-C. ZHANG. *Quantum Anomalous Hall Effect in* $Hg_{1-y}Mn_yTe$ *Quantum Wells*. Phys. Rev. Lett., **101**:146802 (2008).

[204] S. SORELLA and E. TOSATTI. *Semi-metal-insulator transition of the Hubbard model in the honeycomb lattice*. Europhys. Lett., **19**:699 (1992).

[205] T. PAIVA, R. T. SCALETTAR, W. ZHENG, R. R. P. SINGH and J. OITMAA. *Ground-state and finite-temperature signatures of quantum phase transitions in the half-filled Hubbard model on a honeycomb lattice*. Phys. Rev. B, **72**:085123 (2005).

[206] F. F. ASSAAD and I. F. HERBUT. *Pinning the Order: The Nature of Quantum Criticality in the Hubbard Model on Honeycomb Lattice*. Phys. Rev. X, **3**:031010 (2013).

[207] F. PARISEN TOLDIN, M. HOHENADLER, F. F. ASSAAD and I. F. HERBUT. *Fermionic quantum criticality in honeycomb and π-flux Hubbard models: Finite-size scaling of renormalization-group-invariant observables from quantum Monte Carlo*. Phys. Rev. B, **91**:165108 (2015).

[208] I. F. HERBUT, V. JURIČIĆ and O. VAFEK. *Relativistic Mott criticality in graphene*. Phys. Rev. B, **80**:075432 (2009).

[209] V. AYYAR and S. CHANDRASEKHARAN. *Origin of fermion masses without spontaneous symmetry breaking*. Phys. Rev. D, **93**:081701 (2016).

[210] Y.-Y. HE, H.-Q. WU, Y.-Z. YOU, C. XU, Z. Y. MENG and Z.-Y. LU. *Quantum critical point of Dirac fermion mass generation without spontaneous symmetry breaking*. Phys. Rev. B, **94**:241111 (2016).

[211] Y.-Z. YOU, Y.-C. HE, C. XU and A. VISHWANATH. *Symmetric Fermion Mass Generation as Deconfined Quantum Criticality*. Phys. Rev. X, **8**:011026 (2018).

[212] J. C. BUDICH, J. EISERT and E. J. BERGHOLTZ. *Topological insulators with arbitrarily tunable entanglement*. Phys. Rev. B, **89**:195120 (2014).

[213] J. S. HOFMANN, F. F. ASSAAD and A. P. SCHNYDER. *Edge instabilities of topological superconductors*. Phys. Rev. B, **93**:201116 (2016).

[214] T. SENTHIL, M. VOJTA and S. SACHDEV. *Weak magnetism and non-Fermi liquids near heavy-fermion critical points*. Phys. Rev. B, **69**:035111 (2004).

[215] Q. SI, S. RABELLO, K. INGERSENT and J. SMITH. *Locally critical quantum phase transitions in strongly correlated metals.* Nature, **413**:804 (2001).

[216] S. PASCHEN, T. LÜHMANN, S. WIRTH, P. GEGENWART, O. TROVARELLI, C. GEIBEL, F. STEGLICH, P. COLEMAN and Q. SI. *Hall-effect evolution across a heavy-fermion quantum critical point.* Nature, **432**:881 EP – (2004).

[217] M. KLEIN, A. NUBER, F. REINERT, J. KROHA, O. STOCKERT and H. V. LÖHNEYSEN. *Signature of Quantum Criticality in Photoemission Spectroscopy*. Phys. Rev. Lett., **101**:266404 (2008).

[218] S. FRIEDEMANN, T. WESTERKAMP, M. BRANDO, N. OESCHLER, S. WIRTH, P. GEGENWART, C. KRELLNER, C. GEIBEL and F. STEGLICH. *Detaching the antiferromagnetic quantum critical point from the Fermi-surface reconstruction in YbRh2Si2*. Nature Phys., **5**:465–469 (2009).

[219] M. VOJTA. *Orbital-Selective Mott Transitions: Heavy Fermions and Beyond*. J. Low Temp. Phys., **161**:203 (2010).

[220] A. DÖNNI, G. EHLERS, H. MALETTA, P. FISCHER, H. KITAZAWA and M. ZOLLIKER. *Geometrically frustrated magnetic structures of the heavy-fermion compound CePdAl studied by powder neutron diffraction*. Journal of Physics: Condensed Matter, **8**(50):11213 (1996).

[221] T. GOTO, S. HANE, K. UMEO, T. TAKABATAKE and Y. ISIKAWA. *Field-induced magnetic transitions and pressure-induced magnetic instability in CePdAl*. Journal of Physics and Chemistry of Solids, **63**(6):1159 – 1163 (2002). Proceedings of the 8th ISSP International Symposium.

[222] A. OYAMADA, S. MAEGAWA, M. NISHIYAMA, H. KITAZAWA and Y. ISIKAWA. *Ordering mechanism and spin fluctuations in a geometrically frustrated heavy-fermion antiferromagnet on the Kagome-like lattice CePdAl: A Al 27 NMR study*. Physical Review B, **77**(6):064432 (2008).

[223] A. SAKAI, S. LUCAS, P. GEGENWART, O. STOCKERT, H. V. LÖHNEYSEN and V. FRITSCH. *Signature of frustrated moments in quantum critical* $CePd_{1-x}Ni_xAl$. Phys. Rev. B, **94**:220405 (2016).

[224] H. OIKE, Y. SUZUKI, H. TANIGUCHI, K. MIYAGAWA and K. KANODA. *Spin-charge-entangled non-Fermi liquid in a candidate material for a doped spin liquid*. ArXiv e-prints (2016).

[225] M. S. KIM, M. C. BENNETT and M. C. ARONSON. *Yb_2Pt_2Pb: Magnetic frustration in the Shastry-Sutherland lattice*. Phys. Rev. B, **77**:144425 (2008).

[226] K. SENGUPTA, M. K. FORTHAUS, H. KUBO, K. KATOH, K. UMEO, T. TAKABATAKE and M. M. ABD-ELMEGUID. *Geometrical frustration versus magnetic order in the heavy-fermion antiferromagnet YbAgGe under high pressure*. Phys. Rev. B, **81**:125129 (2010).

[227] Y. KATO, M. KOSAKA, H. NOWATARI, Y. SAIGA, A. YAMADA, T. KOBIYAMA, S. KATANO, K. OHOYAMA, H. S. SUZUKI, N. ASO and K. IWASA. *Spin-Singlet Ground State in the Two-Dimensional Frustrated Triangular Lattice: YbAl3C3*. Journal of the Physical Society of Japan, **77**(5):053701 (2008).

[228] T. SATO, F. F. ASSAAD and T. GROVER. *Quantum Monte Carlo Simulation of Frustrated Kondo Lattice Models*. Phys. Rev. Lett., **120**:107201 (2018).

[229] S. WHITE, D. SCALAPINO, R. SUGAR, E. LOH, J. GUBERNATIS and R. SCALETTAR. *Numerical study of the two-dimensional Hubbard model*. Phys. Rev. B, **40**:506–516 (1989).

[230] S. CAPPONI and F. F. ASSAAD. *Spin and charge dynamics of the ferromagnetic and antiferromagnetic two-dimensional half-filled Kondo lattice model*. Phys. Rev. B, **63**:155114 (2001).

[231] A. WIETEK and A. M. LÄUCHLI. *Sublattice coding algorithm and distributed memory parallelization for large-scale exact diagonalizations of quantum many-body systems*. Phys. Rev. E, **98**:033309 (2018).

[232] I. PESCHEL. *On the reduced density matrix for a chain of free electrons*. J. Stat. Mech., **6**:4 (2004).

[233] T. GROVER. *Entanglement of Interacting Fermions in Quantum Monte Carlo Calculations*. Phys. Rev. Lett., **111**(13):130402 (2013).

[234] F. F. ASSAAD, T. C. LANG and F. PARISEN TOLDIN. *Entanglement spectra of interacting fermions in quantum Monte Carlo simulations*. Phys. Rev. B, **89**(12):125121 (2014).

[235] J. E. DRUT and W. J. PORTER. *Hybrid Monte Carlo approach to the entanglement entropy of interacting fermions*. Phys. Rev. B, **92**(12):125126 (2015).

[236] J. E. DRUT and W. J. PORTER. *Entanglement, noise, and the cumulant expansion*. Phys. Rev. E, **93**(4):043301 (2016).

[237] F. PARISEN TOLDIN and F. F. ASSAAD. *Entanglement Hamiltonian of Interacting Fermionic Models*. Phys. Rev. Lett., **121**:200602 (2018).

[238] P. BROECKER and S. TREBST. *Rényi entropies of interacting fermions from determinantal quantum Monte Carlo simulations*. J. Stat. Mech., **8**:08015 (2014).

[239] L. WANG and M. TROYER. *Renyi Entanglement Entropy of Interacting Fermions Calculated Using the Continuous-Time Quantum Monte Carlo Method*. Phys. Rev. Lett., **113**(11):110401 (2014).

[240] F. F. ASSAAD. *Stable quantum Monte Carlo simulations for entanglement spectra of interacting fermions*. Phys. Rev. B, **91**(12):125146 (2015).

[241] P. BROECKER and S. TREBST. *Numerical stabilization of entanglement computation in auxiliary-field quantum Monte Carlo simulations of interacting many-fermion systems*. Phys. Rev. E, **94**(6):063306 (2016).

[242] M. B. HASTINGS, I. GONZÁLEZ, A. B. KALLIN and R. G. MELKO. *Measuring Renyi Entanglement Entropy in Quantum Monte Carlo Simulations*. Phys. Rev. Lett., **104**(15):157201 (2010).

[243] S. HUMENIUK and T. ROSCILDE. *Quantum Monte Carlo calculation of entanglement Rényi entropies for generic quantum systems*. Phys. Rev. B, **86**(23):235116 (2012).

[244] J. BECKER and S. WESSEL. *Diagnosing Fractionalization from the Spin Dynamics of Z_2 Spin Liquids on the Kagome Lattice by Quantum Monte Carlo Simulations*. Phys. Rev. Lett., **121**:077202 (2018).

[245] A. V. CHUBUKOV, T. SENTHIL and S. SACHDEV. *Universal magnetic properties of frustrated quantum antiferromagnets in two dimensions*. Phys. Rev. Lett., **72**:2089–2092 (1994).

[246] F. PARISEN TOLDIN, T. SATO and F. F. ASSAAD. *Mutual information in heavy-fermion systems*. Phys. Rev. B, **99**:155158 (2019).

[247] S. GAZIT, M. RANDERIA and A. VISHWANATH. *Emergent Dirac fermions and broken symmetries in confined and deconfined phases of Z2 gauge theories*. Nat Phys, **13**(5):484–490 (2017).

[248] S. GAZIT, F. F. ASSAAD, S. SACHDEV, A. VISHWANATH and C. WANG. *Confinement transition of Z_2 gauge theories coupled to massless fermions: Emergent quantum chromodynamics and SO(5) symmetry*. Proceedings of the National Academy of Sciences (2018).

[249] B. SWINGLE and T. SENTHIL. *Structure of entanglement at deconfined quantum critical points*. Phys. Rev. B, **86**:155131 (2012).

[250] H. YAO and X.-L. QI. *Entanglement Entropy and Entanglement Spectrum of the Kitaev Model*. Phys. Rev. Lett., **105**:080501 (2010).

[251] A. P. SCHNYDER, P. M. R. BRYDON and C. TIMM. *Types of topological surface states in nodal noncentrosymmetric superconductors*. Phys. Rev. B, **85**(2):024522 (2012).

[252] JÜLICH SUPERCOMPUTING CENTRE. *JURECA: Modular supercomputer at Jülich Supercomputing Centre*. Journal of large-scale research facilities, **4**(A132) (2018).

[253] JÜLICH SUPERCOMPUTING CENTRE. *JUWELS: Modular Tier-0/1 Supercomputer at the Jülich Supercomputing Centre*. Journal of large-scale research facilities, **5**(A135) (2019).

Publications

[P1] **J. S. HOFMANN**, F. F. ASSAAD, R. QUEIROZ, E. KHALAF. *Search for correlation-induced adiabatic paths between distinct topological insulators*. arXiv:1912.07614, accepted by Phys. Rev. Research, (2020).

[P2] **J. S. HOFMANN**, F. F. ASSAAD, T. GROVER. *Fractionalized Fermi liquid in a frustrated Kondo lattice model*. Phys. Rev. B, **100**:035118 (2019).

[P3] M. BERCX, F. GOTH, **J. S. HOFMANN**, F. F. ASSAAD. *The ALF (Algorithms for Lattice Fermions) project release 1.0. Documentation for the auxiliary field quantum Monte Carlo code*. SciPost Phys., **3**:013 (2017).

[P4] M. BERCX, **J. S. HOFMANN**, F. F. ASSAAD, T. C. LANG. *Spontaneous particle-hole symmetry breaking of correlated fermions on the Lieb lattice*. Phys. Rev. B, **95**:035108 (2017).

[P5] **J. S. HOFMANN**, F. F. ASSAAD, A. P. SCHNYDER. *Edge instabilities of topological superconductors*. Phys. Rev. B, **93**:201116(R) (2016).

[P6] **J. S. HOFMANN**, R. QUEIROZ, A. P. SCHNYDER. *Theory of quasiparticle scattering interference on the surface of topological superconductors*. Phys. Rev. B, **88**:134505 (2013).

Acknowledgements

First and foremost, I want to thank my adviser Prof. Dr. Fakher F. Assaad for his guiding supervising during my Ph.D. degree. I am grateful for the interesting topic that you provided, the encouraging discussions we had, and for appreciating the difficulties of the problems I have picked to tackle. Didn't you once introduce a new Murphy's law: "It's your project, so it has to be hard."? I would also like to thank you for supporting various exciting trips, ranging from summer schools in Italy to the visit of Tarun Grover in San Diego.

My external collaborators played an important role in the pursuit of the presented research. I met Raquel Queiroz already during my master thesis and our collaboration has led to my first publication. I appreciate the valuable discussions we had during the edge instability project, her suggestion to study the SPT model as well as the friendship that developed over the years. I am looking forward to seeing you soon at the Weizmann Institute in Israel again. Andreas Schnyder was hosting me at the Max Planck Institute (MPI) in Stuttgart and I am grateful for showing to me how interesting topological condensed matter physics is and for your (co-)supervision of my first two projects, the first of which already got published during my master's thesis and the second one was carried over to this Ph.D. thesis. I thank Tarun Grover for introducing the field of topological order to me by proposing the model we studied during the 'fractional Fermi liquid' project and also for all the discussion I enjoyed in San Diego and via Skype. Finally, I would like to mention Eslam Khalaf, whom I also got to know in Stuttgart, and acknowledge his contribution to the SPT project and the constructive discussion that started already during my masters thesis.

The members of Fakher's group have contributed immensely to my personal and professional life in Würzburg. Special thanks go to Manuel Weber, my office mate for about four years. I appreciate the inspiring discussions about physics, football and everything else. It was fun to organize the Ph.D. students meeting of the research unit FOR 1807 with you and I am grateful for the friendships that developed during this workshop. I also won't forget all

the social activities of the last couple of years. Thank you, Florian Goth, for letting me profit from your immense programming skills, for the discussions on how to separate the QMC method from specific model details which has let to my general implementation of the CT-INT algorithm. I think some of the ideas also transferred to ALF, our second general QMC method which originates from Fakher's career-long experience in this field. I also appreciate your help in hunting a bug in ALF that was ultimately located in Intel's core memory allocator. I want to thank Martin Bercx and Thomas C. Lang for encouraging collaboration on the Lieb lattice project. Last but not least, let me mention the current or former group members Stefan Beyl, Martin Hohenadler, Emilie Huffman, Marcin Raczkowski, Toshihiro Sato, Jonas Schwab, Zhenjiu Wang, Francesco Parisen Toldin, Maksim Ulybyshev and Jan Werner, thank you for the comradery.

I am especially grateful to Jan Böttcher, Florian Goth and Toshihiro Sato for carefully proofreading various chapters of this thesis and providing invaluable comments and suggestions to improve the manuscript.

Apart from the German Research Foundation (DFG) for funding my Ph.D., under DFG-FOR 1162 (AS120/6-2) and DFG-SFB No. 1170 ToCoTronics (Project No. C01), I would also like to express my gratitude for the granted access to large-scale computing centers. I gratefully acknowledge the computing time granted by the John von Neumann Institute for Computing (NIC) and provided on the supercomputer JUROPA, JURECA [252] and JUWELS [253] at Jülich Supercomputing Centre (JSC). Additionally, I gratefully acknowledge the Gauss Centre for Supercomputing e.V. (www.gauss-centre.eu) for funding this project by providing computing time on the GCS Supercomputer SuperMUC at Leibniz Supercomputing Centre (www.lrz.de). Also, I am grateful for the computing time provided on the Julia-cluster by the Rechenzentrum of the university of Würzburg.

My time in Würzburg was made even more exciting thanks to all my fellow students, colleagues and friends, not only at work, but also in our leisure time. I am looking forward to the upcoming snowboarding trip next season.

Last but not least, I would like to thank my family: my parents and my sister for their support throughout writing this thesis and my life in general.

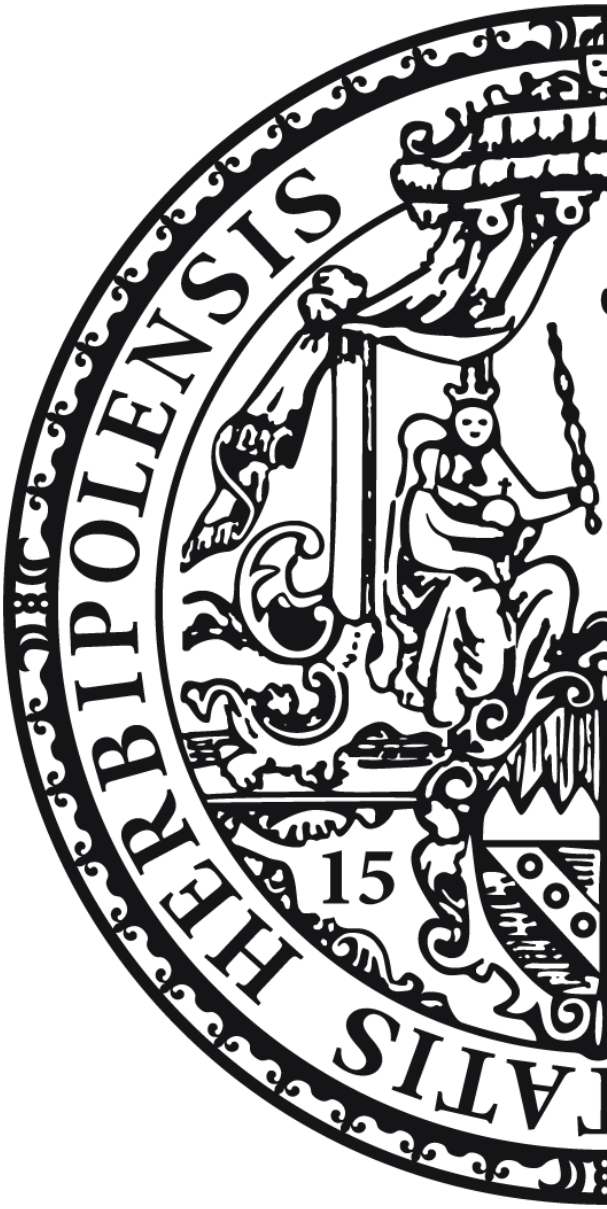
HERBIPOLENSIS
15